Far-Ultraviolet Spectroscopy of the Circumstellar and Interstellar Environment of Young Stars

by

Matthew McJunkin

B.S., Mathematics and Physics, Case Western Reserve University, 2010

M.S., Astrophysical and Planetary Sciences, University of Colorado, 2012

A thesis submitted to the

Faculty of the Graduate School of the

University of Colorado in partial fulfillment

of the requirements for the degree of

Doctor of Philosophy

Department of Astrophysical and Planetary Sciences

2016

This thesis entitled:

Far-Ultraviolet Spectroscopy of the Circumstellar and Interstellar Environment of Young Stars

written by Matthew Scott McJunkin

has been approved for the Department of Astrophysical and Planetary Sciences

---

Dr. Kevin France

Dr. James Green

Dr. Phil Armitage

Dr. Seth Hornstein

Date _____

The final copy of this thesis has been examined by the signatories, and we find that both the content and the form meet acceptable presentation standards of scholarly work in the above mentioned discipline.

McJunkin, Matthew Scott (Ph.D., Astrophysical and Planetary Sciences)

Far-Ultraviolet Spectroscopy of the Circumstellar and Interstellar Environment of Young Stars

Thesis directed by: Dr. Kevin France

I have analyzed absorption from the CO Fourth Positive band system ($A\ ^1\Pi - X\ ^1\Sigma^+$) in the ultraviolet spectra of 6 Classical T Tauri stars, tripling the measurements in the literature. CO traces the molecular gas in the inner disk, providing constraints on the material in the planet-forming environment. I fit an absorption model in order to determine the column density and temperature of the gas in the disk. My CO rotational temperatures agree well with CO fluorescence measurements in the ultraviolet, but are in between infrared CO absorption and emission measurements.

I also fit absorption profiles of H I against the Lyman-α emission from a large sample of young stars (Classical T Tauri and Herbig Ae/Be) in order to determine the amount of interstellar extinction along the line of sight. Knowing the extinction value will allow us to reconstruct the intrinsic emission from the stars, which is the radiation impacting the protoplanetary disk. This radiation determines the thermal and chemical structure of the material that may form planets. I find lower visual extinction values than those in the literature using optical, infrared, and X-ray measurement techniques.

In addition, I have created a new technique using H_2 fluorescence to empirically estimate the full ultraviolet extinction curve of young stars. I compare predicted line fluxes from my created H_2 fluorescence model to observed fluxes from 7 strong progressions in order to determine the extinction over the 1100 - 1700 Å range. I then fit my extinction curves with models from the literature to determine best-fit A_V and R_V values. I find that this technique is limited by the degeneracy between the A_V and R_V values, needing one or the other to be determined independently. I hope to improve the technique and mitigate the limitations in future work.

Dedication

"Yet what is any ocean but a multitude of drops?"

-David Mitchell, *Cloud Atlas*

For

my

friends,

family, and

collaborators who

helped create this ocean

of a thesis one drop

at a time.

Acknowledgments

I'd like to thank all the people who supported me and bolstered me along the long path towards this thesis. My research advisors, both in undergraduate and graduate school (Chris Mihos, Earle Luck, Jim Green, and Kevin France), inspired my research and helped with the challenges. I thank them for pushing me when I would get stuck in an unproductive rut. To my many other collaborators over my research career (Greg Herczeg, Christian Schneider, Lynne Hillenbrand, Eric Schindhelm, Suzan Edwards, Alex Brown, Eric Burgh, Joanna Brown, and Keri Hoadley), I want to thank you for your help in creating figures and writing portions of our papers, your thoughtful comments, and your many hours of proofreading.

To my parents, I'm thankful for your encouragement and your belief that I could do anything if I worked hard enough. Thank you for providing me with the opportunities I needed to expand my mind and choose my own path. To my sister, Sarah, I treasure all the laughs we had growing up. Thank you for being such an amazing role model who inspires me to be my best.

For me, grad school is not just about research. To succeed, I needed a support system to help take my mind off work every once in a while. So to my fellow graduate students, you have an amazing ability to cheer me up when research is not going well. I truly think we have the closest knit group of grad students in the country, and I count you all among my closest friends. Specifically to Jen, Katy, Chris, Eric, Keri, Evan, and David, you have become like family to me. I love y'all so much and I couldn't have done it without you!

And lastly, I'd like to thank Boulder itself for being a bastion of tolerance and progressive thought where I felt free to live as my true self without fear or judgment. Plus, the craft beer and mountains are a pretty good bonus!

Contents

List of Tables

List of Figures

1.   Introduction

"We are only what we know, and I wished to be so much more than I was, sorely."

- David Mitchell, *Cloud Atlas*

Planets form in disks of gas and dust around young stars often called a protoplanetary disk (PPD). The composition and structure of the disk determines the type of planets that are able to form. Molecular hydrogen (H_2) and carbon monoxide (CO) are the most prominent molecules in the disk environment, which makes determining their properties critically important. The stellar spectral energy distribution (SED) incident on the disk greatly affects the disk gas temperature and chemistry, which changes the planet-forming environment. Correcting for the absorption and scattering of light along the line of sight toward these young stars allows us to remove any circumstellar or interstellar attenuation and reconstruct the intrinsic stellar SED impacting the disk.

This thesis presents an analysis of the ultraviolet (UV) spectra of nearby young stars using the *HubbleSpaceTelescope* - Cosmic Origins Spectrograph (*HST*-COS) and Space Telescope Imaging Spectrograph (STIS) data in order to derive the properties of the surrounding circumstellar and interstellar environment. By modeling CO absorption and H_2 fluorescence originating in the disk, as well as interstellar neutral hydrogen (H I) absorption against the stellar Lyman-α (Lyα) profile, I derive disk properties such as molecular column densities and temperatures along with line of sight extinction values. These disk properties are essential in determining how planets form and evolve. An introduction to star formation is given in Section 1.1. The science goals of this thesis are discussed in Section 1.2. Relevant work in observing and modeling disks and deriving extinction measurements is presented in Section 1.3. Lastly, Section 1.4 gives a background of the molecular physics behind the molecular spectra I analyze.

1.1. Star Formation

Molecular gas is prevalent in the interstellar material of star-forming galaxies, and can range from being diffuse to quite dense. Within a cold and dense molecular cloud, regions of slightly higher density (called "cores") may become gravitationally unstable and begin to collapse. Gas thermal pressure (which increases with density and temperature) opposes the gravitational collapse, but the molecules in the cloud can quickly rid themselves of any excess thermal energy, decreasing the pressure. Collisions between molecules in the gas convert the thermal energy into excited rotational and vibrational energy levels of the molecules, which then radiate away photons. As long as these photons escape the collapsing cloud, the temperature of the cloud remains low, and the matter in the cloud collapses in near free-fall. Due to the interior of the core having a higher density, the free-fall time is shortest there, such that the core collapses from the inside-out, with the center collapsing to a protostar (pre-main-sequence star) first, followed by the outer material falling onto the protostar. If the molecular cloud which collapses has nonzero angular momentum (which is generally the case), then the infalling material cannot collapse directly onto the protostar as the rotation speed of the material increases with decreasing size due to the conservation of angular momentum. Instead, the cloud will collapse into a rotating disk with the protostar, which contains the material with the lowest specific angular momentum, at the center.

Protostars are conventionally divided into four separate classes based on the shape of their emitted spectrum. Class 0 protostars are heavily obscured by the collapsing cloud such that their spectra peak at $\lambda > 100$ μm. This stage is short, with lifetimes of just $\sim (1-3) \times 10^4$ yr (André & Motte 2000). Class I protostars have more power being emitted near 10 μm than 2 μm. At this stage, the protostar may have an outflow which has begun to clear out some of the infalling material, while an early disk may be forming, with the remaining envelope of material collapsing onto it. These stars are thought to have ages of $\sim (1-2) \times 10^5$ yr. Class II protostars have spectra similar to a stellar photosphere of their respective spectral type, with a noticeable IR excess. This IR excess is the thermal radiation

of the dust in the PPD. The molecular cloud has fully collapsed or been blown away by a protostellar outflow, leaving a pre-main-sequence star (called a classical T Tauri star at this stage), still undergoing gravitational contraction, surrounded by a PPD which is accreting onto the star with accretion rates $\sim 10^{-6}$ M$_\odot$ yr^{-1}. Classical T Tauri stars (CTTSs) are generally of the spectral types F, G, K, and M, with masses of $\sim 0.1 - 2.0$ M$_\odot$. Lastly, class III protostars generally exhibit spectra of a typical stellar photosphere. These protostars are still undergoing gravitational contraction, but the PPD has been removed through processes such as photoevaporation (see Section 1.2.3). In this thesis, I study mostly CTTSs as they provide the best glimpse of the planet-forming environment. The star-disk system is more easily viewable as the surrounding molecular cloud is absent, while the PPD, in which planets may form, is still present.

1.2. Science Goals

1.2.1. Understanding planet formation and migration

How both terrestrial and giant planets form is still not fully understood. We have detected protoplanetary disks (containing both gas and dust), gaps in protoplanetary disks, debris disks (with the gas disk dissipated), and fully formed exoplanets, but the details of how each stage moves onto the next are still the realm of the theorist. Much of the dynamics and timescales are determined by the gas surface density in the disk. By determining the amount of gas present in typical PPDs, we can better understand how quickly planets form and how planets migrate in the disk before the disk fully dissipates.

Terrestrial planets are thought to be formed by a slow build-up of dust particles that collide and stick in the PPD (see the review by Lissauer 1993). Disk dust starts as interstellar-sized grains (0.1 - 1 μm) from the collapsed molecular cloud, which then settles toward the midplane due to the gravitational force of the protostar and the drag force from the gas in the disk. These small grains collide with one another, sticking together and creating larger

particles, which then collide with each other to grow further. This process is enhanced by the radial drift inwards of the dust grains, which promotes collisions (Weidenschilling 1980; Nakagawa et al. 1981). Particles of $\sim$ cm sizes are quickly formed ($< 10^4$ years; Papaloizou & Terquem 2006) via this process.

As the grains grow larger than ~ 1 cm, the radial drift velocity increases. In the general case, the radial drift velocity of a grain at radius r (from Papaloizou & Terquem 2006) is:

$$v_{r,d} = c_s \frac{3C_D n|n|\Sigma}{16\pi\rho_d r_d} \frac{c_s^2}{r^2\Omega_K^2} \tag{1}$$

where C_D is the drag coefficient (usually of order unity, e.g. Weidenschilling 1977), n is the exponent of the gas pressure power-law ($P \propto r^{-n}$), ρ_d is the mass density of the grain, r_d is the radius of the dust grain, c_s is the sound speed, Ω_K is the oscillation frequency of the grain about the midplane with no drag force, and Σ is the gas surface density of the disk. The maximum radial drift, found via the horizontal equations of motion in the disk, is when the size of the grain is ~ 1 m, which corresponds to a very short infall time of less than 100 years at 1 AU assuming typical disk parameters. When particles grow larger than 1 m, the gas cannot disturb their orbit effectively and the radial drift speed lowers, halting the infall into the star. However, particles must grow quickly in order to get larger than 1 m in size before being accreted onto the star. This obstacle of requiring rapid planetesimal growth to prevent infall into the star when particles reach ~ 1 m in size has been called the "meter size barrier". Better measurements of the disk gas surface density would constrain the radial drift velocity and planetesimal-formation timescales of PPDs.

Planetesimals that pass the "meter size barrier" and grow to sizes ~ 10 km continue to grow through mutual gravitational interactions, collisional accretion, and interactions with the PPD. Collisional accretion alone cannot produce Earth sized objects in a typical disk lifetime ($\sim 1 - 10$ Myr; e.g., see Figure 2 in Wyatt 2008). Gravitational focusing, which adds in the gravitational attraction between the planetesimal and the colliding particles, increases the effective cross section of the planetesimal. This process is necessary to produce Earth sized objects quickly through a runaway accretion process. These objects, often called

embryo cores, become massive enough to produce an increase in the velocity dispersion of the smaller planetesimals, which then halts the runaway accretion. The cores then enter an oligarchic growth regime and may eventually open a gap, inhibiting further accretion. At this point, interactions with the disk resulting in movement of the cores may be important for further growth, but may also lead to rapid migration inwards, threatening the survival of the cores. Surviving cores may then become gas giants (see below) or may be left behind after the gas disk has dispersed to slowly accrete any remaining dusty material and become terrestrial planets.

There are two major theories of giant planet formation: the "core accretion model" (first proposed in Cameron 1973) and gravitational disk instabilities (e.g. Kuiper 1949, 1956). The core accretion model assembles a solid core in the same way as the aforementioned terrestrial planet formation until the core is massive enough to gravitationally accrete the gas around it. Initially, as the core accretes gas, the energy radiated from the infalling gas is matched by the gravitational energy released by planetesimals, which are still being accreted, falling through the atmosphere and hitting the surface of the core. The core and atmosphere evolve relatively slowly together in thermal and quasi-static equilibrium. When the core reaches a critical mass, the energy released by the atmosphere can no longer be balanced by the accretion of planetesimals. No equilibrium solution exists, and the envelope gravitationally collapses to supply more energy. This leads to rapid gas accretion and the formation of giant planets. The instability method forms giant planets from the fragmentation of the protostellar disk itself due to self-gravity. The strength of disk self-gravity leading to instability is determined by the Toomre Q parameter:

$$Q = \frac{c_s \Omega}{\pi G \Sigma} \tag{2}$$

where Ω is the epicyclic frequency. For disks with larger surface densities, Q decreases, and for $Q \lesssim 1$, the disk is unstable and can fragment into giant planets. This second method forms planets very quickly, which is an advantage, as core accretion may not be fast enough to form exoplanets with several Jupiter masses, as the formation of the solid core takes time.

Determining the gas surface density of protoplanetary disks with molecular gas studies is crucial to understanding the formation of both terrestrial and giant planets.

The gas surface density plays an important role in driving planetary migration. Tidal interactions between the gas disk and embedded protoplanets cause the protoplanets to move inwards or outwards from their formation location. These interactions are necessary to explain interesting exoplanetary systems, such as "hot Jupiters", which are Jupiter-sized planets extremely close to their parent stars. They are located inside the so-called "snow line", the disk radius outside of which volatiles such as water, carbon monoxide, and methane can condense.
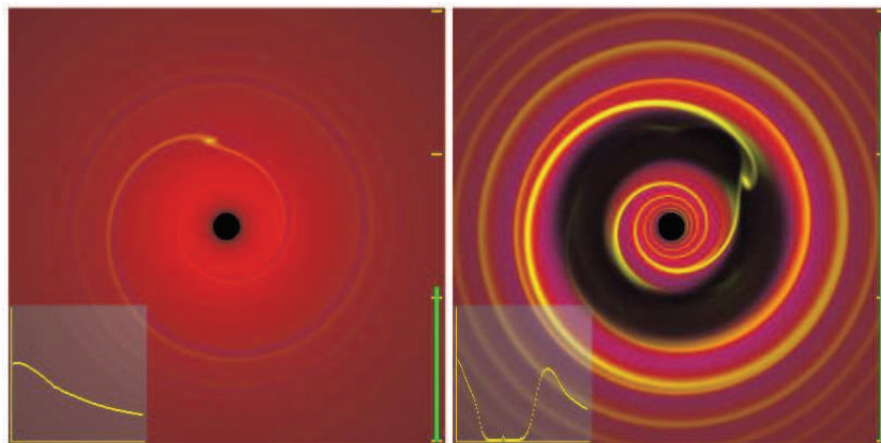
Fig. 1.1.— Illustration of Type I and Type II migration. (Left) A lower mass planet excites a spiral density wave inside and outside of its orbit, without significantly changing the the azimuthally averaged surface density profile (seen in the inset plot). (Right) A more massive $10\ M_J$ planet creates a gap in the disk, where the surface density is significantly reduced. (Figure 1 of Armitage & Rice 2005).

The first of these tidal interactions is Type I migration, which applies to lower mass protoplanets embedded in the gas disk. Lower mass planets create spiral density waves in the disk, which extend inside and outside the planetary orbit (see left-hand panel of Figure 1.1). Migration occurs when there is an imbalance between the torque exerted by

the protoplanet on the interior and exterior density waves. For laminar, circular disks with no magnetic fields, both analytical and numerical calculations find a positive torque on the disk by the protoplanet (or a negative torque on the protoplanet from the disk), causing the planet to lose angular momentum and migrate inward. The migration timescale for a circularly-orbiting planet in an isothermal axisymmetric disk determined from a local three dimensional calculation performed by Tanaka et al. (2002) is:

$$t_I = 2(2.7 + 1/1\gamma)^{-1} \frac{M_\odot}{M_p} \frac{M_\odot}{\Sigma r^2} \left(\frac{H}{r}\right)^2 \Omega^{-1} \tag{3}$$

for a central mass of 1 solar mass ($M_\odot$), planet mass of M_p, disk semi-thickness of H, and gas surface density power law exponent of γ (i.e., $\Sigma \propto R^{-\gamma}$). For typical parameters ($\gamma = 3/2$, $\Sigma = 10^3$ g cm^{-2}, $M_p = 0.1$ Earth masses, and $H/r = 0.1$), $t_I \sim 100$ yr at $r = 1$ AU.

Type II migration describes the interaction between the gas disk and a more massive planet. Massive planets have stronger interactions with the gas disk, and the exchange of angular momentum between the disk gas and the massive planet repels gas from the planetary orbit, opening a gap (see right-hand panel of Figure 1.1). The angular momentum exchange rate between the planet and the disk depends linearly on the disk gas surface density, with higher surface densities imparting more angular momentum. Once a strong gap is formed, some gas may still flow onto the planet as the gas disk evolves and gas flows through the gap. The angular momentum exchanged in this process moves the planet in the same direction as the disk gas, generally inward at smaller disk radii. The planet and the gap move inward on a timescale similar to the disk accretion timescale:

$$t_{II} \quad (\text{yr}) = \frac{0.05}{\alpha} \left(\frac{r}{H}\right)^2 \left(\frac{r}{1\text{AU}}\right)^{3/2} \tag{4}$$

using the α-prescription of Shakura & Sunyaev (1973). If $H/r = 0.1$, and α is in the range $10^{-3} - 10^{-2}$, then $t_{II} \sim 10^3$ yr at $r = 1$ AU. This migration can bring massive planets that form far from the star (with a greater reservoir of gas for large atmospheres), close to the star where they could not have formed. The amount of gas in the PPD is a crucial factor in determining how planets form from planetesimals and how they migrate in the disk.

1.2.2.   Determining the composition of protoplanetary disks

The composition of PPDs determines the composition of the exoplanets that form from the disk material. The dust in the disk is the material from which planetesimals form. These planetesimals grow to form terrestrial planets and giant planet cores. The gas in the disk initially amounts to 99% of the total mass, similar to the ISM (Williams & Cieza 2011). Larger disk masses can lead to larger gas giant atmospheres before the gas disk is dispersed by the protostar. The location of the different gasses in the disk also determines the composition of gas giants at different distances from the protostar. Determining the location and amount of gasses in a protoplanetary disk is thus essential in order to predict the planets that may form and to understand the planetary systems already observed.

The dust composition of PPDs can be studied through the broad spectral bands of silicate features at 10 and 18μm (Henning 2010), and the many mid-infrared polycyclic aromatic hydrocarbon features throughout this wavelength range (Tielens 2008). Direct observations of the 870 μm continuum emission from PPDs using ALMA have recently traced mm-sized particles down to 1 AU spatial scales. The dust in PPDs is significantly processed from the ISM dust distribution, containing larger sizes due to grain growth (Blum & Wurm 2008), and molecules frozen out from the gas phase on their surface (Bergin & Tafalla 2007).

The gas is more difficult to observe due to the specific wavelengths that it emits. This requires high resolution spectra in order to observe and characterize. Direct imaging of the gas in PPDs at high resolution is now possible with ALMA, which will probe previously unexplored structures in the disk. The dust, when optically thick, also prevents molecular lines with similar excitation temperatures from being observed. Spectrally resolved lines can be used to determine the exact spatial location of the gas, assuming a Keplerian disk. The highest velocity material, which is emitting at the inner edge of the molecular disk, emits flux in the line wings, allowing the width of the lines to measure the inner radius of the molecular gas disk.

The most prevalent molecule in protoplanetary disks is H_2, which makes observations of this molecule crucially important for understanding the bulk of the disk material. The symmetric H_2 molecule has no electric dipole moment, permitting only electric quadrupole rovibrational transitions. For the ground state, these occur mostly in the near infrared for $\Delta\nu = 1,2$ (e.g., (1 - 0) S(0): 2.223μm; (2 - 0) S(0): 1.189μm; see transition notation in Section 1.4.3), with pure rotational lines occurring in the mid-infrared ($J = 2 - 0$: 28.22μm; $J = 3 - 1$: 17.04μm). The near infrared lines probe the inner disk ($\lesssim 1$ AU; Williams & Cieza 2011). Bitner et al. (2007) spectrally resolved the $J = 3 - 1, 4 - 2$, and $6 - 4$ rotational H_2 lines in AB Aur, finding an emission radius of 18 AU from the linewidths. Dipole allowed electronic H_2 fluorescent transitions occur in the UV and indicate an origin in the inner disk very close to the protostar, like the near-infrared rovibrational lines (Herczeg et al. 2006).

Other notable atomic and molecular gas observations tracing the disk composition include the optical [O I] line at 6300Å, detected out to $\sim$100 AU in the surface of strongly flared Herbig He/Be disks (Acke et al. 2005), which is due to OH photodissociation; the [Ne II] line which traces hot disk surface gas, possibly due to a photoevaporative flow (Pascucci & Sterzik 2009); C_2H_2, HCN, and CO_2 rovibrational lines at 3 - 6 AU in both emission (Carr & Najita 2008) and absorption (Lahuis et al. 2006); and CO rovibrational emission at the stellar corotation radii for T Tauri star disks (Salyk et al. 2011a). A cartoon depicting these [O I], [Ne II], C_2H_2, HCN, CO_2, and CO line locations is shown in Figure 1.2. Ionized and atomic lines probe the disk surface, while molecular lines probe a bit deeper into the disk where shielding has helped protect against photodissociation. However, the high optical depths of H_2 fluorescence lines in many CTTSs suggest we are only probing the upper disk. This thesis includes new detections of CO absorption and new analyses of H_2 fluorescence to determine column densities and temperatures, increasing our knowledge of the structure and composition of PPDs.
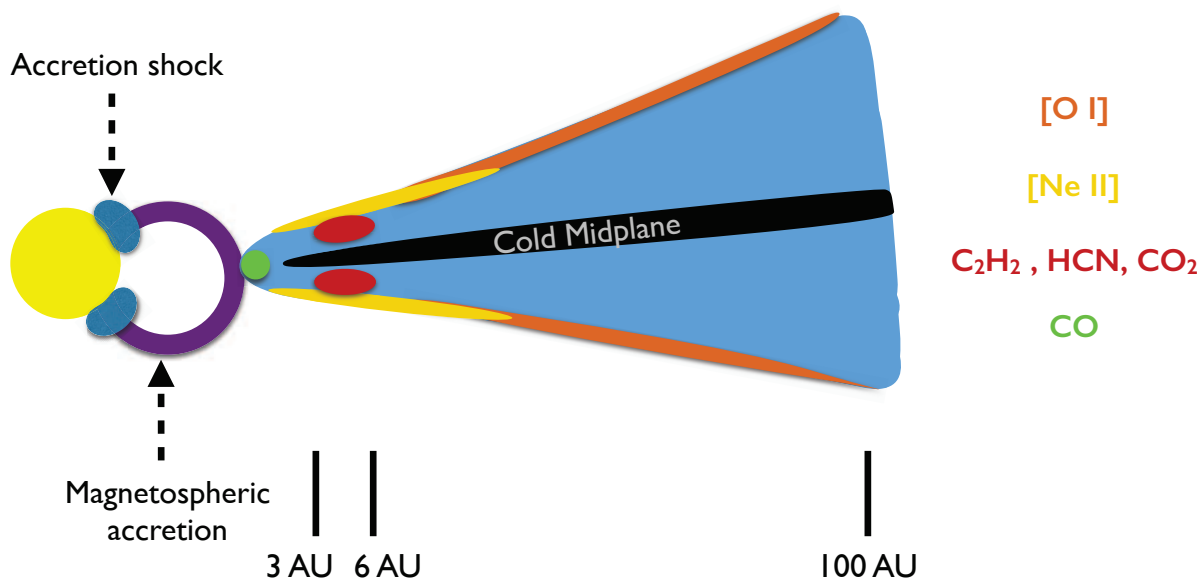
Fig. 1.2.— The locations of the [O I], [Ne II], C_2H_2, HCN, CO_2, and CO lines detected in protoplanetary disks by the referenced works in the text. The four locations corresponding to the atomic/molecular species listed on the right of the figure are depicted with the orange, yellow, red, and green regions. The disk regions without any lines of the listed species is in blue with the cold midplane highlighted in black.

1.2.3. How stellar SEDs affect disk mass, temperature and chemistry

Photoevaporation driven by photons in the far-ultraviolet (FUV: 6 eV $< h\nu <$ 13.6 eV), extreme-ultraviolet (EUV: 13.6 eV $h\nu <$ 0.1 keV), and X-ray ($h\nu >$ 0.1 keV) leads to disk mass loss and eventual disk dissipation. These photons also change the chemistry and temperature of the disk by preferentially breaking up certain molecules, leading to new disk compositions, and heating molecules through UV photon absorption. These photons can come from other nearby massive stars in star-forming regions or from the protostar itself. This thesis is concerned with how the intrinsic SED of the protostar directly affects the disk and how to correct for extinction of the SED along the line of sight.

Early photoevaporation models only used EUV photons to ionize the disk gas around early-type stars (Hollenbach et al. 1994). Enhanced versions of these early models added viscous disk evolution to the EUV photons to increase the viability (Alexander et al. 2006a,b; Clarke et al. 2001). In these models, the EUV photons originate in the stellar chromosphere and proceed to ionize and heat the circumstellar hydrogen (through the absorption of Lyman continuum photons) in the surface layer to $\sim 10^4$ K. A characteristic "gravitational radius" can be defined where the sound speed equals the local Keplerian velocity of the disk:

$$r_g = \frac{GM_*}{c_s^2} \qquad (5)$$

with c_s being the sound speed, and M_* being the stellar mass. This radius is approximately equal to the location in the disk where the total gas energy (thermal plus gravitational) in the heated surface layer is zero. Outside this radius (~ 10 AU for solar-mass stars), the total energy is positive, leading to the possibility of material flowing off the disk in a thermal wind. Accounting for rotation effects and the hydrodynamic wind structure corrects the critical wind launching radius to (Armitage 2015):

$$r_c \approx 0.2\frac{GM_*}{c_s^2}. \qquad (6)$$

Inside the critical wind launching radius, the hot, ionized gas forms a bound atmosphere which sits on top of the cool gas. Both inside and outside the critical radius, the hot and cool gas are separated by a sharp ionization front. A cartoon of this geometry (from Armitage 2015) is shown in Figure 1.3.

Early in the disk lifetime, the photoevaporation rate is much smaller than the accretion rate, leading to standard viscous evolution. The inner disk is accreted onto the star while being resupplied by material from the outer disk. Later, when the accretion rate drops to become the same magnitude as the evaporation rate, the outer disk can no longer resupply the inner disk with gas, and the inner disk drains onto the star on a viscous timescale ($\lesssim 10^5$ yrs). An inner hole of a few AU is produced, exposing the inner disk edge completely to the EUV photons. The disk then evaporates quickly from the inside out, leading to full dispersal of the gas disk.
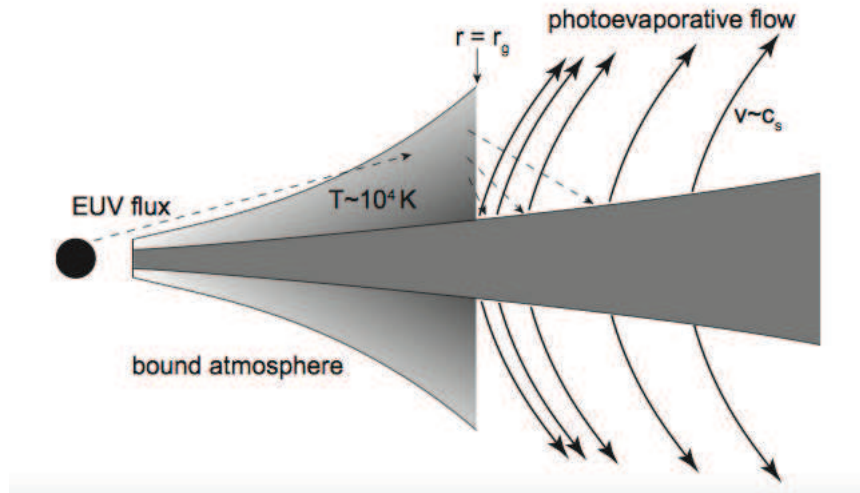
Fig. 1.3.— Cartoon of a simple photoevaporation model using EUV photons for heating and ionizing. Inside the gravitational radius r_g, the hot gas forms a bound atmosphere, while outside this radius, the hot gas is unbound and a thermally driven wind is present. The hot surface layer is separated from the cooler, lower layers by a sharp ionization front (Figure 32 of Armitage 2015).

Newer models including X-ray (e.g., Owen et al. 2010) and/or FUV photons (e.g., Gorti et al. 2009; Gorti & Hollenbach 2009) in addition to the EUV photons penetrate much larger columns of neutral gas. They are able to heat gas deeper in the disk and at larger radii, creating a larger hole through photoevaporation (up to tens of AU). Qualitatively, these newer models are similar to the older models, with some important differences. They predict photoevaporation rates that are two orders of magnitude greater than the models solely with EUV photons. They also predict inner disk holes created early in the disk lifetime, leading to a quick shutoff of disk accretion and thus disks with higher masses and large inner holes. This is contrary to observations of Weak-line T Tauri Stars (WTTSs) which tend to have lower disk masses ($\lesssim 1 - 2$ M_{Jup}; Andrews & Williams 2005, 2007a; Cieza et al. 2008, 2010). This could be explained by the disk masses and photoevaporation rates predicted by Gorti et al. (2009) and Owen et al. (2010) being overestimates.

The stellar SED photons also contribute to disk chemistry and the heating and cooling balance of the disk gas before the gas is photoevaporated. The energetic photons photo-ionize and photo-dissociate molecules, as well as drive photo-electric heating of the disk. Continuum radiation from the star radiatively pumps atoms and molecules, which can alter the cooling rates and non-LTE population. Ice formation and desorption, as well as H_2 formation is regulated by the stellar SED, most notably the UV portion, which affects the chemistry on dust grain surfaces. The most prominent molecules in PPDs, H_2 and CO, are actively photo-dissociated by the energetic stellar emission. However, self-shielding of H_2 prevents the disk H_2 from being fully dissociated, while CO is protected by its own self-shielding and shielding by H_2. FUV photons excite many molecules into excited states, with the H_2 reaction (H_2 + $h\nu \rightarrow H_2^* + h\nu$') assumed to have a rate 10 times the H_2 photo-dissociation rate (Woitke et al. 2009).

Recent work using the Protoplanetary Disk Model (ProDiMo) of Woitke et al. (2009), which uses input incident stellar SED radiation along with 2D radiative transfer, gas thermal energy balance, UV photo-chemistry, and ice formation (see Section 1.3.2), predicted an interesting disk gas thermal and chemical feature. A hot ($\approx 4000 - 7000$ K) atomic gas surface layer was seen which bends around the inner disk rim and extends out to ~ 10 AU. It is directly heated by the stellar radiation, and its lower edge corresponds to the first occurrence of molecules such as CO and OH. The H/H_2 transition occurs here as well, as the gas temperature is high enough to destroy molecular hydrogen in the $H_2 + H \rightarrow 3H$ reaction. A complex organic molecule structure for H_2, CO_2, and HCN was predicted using the full 2D radiative transfer model, but was highly dependent on the model parameters. Getting a better handle on the correct input model parameters for a "typical" protoplanetary disk and specific well-studied disks will lead to better and less varying disk structure predictions.

1.2.4. Estimating extinction curves toward young stars

As a photon travels through space from a CTTS to our telescope, it may encounter gas or dust along its path that can absorb and scatter it into a new direction. Photons scattered out of our line of sight are lost due to this circumstellar or interstellar extinction. Extinction preferentially removes shorter wavelength light, attenuating and reddening the stellar spectrum we observe. Correcting for this loss of light is crucial in order to recreate the stellar SED impacting the disk, which affects the chemical and temperature structure of the disk, as discussed in the last section.

Initial observations of the dimming of stars by the interstellar medium (ISM) are often attributed to Barnard (1907, 1910). This dimming was in addition to the known inverse square law, and was soon confirmed by Trumpler (1930) to be "fine cosmic dust particles of various sizes" which produced "selective absorption". This wavelength-dependent removal of light consists of both absorption and scattering. By viewing how the ISM interacts with light, we can study its properties and correct the observed attenuated stellar emission to get the intrinsic SED of the object behind the ISM. By comparing an obscured star with a star of the same spectral type, but with negligible obscuration, we can derive the spectral signature of the dust or other material causing the extinction. This is called the "pair method" and works well if the spectral types of the stars are known, but cannot be used for stars with uncertain or unmeasured spectral types.

The extinction is generally defined at a certain wavelength (A_λ is the extinction at wavelength λ) with the formula:

$$\frac{A_\lambda}{\text{mag}} = 2.5 log_{10}[F_\lambda^0/F_\lambda] \tag{7}$$

with F_λ as the observed flux of the star at wavelength λ, and F_λ^0 as the intrinsic flux without attenuation by extinction. The extinction is also proportional to optical depth:
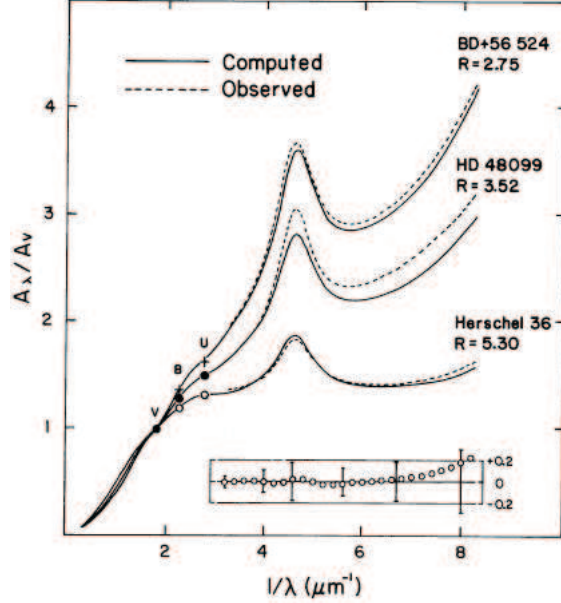
Fig. 1.4.— Extinction as a function of wavelength in the UV for different R_V values (Figure 4 of Cardelli et al. 1989).

$$\frac{A_\lambda}{\text{mag}} = 2.5 log_{10}[e^{\tau_\lambda}] = 1.086\tau_\lambda. \tag{8}$$

Different parametrizations of the extinction as a function of wavelength exist to describe the ISM. The curves use the extinction value and R_V parameter ($R_V = A_V/E(B-V)$, with $E(B-V) = (B-V)_{observed}$ - $(B-V)_{intrinsic}$ as the "reddening") to derive a full extinction curve over a wide wavelength range. The R_V parameter describes the grain size distribution, with larger values indicating more large grains than small grains. Well-determined R_V values range in the literature from $R_V = 2.1$ for HD 210121 (Welty & Fowler 1992) to $R_V \approx 5.7$ for HD 36982 (Cardelli et al. 1989; Fitzpatrick 1999). Cardelli et al. (1989) and Fitzpatrick & Massa (2005) present widely used ISM model curves to fit extinction data. The Cardelli et al. (1989) curves can be seen in Figure 1.4. The UV portion of the curve, which I use mostly in this work, is characterized by an initial linear function with a superimposed bump at ~ 2175Å, and a far-UV rise. This 2175Å bump is poorly understood, but may be due to

small, partially graphitized carbonaceous dust grains (e.g., Draine & Malhotra 1993; Mathis 1994; Mennella et al. 1998; Schnaiter et al. 1998) or polycyclic aromatic hydrocarbons (e.g., Joblin et al. 1992; Li & Draine 2001; Duley 2006). Once the extinction as a function of wavelength is known, the effects of the extinction can be taken out of the observed stellar spectrum to obtain the intrinsic stellar SED.

1.3. Previous Work

1.3.1. Observational work on molecules in protoplanetary disks

Molecules in the inner regions of protoplanetary disks probe the temperature and chemical structure of the planet-forming region around young stars. The inner disk gas also contributes strongly to migration rates of planets (Ward 1997). Najita et al. (2003) detected CO fundamental ($v = 1 \to 0$) emission (with high excitation temperatures of ~ 1000 K) from the terrestrial planet forming region of several T Tauri stars. Rettig et al. (2004) also discovered CO $v = 1 \to 0$ rovibrational emission in the inner disk of the T Tauri star TW Hya. They found a CO rotational temperature of ~ 400 K, suggesting a disk radius location of 0.5 - 1.0 AU in their preliminary model. They also found lower column densities, suggesting that the inner disk was being depleted due to dust and gas accretion onto the star. Strangely, they did not find hot CO emission, suggesting that the innermost disk region ($\lesssim 0.5$ AU) had been totally cleared.

Salyk et al. (2007) expanded on the Rettig et al. (2004) work by detecting CO emission from TW Hya over a wider range of rotational energies as well as the first CO $v = 1 \to 0$ emission from the T Tauri star GM Aur. Their observed TW Hya emission was from hot (~ 4000 K) CO, suggesting the emission came from a much smaller radius of 0.07 AU. The former Rettig et al. (2004) work incorrectly assumed optically thin lines, leading to the emission location discrepancy. Salyk et al. (2007) also found lower inner disk masses which could not be maintained for more than a few hundred years at the measured accretion

rate unless the inner disk was being resupplied by outer disk material. Colette Salyk and her collaborators have detected and studied many other molecules, such as OH, H_2O, HCN, C_2H_2, and CO_2, with temperatures ($T \sim 500 - 1500K$) and line shapes consistent with emission from the inner regions ($\sim 0.5 - 5$ AU) of CTTSs (Salyk et al. 2008, 2011b), and have expanded the amount of sources probed by the important CO rovibrational emission (Salyk et al. 2011a), observing CO emission at the inner radius of CTTS disks. Other notable works studying rovibrational emission from hot, gaseous CO in CTTS in the inner disk atmosphere include Brittain et al. (2003), who find CO emission from both the inner rim and the outer disk (> 80 AU) in AB Aur, and Najita et al. (2003), who detect CO at a large range of disk radii ($\sim 0.05 - \gtrsim 1$ AU) for many T Tauri targets.

Gregory Herczeg did much of the pioneering work identifying and measuring large numbers of H_2 fluorescent lines in CTTSs using STIS, specifically TW Hya, RU Lup, DF Tau, T Tau, and DG Tau (Herczeg et al. 2002, 2004, 2005, 2006). Previous studies of T Tauri stars with low-resolution *International Ultraviolet Explorer* (*IUE*) data detected a few H_2 fluorescence lines (Valenti et al. 2000; Johns-Krull et al. 2000), while Ardila et al. (2002) detected a total of 19 different lines over 8 targets using the Goddard High Resolution Spectrograph. Using UV STIS data, Herczeg et al. (2002, 2004, 2006) identified H_2 fluorescent emission that has been pumped by the stellar Lyα line. These lines were used to constrain the column density and temperature of the H_2 in the disks for the first time. Much of the line analysis was based on the work of Wood et al. (2002), who studied Lyα fluoresced H_2 lines in the spectra of the variable star Mira B with a Monte Carlo radiative transfer code.

France et al. (2012b) presented the largest spectrally resolved survey of H_2 fluorescence from young stars composed of new and previous *HST*-COS and STIS spectra in the far-UV. Previous large spectral surveys, such as those by Ingleby et al. (2009) and Yang et al. (2012), had lower spectroscopic sensitivity or resolution. 34 T Tauri stars were in the France et al. (2012b) sample with ages between ~ 1 and 10 Myr. H_2 emission was seen in the spectra of all the accreting sources, originating predominantly at radii $\lesssim 3$ AU, consistent with the CO

emission observed in the mid-IR (see above). Recently, Hoadley et al. (2015b) created a 2D radiative transfer model to fit H_2 emission from 14 CTTSs to study the radial distribution of H_2 as disks evolve from primordial disks (a full dust disk) to transition disks (with little-to-no warm dust present). They observe a strong correlation between disk evolutionary stage and the location of the H_2 fluorescence, with the transition disk targets having a larger emission radius. They propose that either the evolution of the disk leads to physical structure changes in the warm molecular disk which enables the exciting Lyα photons to propagate further into the disk, that the H_2 ground-state populations change over time, or that H_2 molecules are being destroyed in the inner disk over time and are not reforming due to the lack of dust grains in the region.

1.3.2. Protoplanetary disk models

Models of PPDs taking into account the physical and chemical processes occurring in the disk environment can predict the disk structure and dynamics. Kamp & Bertoldi (2000) created a simple disk model involving a dust and gas density distribution with a radial power law and vertical Gaussian, dust extinction properties, and ionization balance, which computed equilibrium abundances of 47 atomic, ionic, and molecular species in a complex chemical network. Woitke et al. (2009) introduced the code called ProDiMo (Protoplanetary Disk Model) based on the thermo-chemical models of Inga Kamp (Kamp & Bertoldi 2000; Kamp & van Zadelhoff 2001; Kamp & Dullemond 2004), and updated with more physical properties included. ProDiMo calculates the thermal, chemical, and physical structure consistently using global iterations. The iterations contain the 2D radiative transfer of dust continuum, gas thermal energy balance, kinetic gas-phase and UV photo-chemistry, ice formation, and hydrostatic disk structure calculation in axial symmetry. The iteration structure of the code can be seen in Figure 1.5.
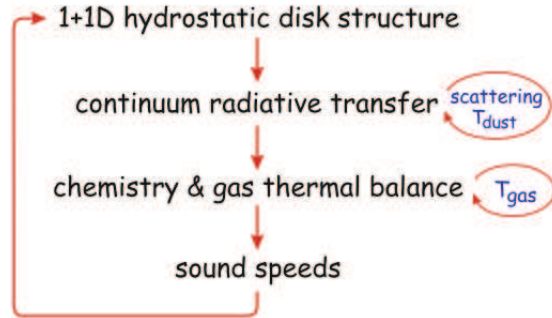
Fig. 1.5.— Global iterations of ProDiMo (Figure 1 of Woitke et al. (2009)). Circular arrows on the right are sub-iterations. The gas temperature structure must be iterated in the chemistry and gas thermal balance.

Using ProDiMo, Woitke et al. (2009) predicted that the dense, cold midplane of a PPD was surrounded by a layer of hot ($T_g \approx 5000$ K), thin ($n_{<H>} \approx 10^7$ to 10^8 cm^{-3}) atomic gas predominantly heated by the stellar UV radiation. This layer extended out to a radius of 10 AU and a height of $z/r \sim 0.5$. This inner disk region is most important for our studies of planet formation. Dust grains in this layer scatter the stellar radiation down toward the disk, which affects the disk chemistry. Woitke et al. (2011) apply the ProDiMo code, with improvements in treating PAH ionization balance and heating, exothermic reaction heating, and non-thermal gas emission line pumping mechanisms to model the disk of the T Tauri star ET Cha. They find that the models predict a small disk for the star ($R_{out} = 6 - 9$ AU) and a large gas-to-dust mass ratio of at least 2000. The derived disk mass of the star was also very small compared to the high accretion rate that was estimated. The predicted lifetime of the disk was calculated to be 0.05 - 3 Myr, much younger than the age of the Chamaeleontis cluster (8 Myr; Mamajek et al. 2000). They concluded that the unusual star is either much younger than the cluster, or is undergoing a stage of highly increased mass accretion.

Tilman Birnstiel has done an enormous amount of work on modeling the dust composition of protoplanetary disks (e.g., Birnstiel et al. 2009, 2010a,b, 2012b,a, 2015). Under-

standing how dust grains grow, how small dust grains are replenished, and how dust grains survive radial drift through the "meter size barrier" is critical to understanding the formation of terrestrial planets and giant planet cores. He and his collaborators found by using a dust and gas evolution code that turbulence is necessary to explain why disks stay "dusty" with a large amount of small dust particles as grain growth occurs in the disk (Birnstiel et al. 2012b). For critical collision velocities of 1 m s^{-1}, fragmentation is effective at keeping small dust particles (which have low radial drift velocities), present throughout the lifetime of the disk (Birnstiel et al. 2009). For collision velocities of 10 m s^{-1}, particles grow too large and drift inwards, amounting to significant dust loss. The "meter size barrier" still remains a problem for the growth of planetestimals in PPDs, though continuing work on dust evolution models hopes to solve this in the future. Birnstiel et al. (2012a) also try to explain transition disks with grain growth models, but fail to produce the dark emission cavities seen in the millimeter-wave interferometric images, though they can reproduce the observed infrared SED dips. Most recently, Birnstiel et al. (2015) produced gaps in scattered light images of PPDs using inefficient dust particle fragmentation.

Vasyunin et al. (2011) also studied dust evolution in PPDs, but focused more on UV penetration into the disk and subsequent chemical abundance ratios. Dust growth, fragmentation, and sedimentation are included in their (1+1)-dimensional α-viscosity model to calculate the disk temperature and density structures. The grain growth and dust settling of the models leads to higher UV irradiation onto the upper disk as well as enhanced gas-phase molecular abundances. The column densities of gas-phase H_2O and C_2H are proposed as observational tracers of grain growth for the inner disk, though more work is needed to determine if this is model dependent.

1.3.3. Previous extinction measurement work in many wavelength regions

The literature is full of studies measuring the extinction toward protostars in many different wavelength regions. The pair method is used to determine extinctions by comparing the SED of a reddened star to that of a similar star with little reddening (Rudnick 1936). Veiling of the stellar photosphere due to excess accretion emission (e.g., Gullbring et al. 1998) makes this calculation challenging unless one can accurately remove this effect from the SED. Modeling of spectrophotometry, including both the underlying stellar photosphere and the veiling continuum, has been done by Hartigan & Kenyon (2003),Herczeg & Hillenbrand (2014), and McJunkin et al. (2014). Gullbring et al. (2000) used an accretion-shock model to fit the observed stellar SED in the optical (which included excess veiling emission), while also providing a test to the model by fitting the SED in the UV where shock emission should dominate.

Optical extinction measurements can be similarly calculated by comparing the color of the reddened star to an assumed intrinsic color based on the spectral type (e.g., Kenyon & Hartmann 1995). Large stellar temperature gradients due to rapid rotation (Müller et al. 2011) as well as scatter in the intrinsic spectral color and temperature of a particular spectral type (Gerbaldi et al. 1999) lead to wide variance in the calculated optical extinctions. CTTSs are also optically variable (Herbst et al. 1994), which can include large color variability, leading to further difficulty in measuring optical extinctions from colors or spectrophotometry. Stars in close binaries also may have inaccurate color determinations, though most of the binary stars I study in this thesis are not close enough to their companions to be affected (except possibly AK Sco, HD 104237, TWA 3A, and V4046 Sgr).

IR extinctions have been derived using Two Micron All Sky Survey magnitudes and assumed $J - H$ or $J - K$ photospheric colors with a standard interstellar reddening law (e.g., White & Hillenbrand 2004; Furlan et al. 2011). These can be converted to visual extinctions using the formula: $A_V/A_J = 3.55$ (Furlan et al. 2011). White & Hillenbrand (2004) use the 2MASS colors that are closest to photospheric as possible so that the measured extinction

is not contaminated. Some visual extinctions have been determined using IR data by simultaneously fitting the observed target flux, the excess veiling, and the extinction corrected photospheric template emission at a specific wavelength (Fischer et al. 2011; McClure et al. 2013). McClure et al. (2013) find the visual extinction using the formula:

$$A_V = \frac{1}{A_\lambda/A_V} 2.5 log((1 + r_\lambda) \frac{F_{phot}(\lambda)}{F_{t,obs}(\lambda)}) \tag{9}$$

with A_λ/A_V being an assumed extinction curve, $F_{phot}(\lambda)$ being the (extinction corrected) photospheric template flux, $F_{t,obs}(\lambda)$ being the observed target flux, and r_λ being the degree of continuum veiling ($r_\lambda = F_V(\lambda)/F_c(\lambda)$, with $F_V(\lambda)$ as the excess flux and $F_c(\lambda)$ as the continuum flux). A linear fit with $2.5 log((1 + r_\lambda) F_{phot}(\lambda)/F_{t,obs}(\lambda))$ as the ordinate, A_λ/A_V as the abscissa, and A_V as the slope is used to calculate the visual extinction (Fischer et al. 2011). Edwards et al. (2013) introduced new extinction assessment diagnostics using hydrogen Paschen and Brackett line ratios in the near-IR compared to predicted ratios from the local line excitation models of Kwan & Fischer (2011). This allowed them to place constraints on the validity of published literature extinction values by comparing the line ratios corrected by the published extinction values to the predicted line ratios from the Kwan & Fischer (2011) models.

Extinctions calculated from X-ray data generally use two-temperature parameterization fits to CCD resolution ($R \sim 15 - 20$) spectra (e.g., Skinner et al. 2004; Güdel et al. 2007a; Testa et al. 2008; Günther & Schmitt 2009; López-Santiago et al. 2010) to obtain an equivalent hydrogen column density (N_H = N(H I) + 2N(H$_2$) + N(H II)), though the hydrogen is not directly measured. The two-temperature fits are necessary to describe the two distinct X-ray emission sources in CTTSs: the cooler ($\sim$ 0.2-0.3 keV) component from the localized accretion shock hot-spot, and the harder ($\sim$ 1 keV) component produced in the hot coronal magnetic loops (Kastner et al. 2002). In the second chapter of this thesis, I use the equivalent hydrogen column densities as my "best estimate" of N(H I) and convert these values to visual extinctions using the Bohlin et al. (1978) relation.

There is little agreement between the visual extinctions calculated using optical, IR, and

X-ray data. However, this is most likely due to the fact that each wavelength region traces different attenuation sources. The optical and IR generally trace the dust content along the line of sight, whereas the X-ray photons are attenuated by dust grains, as well as atomic and molecular gas. The different wavelength bands likely probe different locations in the disk, such that while each method travels the same path through the interstellar medium, the path through the circumstellar medium will be different, affecting the extinction measurement. The variability of these CTTSs may also play a role, with varying circumstellar obscuration changing the extinction between measurements (Herbst et al. 1994).

1.4. Molecular Physics

1.4.1. Rovibrational transitions

Because molecules are made up of more than one atom, their spectra are necessarily more complex than atomic spectra. All interactions between the individual nuclei and electrons combine to make the complex molecular spectra we observe. In this thesis, the molecules studied are diatomic (CO and H_2), which are the simplest molecules to understand. In addition to the motion of the electrons between orbitals, molecules have rotational and vibrational transitions due to the motion of the individual nuclei in the molecule. In the Born-Oppenheimer approximation, the electronic, rotational, and vibrational transitions are considered separately such that the total molecular wavefunction is simply the product of the individual wavefunctions for each transition, and the total energy is the sum of the individual energies for each transition.

The electronic states of molecules are described by potential energy curves made up of the Coulomb potential of the nuclei and the energy from the motion of the electrons through the nuclear electric field. At a fixed separation r_n, the electron eigenfunctions (ψ_q) and eigenenergies ($E_q^{(e)}(r_n)$), with q representing the quantum numbers that characterize the eigenfunction, can be obtained by solving the electron Schrödinger equation for the electrons

moving in this potential. Slowly changing the separation changes these eigenfunctions and eigenenergies adiabatically, so we can define the effective potential governing the internuclear separation (for diatomic molecules like CO and H_2) by the function:

$$V_q(r_n) = E_q^{(e)}(r_n) + Z_1 Z_2 \frac{e^2}{r_n} \tag{10}$$

where Z_1 and Z_2 are the atomic numbers of the two nuclei. The minimum of this potential curve is defined as the energy of the electronic state. The lowest binding electronic states of CO and H_2 are shown in Figure 1.6 and Figure 1.7 respectively.

To first order, the radial, or "vibrational", motions of the two nuclei in a diatomic molecule behave as a simple harmonic oscillator. The potential for this motion is:

$$V_q(r) \approx V_q(r_0) + \frac{1}{2} k (r - r_0)^2 \tag{11}$$

where r_0 is the nuclear separation where $V_q(r)$ has a minimum, and k is a "spring constant". This potential has energy levels of the form:

$$E_{vib} = h\nu_0 \left(v + \frac{1}{2} \right) \tag{12}$$

with natural oscillator frequency ν_0 and vibrational quantum number v. The natural oscillator frequency ν_0 is defined as $\omega_0/2\pi$ with $\omega_0 = (k/m_r)^{1/2}$ (m_r is the reduced mass of the molecule). Corrections to this approximate energy due to the potential $V(r)$ not being exactly quadratic include terms of the form $(v + \frac{1}{2})^n$, where n is an integer.

We can approximate the rotational motion of the molecule about the center of mass as a rigid rotator. The energy levels of the rigid rotator are:

$$E_{rot} = hBJ(J + 1) \tag{13}$$

where B is the rotational constant described by $\hbar^2/2m_r r_0^2$, and J is the rotational quantum number. The rotational constant B depends on the vibrational state through the parameter r_0. As vibrations stretch the molecule, r_0 increases, lowering the rotational constant.
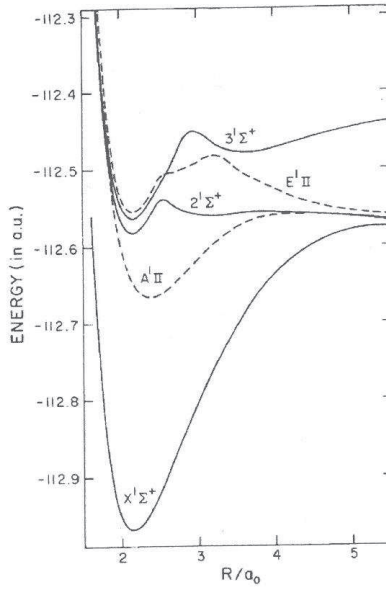
Fig. 1.6.— Lowest binding CO electronic states from Kirby & Cooper (1989).
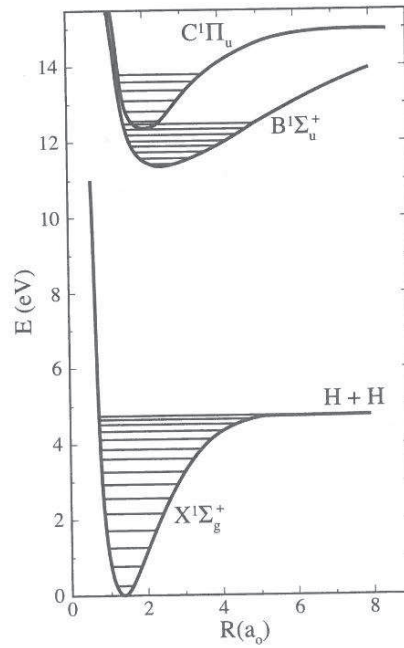
Fig. 1.7.— Lowest binding H_2 electronic states from Draine (2011). The $A^3\Sigma_u^+$ state of H_2 exists as a non-binding state at ~ 5 eV above the ground state between the $X^1\Sigma_g^+$ and $B^1\Sigma_u^+$ electronic states.

Corrections to this simplified energy equation due to the molecule not being a perfect rigid rotator are of the form $J^n(J+1)^n$, with n again being an integer.

Putting the energy expressions together and writing out the first few terms in the rotational and vibrational expansions, we have the energy levels for the diatomic molecule:

$$E_{tot}(v, J) = E_{el} + E_{vib} + E_{rot} \tag{14}$$

$$= E_{el} + \omega_e \left(v + \frac{1}{2}\right) - \omega_e x_e \left(v + \frac{1}{2}\right)^2 + \dots + B_v J(J+1) - D_v J^2 (J+1)^2 + \dots \tag{15}$$

where E_{el} is the energy of the electronic state (defined to be 0 for the ground state), and the terms ω_e, x_e, B_v, and D_v are measured constants (Herzberg 1950). Each electronic state thus has a rovibrational spectrum of energies which can be seen for the ground state of H_2 in Figure 1.8.
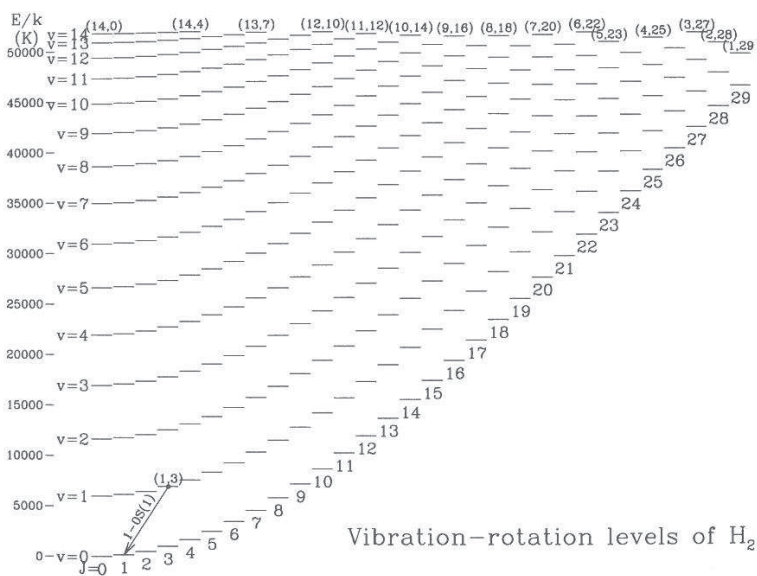
Fig. 1.8.— H_2 rovibrational energy levels of the ground electronic state with $J \leq 29$ from Draine (2011).

1.4.2.   Selection rules

Transitions between different electronic, rotational, and vibrational states of a molecule follow certain selection rules similar to atoms. We can separate the different types of transitions that can occur into pure rotational, rovibrational, and electronic in order of increasing energy. Pure rotational transitions are mostly seen in the far-infrared and radio; rovibrational transitions are seen in the infrared; and electronic transitions are observed in the UV. When discussing absorbing transitions, primed quantum numbers (e.g., v', J') will represent the upper level, while unprimed quantum numbers (e.g., v, J) will represent the lower level. For emitting transitions, the upper level will still be denoted with primed variables, while the lower level will be represented with double primed variables (e.g., v'', J'').

In the dipole approximation, it is assumed that the dipole moment of the molecule is not zero ($d \neq 0$), and that the dipole moment changes during the transition. In purely rotational transitions, this leads to the selection rules:

1. $d \neq 0$

2. $\Delta J = -1$ (emission).

   $\Delta J = +1$ (absorption).

Physically, the first selection rule arises from the fact that a classical rotating system only radiates if its dipole moment changes. If $d = 0$, then the rotating system cannot radiate classically, leading to the first selection rule. The second selection rule arises from the evaluation of the dipole matrix element (which involves an integral over spherical harmonics), and the fact that the parity must change in a dipole transition. The parity of a wavefunction is even if it is symmetric under a $r \to -r$ transformation ($\psi \to \psi$), and odd if it is antisymmetric ($\psi \to -\psi$). As a consequence of the first selection rule, homonuclear diatomic molecules (like H_2) cannot produce pure rotation spectra in the dipole approximation. However, weaker pure rotation spectra due to higher order radiation, such as electric quadrupole radiation,

have been observed. This is the reason why H_2 emission in the infrared is weak, and why I choose to study the stronger electronic dipole transitions in the UV.

Increasing in energy, we can add vibrational transitions along with the rotational transitions. These are rovibrational transitions, and the dipole selection rules are:

1. $d \neq 0$

2. $\frac{d(d)}{dr}|_{r=r_0} \neq 0$

3. $\Delta v = -1$ (emission) or

   $\Delta v = +1$ (absorption)

4. $\Delta J = \pm 1$ for $\Lambda = 0$

   $\Delta J = \pm 1, 0$ for $\Lambda \neq 0$.

Λ is the absolute value of the projection of the electronic orbital angular momentum along the internuclear axis, with electronic states $\Lambda = 0, 1, 2, 3,...$ denoted by Σ, Π, Δ, Φ, ... respectively. The first rule is the same as the rule for purely rotating systems. The second rule requires a change in the dipole moment during a change in vibrational state. The third rule comes from the quantum rule governing harmonic oscillators. The final rule again arises from the fact that parity must change in a dipole transition. When $\Lambda = 0$, the parity is solely determined by the rotational quantum number J, and the second selection rule of purely rotational transitions is obtained. When $\Lambda \neq 0$, the rotational levels split into two levels (one for $+\Lambda$ and one for $-\Lambda$), in a process called Λ doubling. These different levels have opposite parity, allowing parity to change when $\Delta J = 0$. $\Delta J = +1$ and $\Delta J = -1$ are both allowed in either emission or absorption in a rovibrational transition because the vibrational transition contains the majority of the total energy change.

Electronic transitions of molecules are quite complex, but for completeness, the specific rules governing the electronic dipole transitions in diatomic molecules are:

1. $\Delta\Lambda = -1, 0, +1$

2. $\Delta J = -1, 0, +1$, but $J = 0 \rightarrow J = 0$ is not allowed

   and $\Delta J = 0$ is not allowed if $\Lambda = 0 \rightarrow \Lambda = 0$

3. $\Delta v =$ any positive or negative integer

There is no restriction on Δv because the dipole transition is an electronic one. H_2, which does not have a permanent dipole moment, can produce strong dipole emission through electronic transitions, which do not have the $d \neq 0$ selection rule. In this thesis I only focus on two molecular electronic transitions, the CO Fourth Positive $(A^1\Pi - X^1\Sigma^+)$ band in absorption from the $^1\Sigma^+$ ground state to the upper $^1\Pi$ state, and the Lyman band H_2 transitions between the ground state $(X^1\Sigma_g^+)$ and the excited state $(B^1\Sigma_u^+)$, both of which occur in the UV.

1.4.3. Molecular Band and Progression Structure

The common notation for a fluorescence transition is $(v' - v'')P(J'')$, which represents a transition between the (v',J') and (v'',J'') states. The letter (P in the example) is the rotational branch and represents the ΔJ value, which allows this notation to uniquely specify a transition. The electric dipole and quadrupole branch letters are O, P, Q, R, and S corresponding to $\Delta J =$ -2, -1, 0, 1, and 2. Thus, the notation $(v' - v'')R(J'')$ represents a transition between the $(v',J''+1)$ and (v'',J'') states. A consequence of the second electronic dipole selection rule and the requirement that J is positive is that $J = 0$ is forbidden in both the Q and R branches.

For the H_2 fluorescence I study, I look at seven strong progressions in emission. A vibrational progression consists of all of the transitions out of a vibrational state in the upper electronic state into all vibrational levels in the lower electronic state. Each vibrational progression contains lines of uniformly spaced frequencies, though I only fit the strongest,

uncontaminated lines from each progression in my H_2 fluorescence fitting. In the CO absorption, I look at 9 bands in the Fourth Positive band system $(A^1\Pi - X^1\Sigma^+)$. An electronic absorption band is a group of absorption lines all originating from the same vibrational level (v) in the lower electronic state up to another vibrational level (v') in the upper electronic state. The band structure seen in my CO absorption consists of a bandhead where the strongest absorption occurs, followed by many weaker absorptions extending to longer wavelengths. This is the rotational fine structure superimposed on the vibrational structure. The bandhead is the absorption from the $(v,J) = (0,0)$ state of the ground CO electronic state $(X^1\Sigma^+)$ to the $(v',1)$ state of the upper CO electronic state $(A^1\Pi)$ for each $v' = 0$ - 9 band we observe, while the weaker absorptions at longer wavelengths are absorptions from the higher-J states of the ground $v = 0$ state. These absorptions are weaker as these higher-J lines are less populated at the temperatures observed in PPDs.

2.   CO Absorption Line Spectroscopy

"'Belief, like fear or love, is a force to be understood as we understand the theory of relativity and principals of uncertainty. Phenomena that determine the course of our lives. Yesterday, my life was headed in one direction. Today, it is headed in another. Yesterday, I believe I would never have done what I did today. These forces that often remake time and space, that can shape and alter who we imagine ourselves to be, begin long before we are born and continue after we perish. Our lives and our choices, like quantum trajectories, are understood moment to moment. That each point of intersection, each encounter, suggest a new potential direction."

- David Mitchell, *Cloud Atlas*

Carbon monoxide (CO) is the most commonly used tracer of molecular gas in the inner regions of protoplanetary disks. CO can be used to constrain the excitation and structure of the circumstellar environment. Absorption line spectroscopy provides an accurate assessment of a single line-of-sight through the protoplanetary disk system, giving more straightforward estimates of column densities and temperatures than CO and molecular hydrogen (H_2) emission line studies. I analyze new observations of ultraviolet CO absorption from the *Hubble Space Telescope* along the sightlines to six classical T Tauri stars. Gas velocities consistent with the stellar velocities, combined with the moderate-to-high disk inclinations, argue against the absorbing CO gas originating in a fast-moving disk wind. I conclude that the far-ultraviolet observations provide a direct measure of the disk atmosphere or possibly a slow disk wind. The CO absorption lines are reproduced by model spectra with column densities in the range $N(^{12}CO) \sim 10^{16} - 10^{18}$ cm^{-2} and $N(^{13}CO) \sim 10^{15} - 10^{17}$ cm^{-2}, rotational temperatures $T_{rot}(CO) \sim 300 - 700$ K, and Doppler b-values, $b \sim 0.5 - 1.5$ km s^{-1}. I use these results to constrain the line-of-sight density of the warm molecular gas ($n_{CO} \sim 70 - 4000$

cm^{-3}) and put these observations in context with protoplanetary disk models.

2.1. Introduction

Characterizing the gas properties of protoplanetary disks at planet-forming radii ($a \leq$ 10 AU) is critical to understanding the way planets form and evolve. The lifetimes of protoplanetary disks are comparable to the time during which giant planet cores form and accrete gaseous envelopes ($10^6 - 10^7$ yr; Fedele et al. 2010; Hernández et al. 2007; Hubickyj et al. 2005). The surface density of the disk in which the planet forms places limits on the amount of migration that is possible (Trilling et al. 2002; Armitage et al. 2003). The lifetime of the protoplanetary disk determines the amount of time that giant planets are able to accrete, thereby influencing their final masses (Ida & Lin 2004). Observations of carbon monoxide (CO) emission and absorption lines from ultraviolet (UV) to infrared (IR) wavelengths have been shown to be useful probes of molecular gas in the inner disk (Najita et al. 2003; Salyk et al. 2011a; Schindhelm et al. 2012a).

Emission and absorption from the CO Fourth Positive band system ($A\ ^1\Pi - X\ ^1\Sigma^+$) has been widely used to study the interstellar medium (Federman et al. 1980; Burgh et al. 2007), debris disks (Vidal-Madjar et al. 1994), comets (Feldman & Brune 1976; McPhate et al. 1997), planets (Durrance 1981; Feldman et al. 2000), and the atmospheres of cool stars (Carpenter et al. 1994). The first detections of CO far-UV emission and absorption spectral features from the inner regions of protoplanetary disks were presented in France et al. (2011a). The detected CO absorption lines have rotation temperatures $T_{rot}(CO) \approx 500 \pm 200$ K, pointing to an origin in the warm inner disk gas. Molecular hydrogen (H$_2$) and CO absorption were measured simultaneously for the first time by France et al. (2012a) in the disk of AA Tauri. The H$_2$ was seen in absorption against the Lyα emission line, as in Yang et al. (2011), and the CO $A - X$ absorption bands were observed against the far-UV continuum (France et al. 2011b). The value of CO/H$_2 \sim 0.4$ found by France et al. (2012a) is approximately three

orders of magnitude larger than the canonical interstellar value of 10^{-4}. Better constraints on the CO/H_2 ratio are important for determining the total amount of gas in protoplanetary disks.

Many classical T Tauri star (CTTS) disks have been studied with near-IR fundamental (4.7 μm) and overtone (2.3 μm) bands of CO, in both emission (e.g. Carr et al. 1993; Najita et al. 2003; Salyk et al. 2011a), and absorption (e.g. Rettig et al. 2006; Horne et al. 2012). Near-IR CO emission has been used as a tracer of the dominant molecular gas component, H_2, because the homonuclear nature of H_2 makes rovibrational transitions dipole-forbidden and thus difficult to observe at near- and mid-IR wavelengths (Pascucci et al. 2006; Bitner et al. 2008; Carmona et al. 2008; although see Bary et al. 2003; Ramsay Howat & Greaves 2007; and Bary et al. 2008). The CO lines at 4.7 μm appear to originate from the inner disk region with T $\approx$ 500 - 1500 K and Keplerian velocities consistent with the dust sublimation radius. However, some sources have line profiles with excess low velocity emission (Bast et al. 2011), which Pontoppidan et al. (2011) propose arises from a slow molecular disk wind. In general, the IR CO temperatures from LTE slab models (275 - 1675 K, average $\sim$ 1100 K; Salyk et al. 2011a) are higher than those measured from UV CO fluorescence (460 $\pm$ 250 K; Schindhelm et al. 2012a). Rettig et al. (2006) and Horne et al. (2012) studied IR CO absorption from the surfaces of circumstellar disks. Rettig et al. (2006) find CO excitation temperatures of $\sim$ 100 K, likely placing the absorbing gas farther out in the disk at $r > 10$ AU.

The discrepancies between the IR and UV CO work suggests that the observations are probing multiple molecular gas populations, and multiple populations may be responsible for the anomalously high observed CO/H_2 ratio in AA Tau. With deep UV absorption spectroscopy, we have a new observational tool for studies of the inner disk gas. Absorption lines give the most direct measure of the column density and temperature of the disk gas along the line-of-sight as the line fitting is largely independent of the geometry or the photo-exciting source. In order to provide observational constraints on inner disk gas, I present new

analyses of far-UV spectroscopic observations of six (0.6 – 6 Myr) CTTSs. My observations probe the warm disk atmosphere, which is important for constraining the three-dimensional structure of disks in which planets form. In this chapter, I describe the targets and the observations in §2.2. The analysis performed and the model fit parameters are presented in §2.3. The disk geometry and correlations in the data are discussed in §2.4. Finally, §2.5 contains a brief summary of my results.

2.2. Targets and Observations

I analyze far-ultraviolet spectra of six targets that are a subset of the 34 T Tauri stars presented in France et al. (2012b): AA Tau, HN Tau A, DE Tau, RECX-15 (ET Cha), RW Aur A, and SU Aur. HN Tau A and RW Aur A (hereafter HN Tau and RW Aur) are binary stars, but with separations large enough, 1.4" for RW Aur AB and 3.1" for HN Tau AB (White & Ghez 2001), such that only the primary is within the aperture and dominates the emission analyzed here. AA Tau and HN Tau have been studied previously by France et al. (2011a, 2012b), but I refit their spectra with the same procedure as the other targets for consistency. Five targets are in the Taurus-Auriga star-forming region at a distance of 140 pc (Bertout et al. 1999; Loinard et al. 2007). RECX-15 is in the η Chamaeleontis cluster at a distance of 97 pc (Mamajek et al. 1999). Parameters including the age, luminosity, and spectral type of these targets are listed in Table 2.1.

All targets were observed using the *Hubble Space Telescope*-Cosmic Origins Spectrograph (*HST*-COS; Green et al. 2012) under program ID 11616. The COS FUV M-mode wavelength solution is accurate to $\Delta v \sim 15$ km s^{-1} and depends on the object centering[1]. Target acquisition was through the MIRRORB near-UV imaging mode for AA Tau and DE Tau. The rest of the targets were acquired using the MIRRORA mode. Far-UV spectra were obtained using three central wavelengths for G160M, two central wavelengths for G130M,

---

[1]http://www.stsci.edu/hst/cos/ducuments/handbooks/current/cos_cover.html

and multiple focal-plane positions to cover the $1133 \leq \lambda \leq 1795$ Å bandpass while minimizing fixed pattern noise. Table 2.2 lists the dates and exposure times for each object used in this chapter. The data were processed through CALCOS, the COS calibration pipeline, and aligned and co-added with the procedure described in Danforth et al. (2010).

The six targets were the only objects in the T Tauri star sample to show unambiguous CO absorption. The rest of the larger sample either had low continuum signal-to-noise (S/N) making modeling difficult, or were complete non-detections of CO absorption (most likely from low-inclination disks not intercepting the line-of-sight). My optical depth detection limit was $\tau = 5$, below which the absorption depths were comparable to the noise in the data. The targets that I do not fit have inclinations ranging from 4° (TW Hya, Pontoppidan et al. 2008) to 85° (DF Tau, Johns-Krull & Valenti 2001) with an average of 43°. Thus, the majority of the targets that do not show strong CO absorption have lower inclinations. DF Tau is an unusual target discussed in §2.4.3. The six targets that I analyze all have medium-to-high inclination (35° - 77°, with an average of 61°) protoplanetary disks. The average does not include HN Tau, whose inclination is not well known. The inclinations have been determined in a number of different ways, with fairly large uncertainties arising from the techniques used. The inclination of AA Tau was determined by periodic eclipses of the star by the magnetically warped accretion disk combined with a measured line-of-sight projected rotation velocity in the optical (Donati et al. 2010; Bouvier et al. 2003). For DE Tau, it was calculated from stellar radii and rotation periods spectroscopically determined in the IR combined with the literature value of $v \sin i$ in the red (Johns-Krull & Valenti 2001). Optical spectroscopy of a very strong H_α emission line profile was modeled to find the inclination of the disk of RECX-15 (Lawson et al. 2004). The interferometric data of RW Aur was fit with an inclined uniform disk model and was sufficient to constrain the inclination of the disk (Eisner et al. 2007). This inclination is inconsistent with the RW Aur inclination ($\sim 45°$) found by López-Martín et al. (2003) using the ratio of proper motion to radial velocity toward emission knots in the RW Aur jet. The visibility as a function of hour angle in the K-band of SU Aur was fit with a Gaussian brightness profile that was

Table 2.1.   Target Parameters

Object	Spectral Type	A_V	Inclination (degrees)	L_* ($L_\odot$)	M_* ($M_\odot$)	$\dot{M}$ (10^{-8} $M_\odot$ yr^{-1})	$\log_{10}$(Age) (yrs)	Ref.[a]
AA Tau	K7	0.5	70	0.71	0.80	0.33	6.38 ± 0.20	2,4,7,12,16
DE Tau	M0	0.6	35	0.87	0.59	2.64	5.82 ± 0.20	7,10,12
HN Tau	K5	0.5	>40	0.19	0.85	0.13	6.27 ± 0.27	6,7,12
RECX-15	M2	0.0	60	0.08	0.40	0.10	6.78 ± 0.08	13,14,15
RW Aur	K4	1.6	77	2.3	1.40	3.16	5.85 ± 0.53	5,9,11,12,17
SU Aur	G1	0.9	62	9.6	2.30	0.45	6.39 ± 0.21	1,3,8,11,12

[a] (1) Akeson et al. (2002); (2) Andrews & Williams (2007b); (3) Bertout et al. (1988); (4) Donati et al. (2010); (5) Eisner et al. (2007); (6) France et al. (2011a); (7) Gullbring et al. (1998); (8) Gullbring et al. (2000); (9) Hartigan et al. (1995); (10) Johns-Krull & Valenti (2001); (11) Johns-Krull et al. (2000); (12) Kraus & Hillenbrand (2009); (13) Lawson et al. (2004); (14) Luhman & Steeghs (2004); (15) Ramsay Howat & Greaves (2007); (16) Ricci et al. (2010); (17) White & Ghez (2001).

Table 2.2.   *HST*-COS G130M/G160M Observations of Targets

Object	R. A. (J2000)	Dec. (J2000)	Date	G130M Exposure (s)	G160M Exposure (s)
AA Tau	04 34 55.42	+24 28 52.8	2011 Jan 06, 07	5588	4192
DE Tau	04 21 55.69	+27 55 06.1	2010 Aug 20	2088	1851
HN Tau	04 33 39.37	+17 51 52.1	2010 Feb 10	5724	4528
RECX-15	08 43 18.43	-79 05 17.7	2011 Feb 05	3890	4501
RW Aur	05 07 49.51	+30 24 04.8	2011 Mar 25	1764	1617
SU Aur	04 55 59.39	+30 34 01.2	2011 Mar 25	1788	1759

inclined on the sky, giving the best fit inclination for the disk (Akeson et al. 2002). The inclination of HN Tau is not well known, and only a lower limit is given to indicate that an inclination higher than 40° is needed for the line-of-sight to intercept the disk and to explain observed outflows (France et al. 2011a). This lower limit is increased in §2.4.3 by comparing to published models.

The radial velocities of the majority of the stars (listed in Table 2.3) were obtained by Nguyen et al. (2012). The radial velocity for RW Aur A was not measured by Nguyen et al. (2012), but is assumed to be the same as that for the secondary, RW Aur B. The radial velocity of RECX-15 is determined using photospheric Li I absorption lines at 6707.76 Å and 6707.91 Å (Woitke et al. 2011) with resolving power of $\sim 30,000$ (10 km s^{-1} at 6300 Å).

The CO is observed in absorption against the far-UV continuum of these actively accreting stars. The far-UV continuum arises from stellar photospheric and chromospheric emission as well as an accretion continuum (Calvet & Gullbring 1998; France et al. 2011b; Ingleby et al. 2011; see Table 2.1 for the accretion rates). The far-UV continuum may be enhanced in some objects by a molecular dissociation quasi-continuum (Bergin et al. 2004; Herczeg et al. 2004), but the details of this process have not been thoroughly characterized observationally (see, e.g., France et al. 2011b). The continuum emission is absorbed by circumstellar atoms and molecules. Depending on the inclination angle, the light may pass through multiple layers of the disk and thus probe multiple temperature and density regimes. At the high temperatures and column densities of the observed CO (see §3.3), the contribution from interstellar CO is negligible for transitions from $J > 2$. For temperatures typical of the interstellar medium (ISM), states with $J \geq 3$ are not significantly populated. For the extinction values (A$_V \lesssim 1.5$), I would expect an interstellar CO column density of $N(CO) \lesssim 10^{14}$ (see Figure 3 of Burgh et al. 2007), which is orders of magnitude smaller than the circumstellar column densities that I observe. Therefore, my CO measurements do not probe the cold diffuse interstellar material with $<T_{rot}(CO)>_{ISM} \sim 4$ K (Burgh et al. 2007), but arise from material close to the star, likely the warm molecular disk.

Table 2.3.   CO Fit Parameters

Object	$F_{cont}(1420)$ (10^{-15} erg cm^{-2} s^{-1} Å^{-1})	$\log_{10}(N(^{12}CO))$	$\log_{10}(N(^{13}CO))$	$T_{rot}(CO)$ (K)	b (km s^{-1})	v_{CO} (km s^{-1})	v_* (km s^{-1})	v_* Reference[a]
AA Tau	6.1	$16.9^{+0.6}_{-0.7}$	$15.5^{+1.0}_{-1.2}$	450^{+550}_{-250}	$1.4^{+0.7}_{-0.6}$	$+24.7 \pm 18.6$	16.98 ± 0.04	2
DE Tau	3.7	$17.2^{+0.6}_{-0.7}$	$16.0^{+1.0}_{-1.7}$	450^{+1000}_{-300}	$1.4^{+0.6}_{-0.5}$	$+1.4 \pm 15.9$	15.402 ± 0.018	2
HN Tau	7.9	$16.0^{+0.4}_{-0.6}$	$15.2^{+0.7}_{-1.2}$	700^{+1200}_{-450}	$1.4^{+1.3}_{-0.6}$	$+28.0 \pm 21.1$	4.6 ± 0.6	2
RECX-15	4.5	$17.8^{+0.6}_{-0.9}$	$16.7^{+1.2}_{-1.0}$	350^{+1850}_{-200}	$0.5^{+0.3}_{-0.2}$	$+18.2 \pm 11.3$	22	1
RW Aur	22.3	$16.9^{+0.8}_{-1.0}$	$14.7^{+0.7}_{-0.7}$	300^{+600}_{-250}	$0.6^{+0.4}_{-0.2}$	$+20 \pm 20$	15.00 ± 0.03[b]	2
SU Aur	5.6	$17.4^{+0.7}_{-0.9}$	$15.5^{+1.4}_{-1.5}$	350^{+1250}_{-250}	$1.2^{+0.7}_{-0.5}$	$+16.3 \pm 27.3$	14.26 ± 0.05	2

[a](1) Woitke et al. (2011); (2) Nguyen et al. (2012).

[b]Value for RW Aur B

2.3. Analysis

2.3.1. Data Analysis

I identify nine CO bands, $(v' - 0)$, that span the COS far-UV bandpass from the (0 - 0) band at $\lambda \sim 1544$ Å to the (8 - 0) band at $\lambda \sim 1322$ Å (Figure 2.1). I do not fit the (5 - 0) band due to contaminating emission from H_2 and Si IV $\lambda 1394$ Å. The (0 - 0) band is contaminated with C IV $\lambda 1548$ Å emission and is also excluded from the overall fit. Many photo-excited H_2 emission lines populate the spectra, complicating the model spectrum fits as well. All CTTS systems with identifiable CO absorption contain broad bands created by the overlap of many closely spaced rotational lines. This suggests a relatively high rotational temperature, $T_{rot}(CO)$, because as higher-J lines are populated, the observed spectral bands become broader. Broad CO absorption bands were first identified in the spectrum of HN Tau (France et al. 2011a) and later in the spectrum of AA Tau (France et al. 2012a). I employ a similar technique to the previous work, using spectral synthesis modeling to measure $T_{rot}(CO)$ and N(CO) in all six sources.

The spectrum around each band was normalized by a linear fit to the nearby continuum, avoiding regions with H_2 or other emission lines. The least contaminated absorption bands are the (1 - 0), (2 - 0), (3 - 0), and (4 - 0) bands, which also have the strongest oscillator strengths in the Fourth Positive system. However, ^{12}CO and ^{13}CO are not cleanly resolved in the low-v' bands. To isolate these isotopologues, higher-v' bands with larger separations between the ^{12}CO and ^{13}CO bandheads ($v' = 7, 8$) are used to better constrain the column densities of both species (see §2.3.3). There is nearly a 3 Å separation between the isotopes in the (7 - 0) band, compared to the ~ 1 Å separation in the (1 - 0) band. However, these higher bands can sometimes blend into the continuum because of their shallower absorptions. HN Tau in particular does not have detected $v' = 7, 8$ absorption (see §2.3.3). An example of these higher band fits showing separations in the DE Tau (1 - 0) and (7 - 0) lines is shown in Figure 2.2.
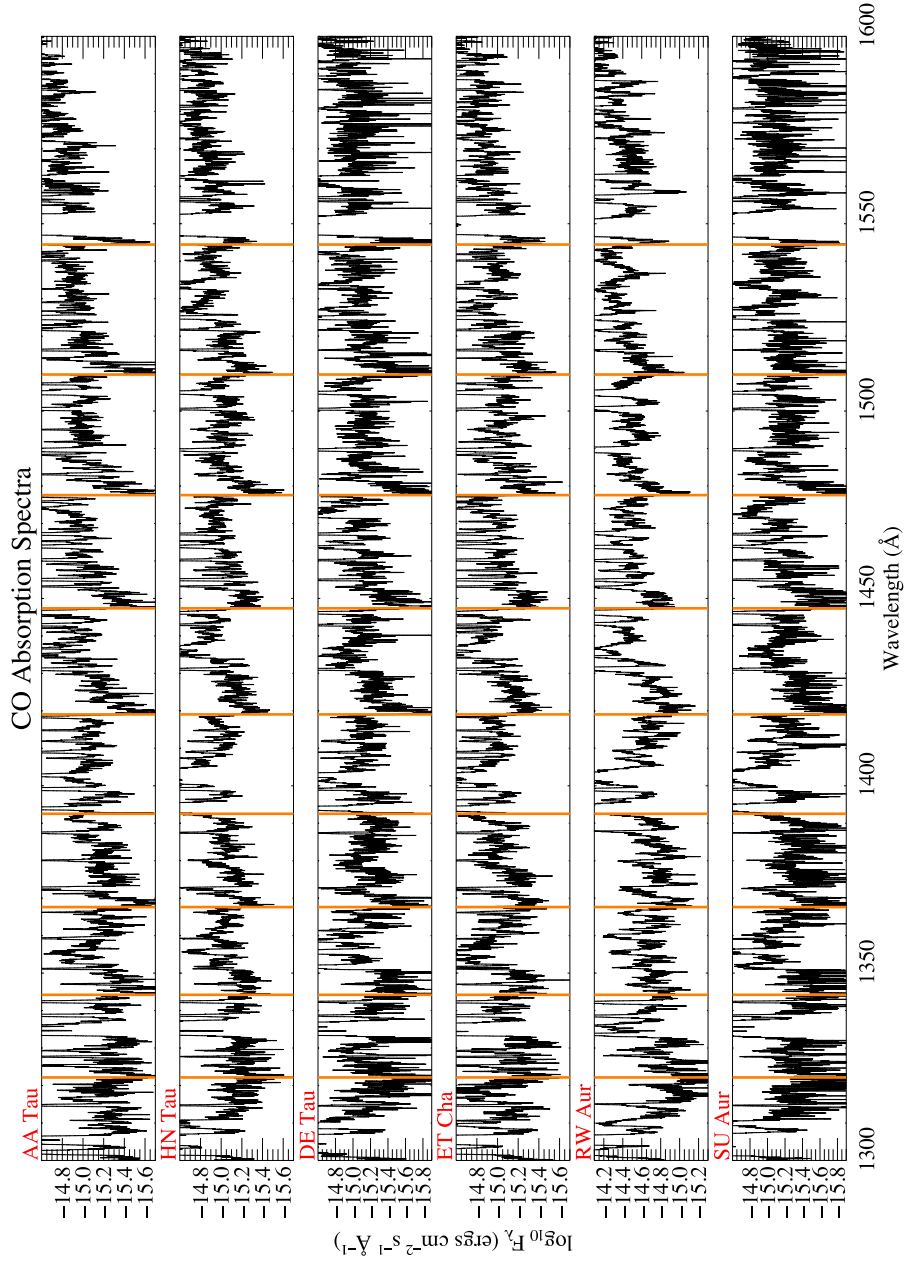
Fig. 2.1.— The nine far-UV CO rovibrational absorption bandheads identified by orange vertical lines. Going from left to right: $(v' - v'' = 8 - 0)$ 1322.1 Å, (7 - 0) 1344.2 Å, (6 - 0) 1367.6 Å, (5 - 0) 1392.5 Å, (4 - 0) 1419.0 Å, (3 - 0) 1447.4 Å, (2 - 0) 1477.6 Å, (1 - 0) 1509.7 Å, (0 - 0) 1544.4 Å. The spectra have been Fourier smoothed to suppress frequencies higher than the 7-pixel spectral resolution.
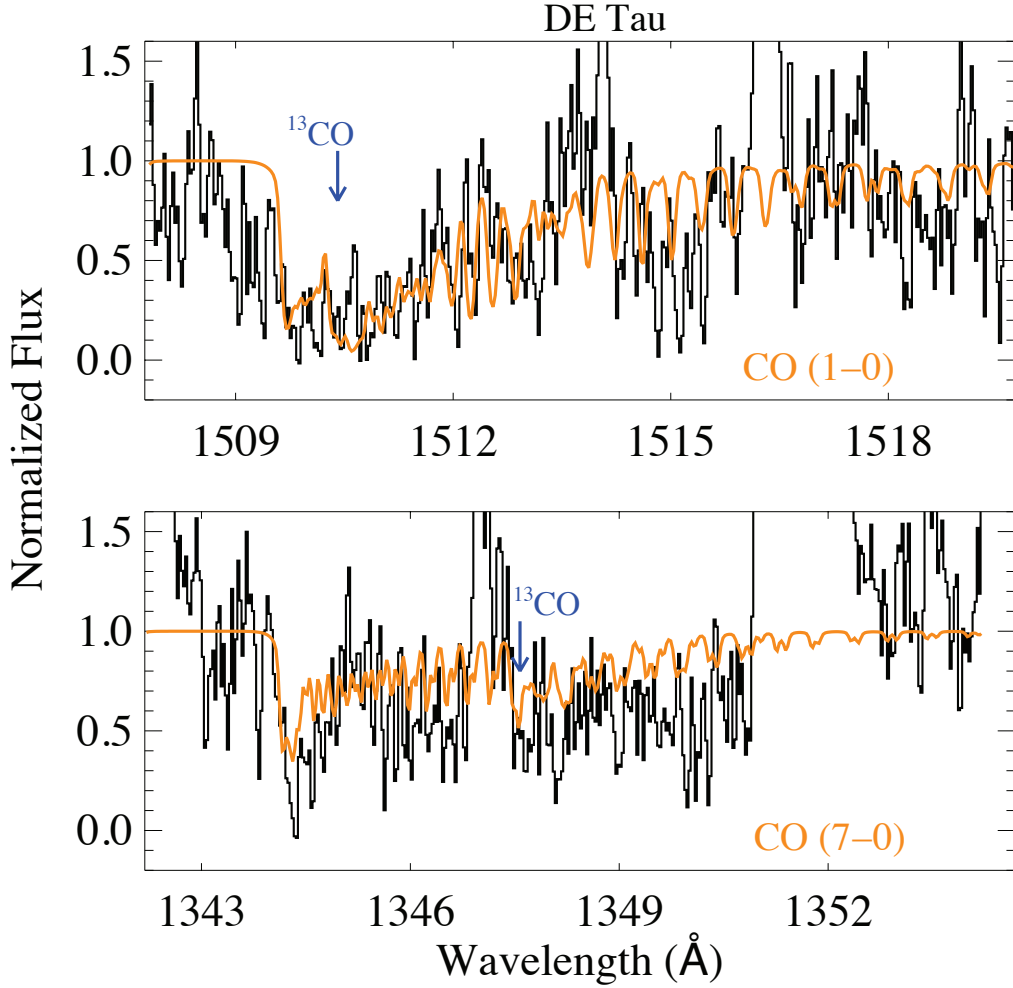
Fig. 2.2.— Low-v' (above) and high-v' (below) model fits for DE Tau showing the larger separation between ^{12}CO and ^{13}CO for larger v'-values. The separation helps to better constrain the ^{12}CO/^{13}CO ratio in the model. The data is in black and the best-fit model is in orange. The first absorption dip in each model is the ^{12}CO bandhead, and the ^{13}CO bandhead is marked with a blue arrow. The high signal-to-noise in the data as well as contaminating emission lines makes this spectral fitting difficult. I set any normalized flux value greater than 1.1 equal to 1.1 during the fitting to mitigate the effect of the emission lines. However, the model is still often driven to lower column densities in order to fit these regions, providing shallower absorption models, which can be seen in the (7 - 0) band fit.

The normalized data vary in both the depth of their absorptions and the number of excited J-lines present. DE Tau and SU Aur have the largest depths, but the data are also noisier, making it harder to determine a continuum level. The depths will vary, even for similar column densities, because of the error associated with the continuum fit and population shifts in the lower-J levels due to increases and decreases in temperature (see §2.3.2). Because the absorptions in these targets are very saturated (see §2.3.3), changing the column density does not affect the absorption depth highly at low-J values. Here, the normalization will have a bigger effect. At high-J values (longer wavelengths within the band) it is difficult to pinpoint the weaker absorptions amongst the emission lines and the noise in the data. This makes the data harder to interpret, though RW Aur does have a significant lack of high-J lines compared to the other targets. HN Tau, however, has fairly prominent high-J lines. All of these factors contribute to the derived molecular parameters and errors described in §2.3.2 and §2.3.3.

2.3.2.   Model Description and Fitting Procedure

The CO absorption profiles were modeled for ^{12}CO using the oscillator strengths and rovibrational line wavelengths from Eidelsberg (private communication). The A $^1\Pi$ energy levels of Haridass & Huber (1994) were used to calculate the ground state energies. The oscillator strengths for ^{13}CO are taken from Eidelsberg et al. (1999), and the wavelengths and oscillator strengths for the perturbation states were taken from Eidelsberg & Rostas (2003). A common rotational temperature was assumed for both ^{12}CO and ^{13}CO.

All six of the analyzed bands ($v' = 1, 2, 3, 4, 7, 8$) were compared to model spectra for a grid of different values of the Doppler b-value, rotational temperature, $T_{rot}(CO)$, and logarithmic column density of both ^{12}CO and ^{13}CO, $\log_{10}(N(^{12}CO))$ and $\log_{10}(N(^{13}CO))$. The model also includes a velocity shift parameter (explored in more detail in §2.4.1), which I originally estimated by eye from the (2 - 0) band of each target by varying the velocity

shift until the bandheads of the model and data coincided. However, after a more rigorous treatment of the velocity shifts, using all the bands with uncontaminated bandheads to constrain the location of the CO gas in the disk, more reliable values are found in §2.4.1. The ranges of my grid search was $0.5 - 2.0$ km s^{-1} in steps of 0.1 km s^{-1} for the Doppler b-value, $300 - 1000$ K with steps of 50 K for the rotational temperature, $16.0 - 18.0$ in steps of 0.1 for $\log_{10}(N(^{12}CO))$, and $14.0 - 17.0$ in steps of 0.1 for $\log_{10}(N(^{13}CO))$. The maximum b-value for my grid search comes from my assumption of turbulent velocities $\lesssim 1$ km s^{-1} and CO rotational temperatures $\lesssim 5 \times 10^3$ K. The maximum $\log_{10}(N(^{12}CO))$ value for the search comes from the analysis of France et al. (2012a), who argue that any larger column of ^{12}CO would lead to a column of hydrogen that would extinguish the stellar flux around the Lyα line center, which is inconsistent with my observations. This limit is confirmed after the fit as the majority of the targets (except those with the highest column, RECX-15 and SU Aur) are inconsistent with a column of 10^{18} cm^{-2} within their errors. Any ^{12}CO column density lower than my lower limit of 10^{16} cm^{-2} (which corresponds with my optical depth detection limit of $\tau = 5$) would be very difficult to detect with the S/N, setting the lower bound on my column density search. An example of the CO model is shown in Figure 2.3. The higher rotational states are excited at higher temperatures while the lower rotational states are depopulated. Thus, the observed absorption band becomes wider and shallower with increasing temperature if column density is kept constant. The three simulated spectra at the top of Figure 2.3 are at the native model resolution ($\Delta v \sim 2$ km s^{-1}) and the bottom spectrum is at the resolution of the HST-COS instrument ($\Delta v \sim 17$ km s^{-1}). The CO absorption lines are narrower than the instrumental resolution. The unresolved line cores do not go to zero at the observational resolution even when the CO optical depths are large.

Because the statistical errors in the data were sometimes anomalously small[2], such that a reduced χ^2 fitting routine with non-uniform errors gave erroneous results, I employed a

---

[2]The CALCOS pipeline is known to mishandle statistical errors in the low S/N regime (Froning et al. 2011)
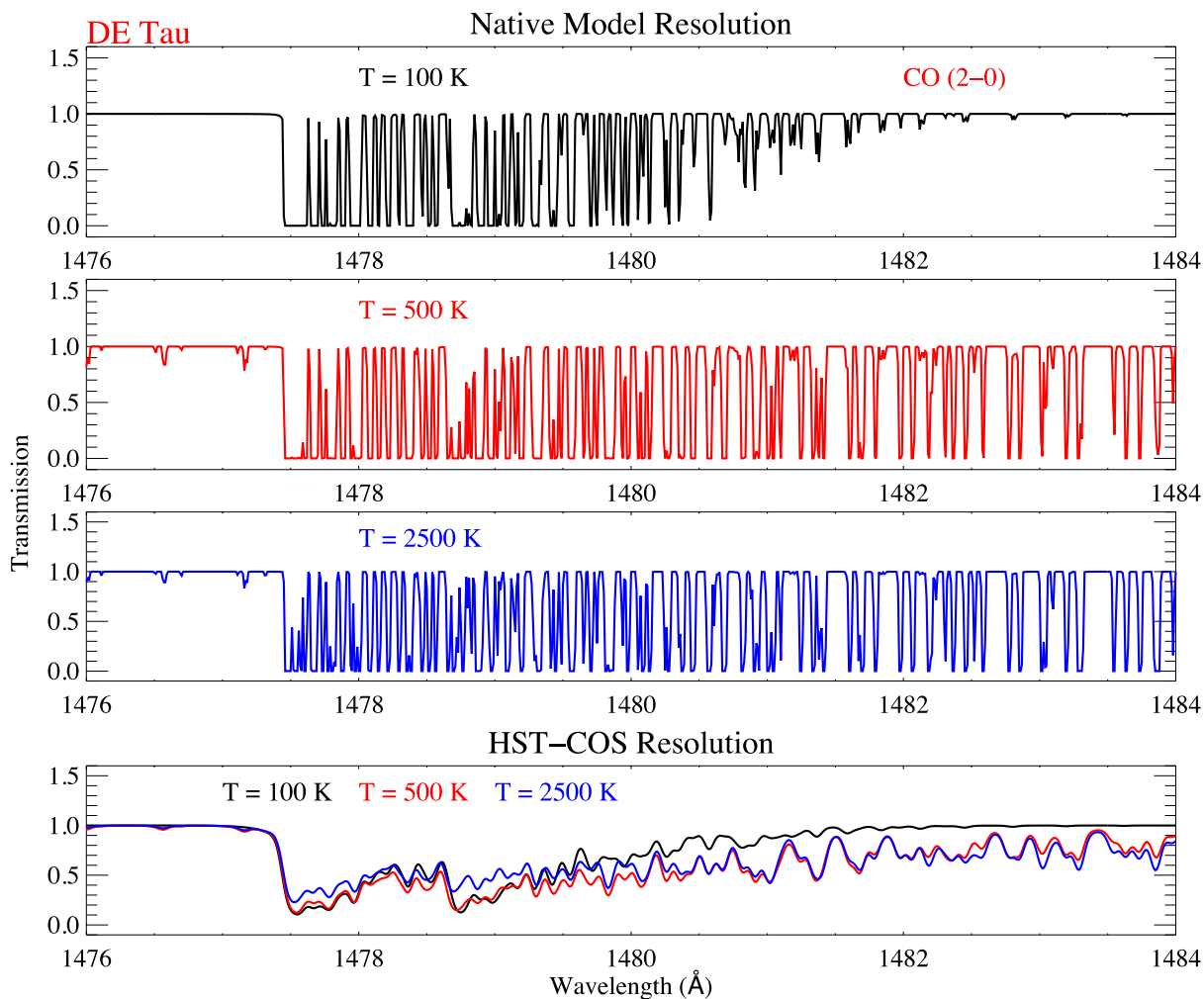
Fig. 2.3.— Three different CO models for the (2 - 0) band of DE Tau with identical Doppler b-value = 1.4 km s^{-1}, $\log_{10}(N(^{12}CO)) = 17.2$, $\log_{10}(N(^{13}CO)) = 16.0$, and velocity shift = 1.4 km s^{-1}. (Top 3): Model output with native model resolution ($\Delta v \sim 2$ km s^{-1}). (Bottom): Model output after being convolved with the *HST*-COS linespread function ($\Delta v \sim 17$ km s^{-1}) to simulate data detected with the instrument.

simple least squares fitting routine that minimizes the square of the difference between the model and the data. This procedure weighted all data points equally, giving a more reliable fit. Because of the presence of emission lines (mostly H_2), I truncated the data above a normalized flux level of 1.1 so that the emission features did not contaminate the absorption model fitting. This does, however, cause the model to fit a truncated continuum value instead of the absorption at times when the emission lines wipe out the absorption. The model is pulled toward a solution with lower column density to fit the higher flux values at these points, introducing a bias which contributes to the large errors on the column density in Table 2.3.

The model uses the five input parameters to create a theoretical spectrum. The Doppler b-value, along with the column density, determines the opacity of the model, and the temperature determines the band shape as discussed above, with higher temperatures leading to wider, shallower absorption models. The column density inputs determine the relative depth of the ^{12}CO and ^{13}CO absorption bands. The $^{12}CO/^{13}CO$ ratio is primarily determined by the differences in the absorption depths at the relevant bandheads. At the high column densities of these disks (see §2.3.3), most of the targets are on the flat portion of the curve of growth (COG) for the lower-J ^{12}CO lines of the lower-v' bands. This means that increasing the column density of ^{12}CO does not lead to a significant increase in the absorbed flux. The column density fits rely more on the ^{13}CO absorption and the higher-v' bands and higher-J lines of ^{12}CO, which are less saturated. The velocity shift parameter moves the absorption band of the model to shorter or longer wavelengths corresponding to the gas moving toward or away from the observer, respectively. The theoretical spectrum is then convolved with the COS linespread function and compared to the observations to find the best-fit parameter values.

2.3.3. Model Fits and Errors

The fits to the normalized absorption data are shown in Figure 2.4a - Figure 2.4f and the parameter values are provided in Table 2.3. DE Tau and SU Aur, which have the deepest absorptions, have higher column densities in both ^{12}CO and ^{13}CO than most of the other targets. The shallower low-J lines combined with the prominent high-J lines in HN Tau require a higher temperature and lower column density to fit the data. Most of the targets share a common best-fit temperature (~ 350 K), with HN Tau being an outlier because of the more prominent high-J lines. The column densities are much more varied, with large uncertainties because of the high-J lines blending in with the low S/N continuum and contamination by emission lines. Unlike the temperature, there is no common best-fit column density for all of the targets within the uncertainties. An intersystem band not taken into account in the code (a' $^3\Sigma^+ - X$ $^1\Sigma^+$ (14 - 0)) at $\lambda = 1419.50$ Å (Eidelsberg & Rostas 2003) hinders the fit of the (4 - 0) band of HN Tau, the highest temperature target. This absorption is between the ^{12}CO and ^{13}CO bandheads, causing the data to be deeper than the model in this part of the spectrum. A few targets also show this difference in the (2 - 0) band as well, which could be another intersystem band.

My fit values for all six targets lie in the ranges of $b = 0.5 - 1.4$ km s^{-1}, $T_{rot}(CO) = 300 - 700$ K, $\log_{10}(N(^{12}CO)) = 16.0 - 17.8$, and $\log_{10}(N(^{13}CO)) = 14.7 - 16.7$. The errors were estimated by taking the standard deviation of the χ^2 distribution with appropriate degrees of freedom. Increasing the minimum χ^2 value by the standard deviation determined the best-fit parameter range. I define errors as the width of the best-fit parameter space, as defined by the standard deviation of the χ^2 distribution. This error procedure is illustrated in Figure 2.5. The errors on $\log_{10}(N(^{13}CO))$ were more difficult to define because of the lower column density of ^{13}CO. For $\log_{10}(N(^{13}CO)) \lesssim 14$, the χ^2 value does not increase substantially as the column density is decreased because I am no longer detecting the absorption. I take a lower limit on the column density of ^{13}CO of 10^{14} cm^{-2} for this reason. Within the errors, HN Tau, RW Aur, and SU Aur are consistent with a non-detection of ^{13}CO (column density
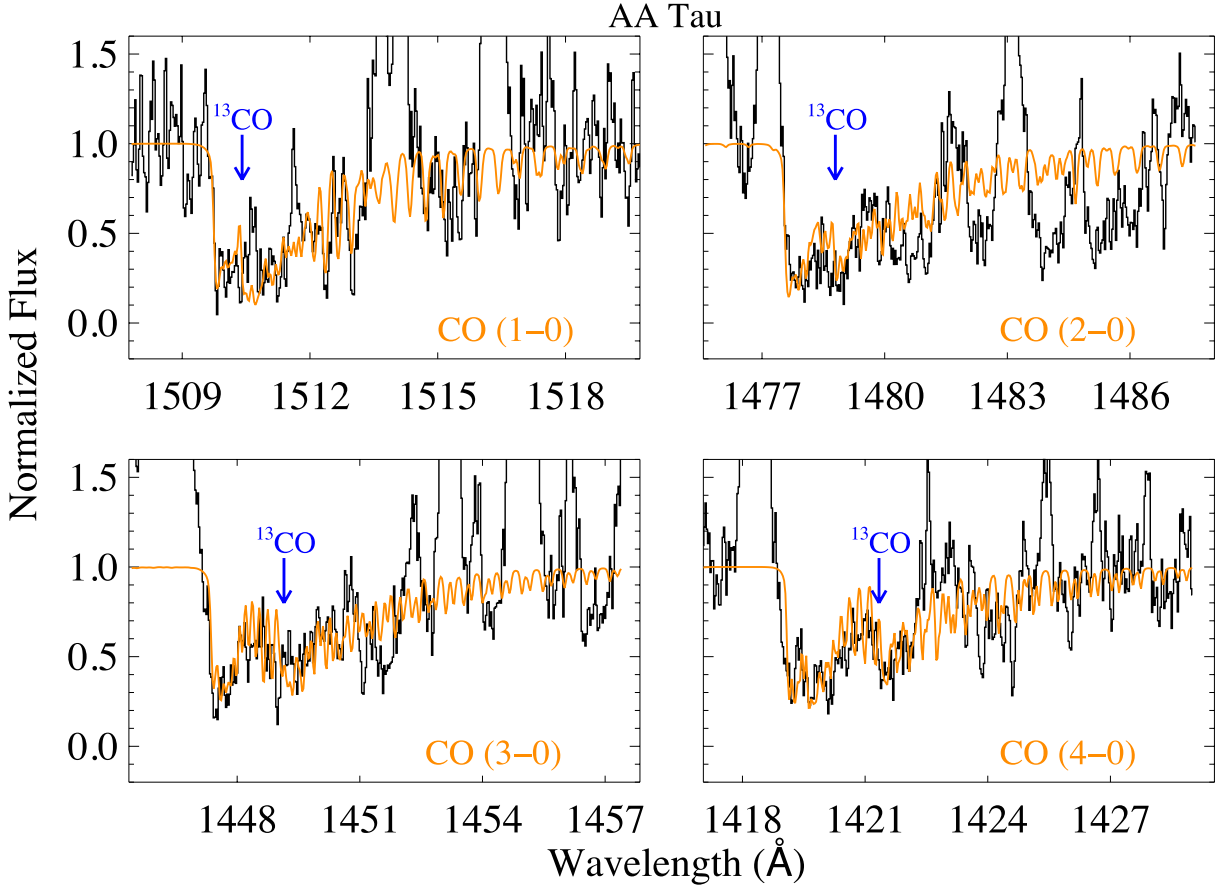
Fig. 2.4a.— Low-v' model fits (orange) for AA Tau. The best-fit values (see Table 2.3) for the Doppler b-value, $T_{rot}(CO)$, $\log_{10}(N(^{12}CO))$, $\log_{10}(N(^{13}CO))$, and velocity shift are used. The data (black) are continuum normalized and the ^{13}CO bandheads are marked to clearly show the two different CO species. The emission contaminating the absorption is not included in the model and any flux above a normalized value of 1.1 is truncated during the fit.
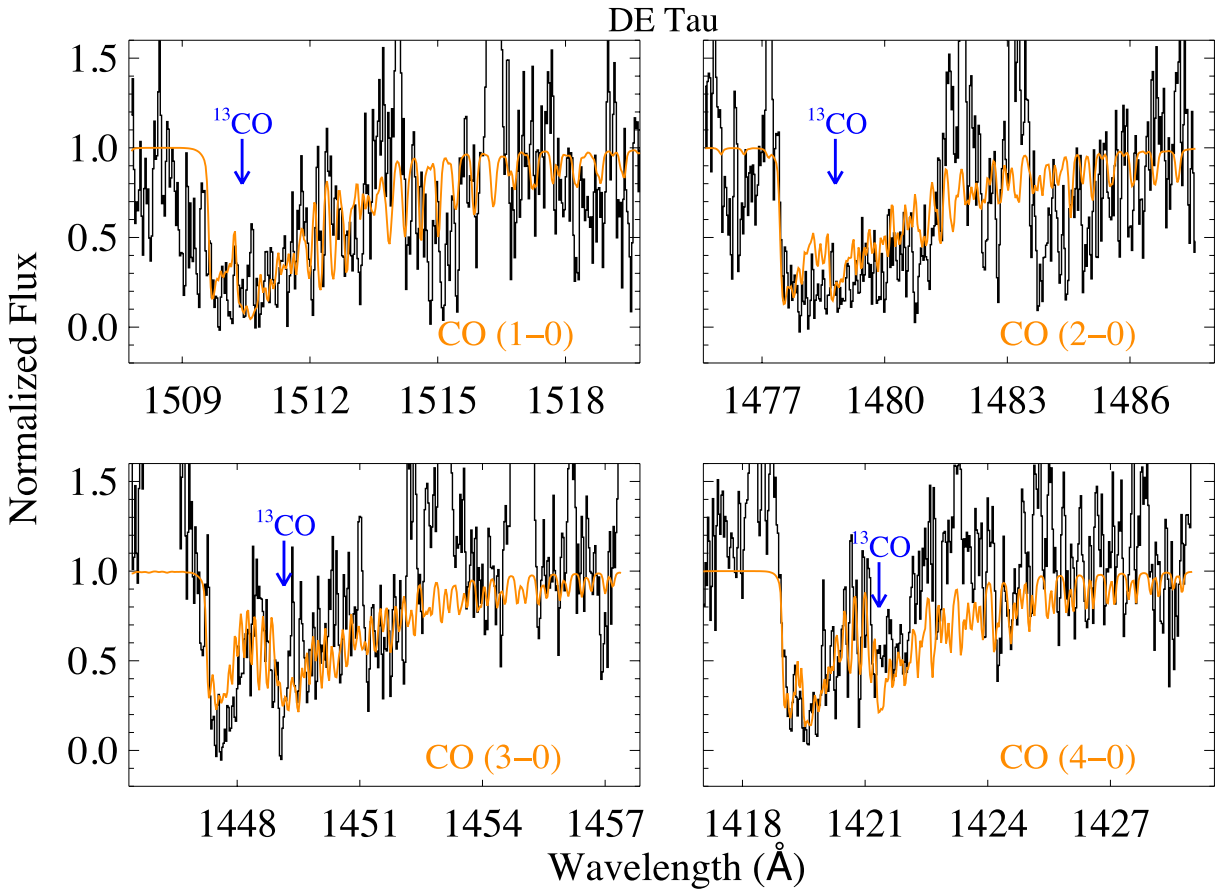
Fig. 2.4b.— Same as Figure 2.4a for DE Tau.
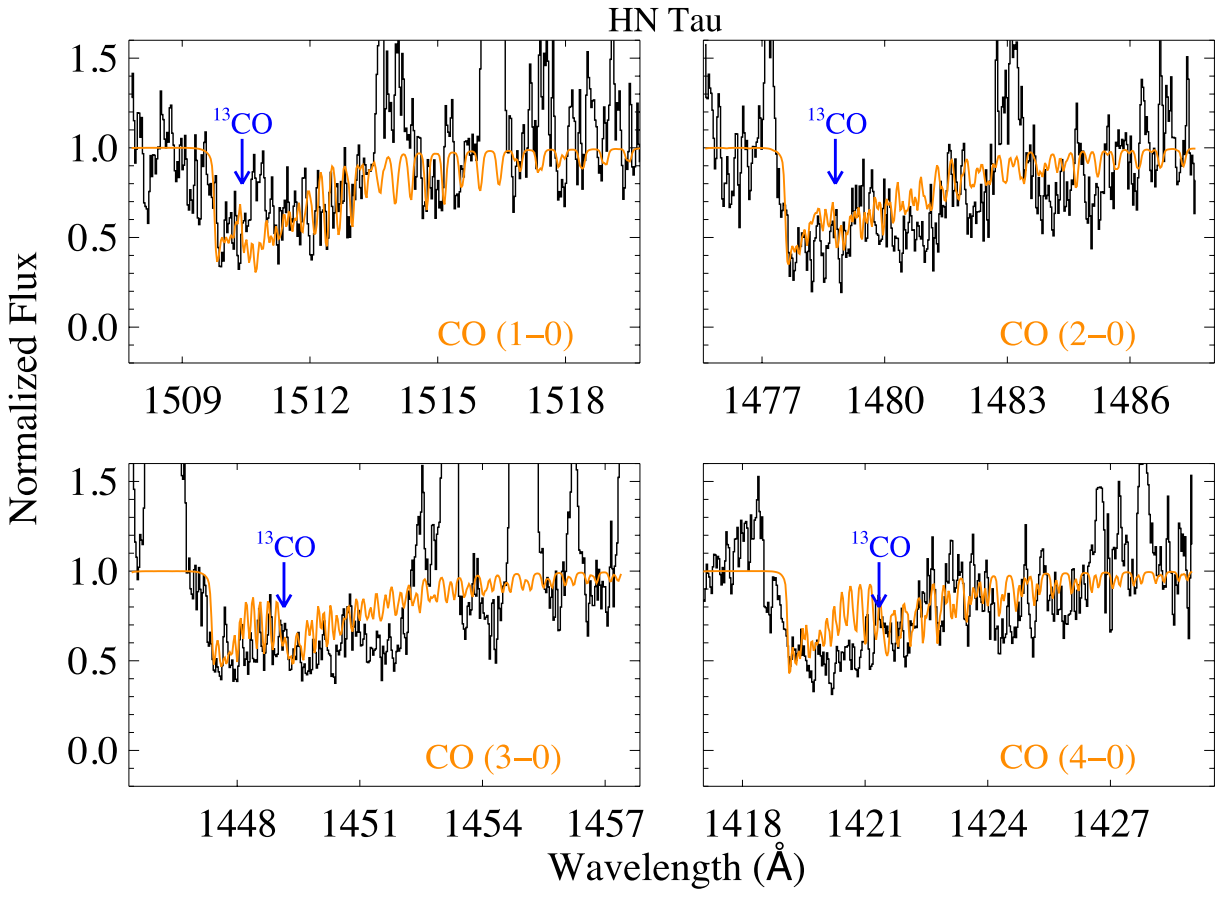
Fig. 2.4c.— Same as Figure 2.4a for HN Tau.
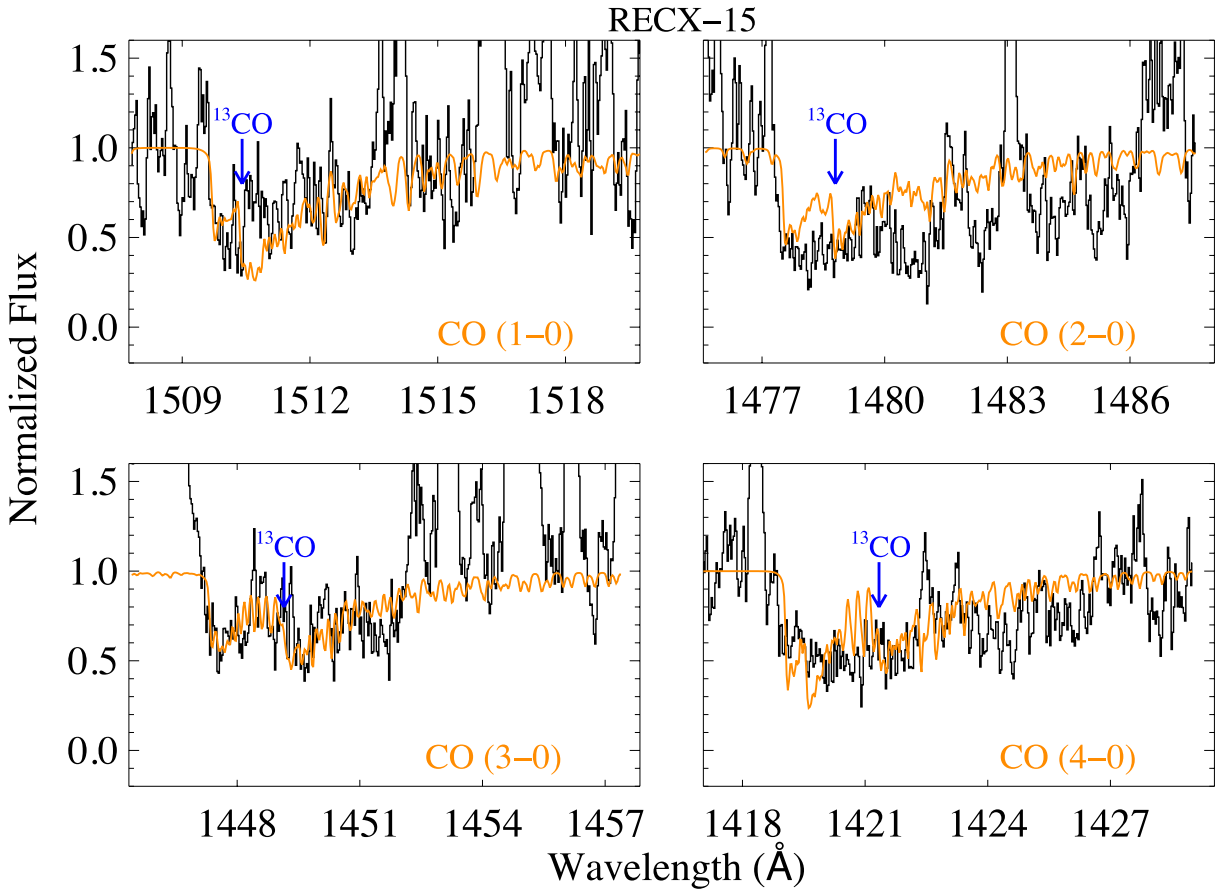
Fig. 2.4d.— Same as Figure 2.4a for RECX-15.
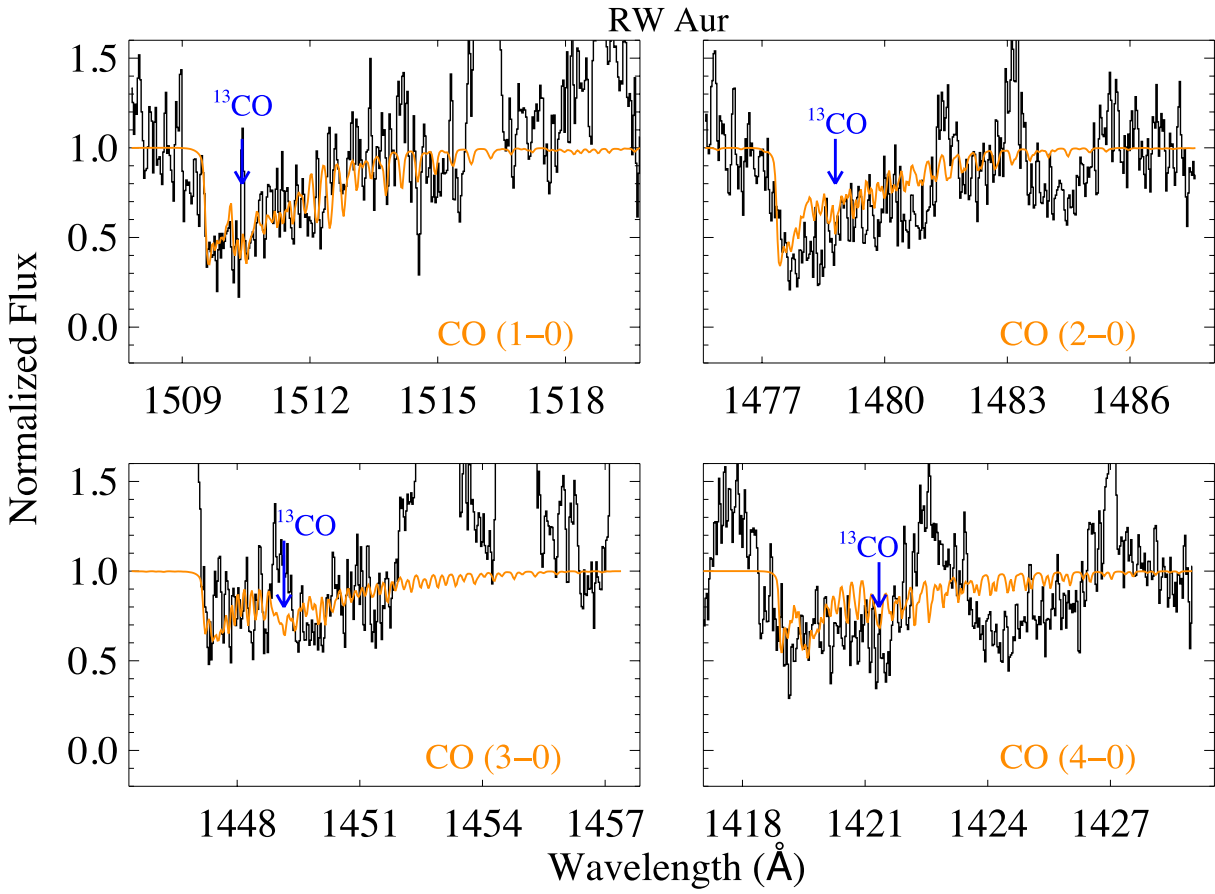
Fig. 2.4e.— Same as Figure 2.4a for RW Aur.
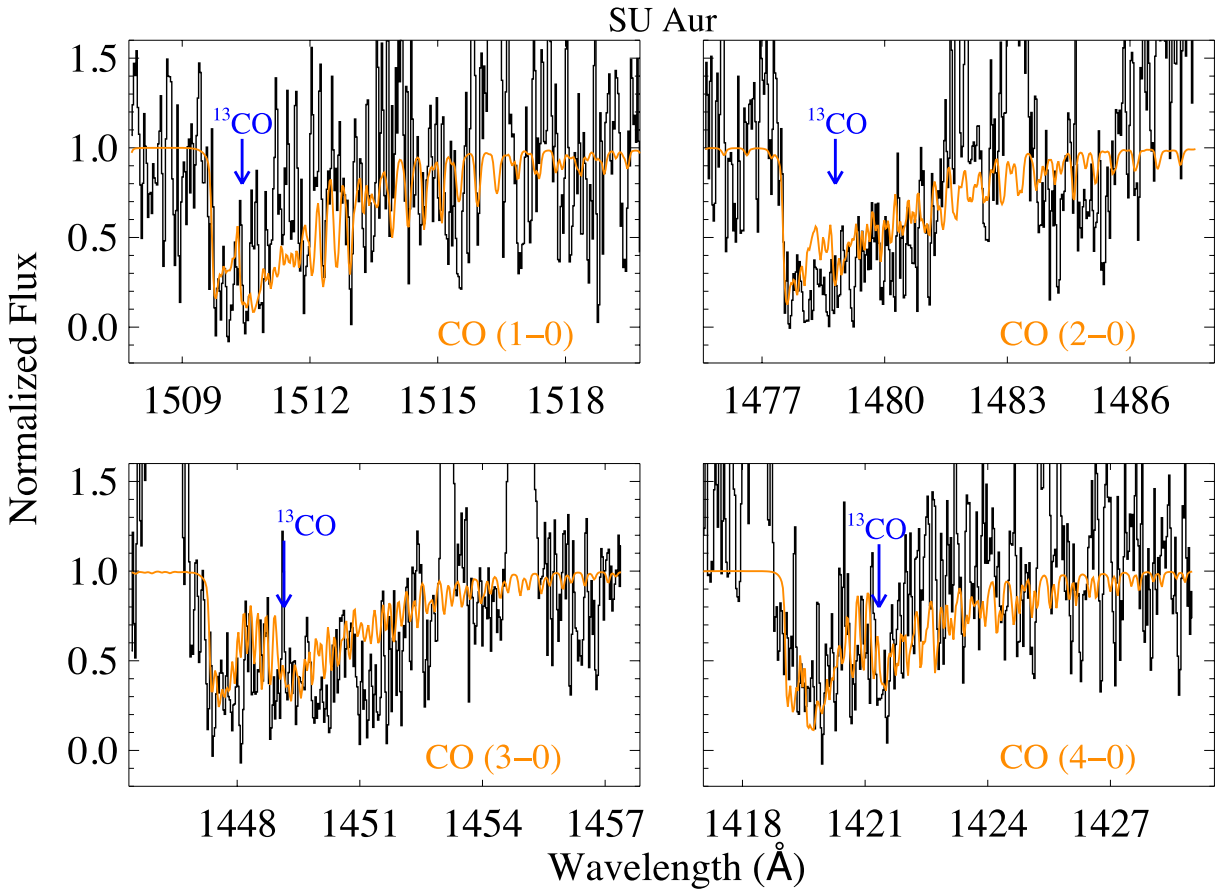
Fig. 2.4f.— Same as Figure 2.4a for SU Aur.

of ^{13}CO $< 10^{14}$ cm^{-2}). The temperatures in general tend to have large upper error bars. Higher temperatures populate the higher J-states, which produce weaker absorption lines due to smaller column densities. Due to the low S/N in the data, these weak lines blend into the continuum making the high temperature limit difficult to constrain. At temperatures $\gtrsim$ 1000 K, the (v' - 1) rovibrational bands of CO should be detectable ($\tau \geq 5$) in the data at my best-fit column densities. At my best-fit temperature of $\sim$ 350 K, the (v' - 1) band would be detected for $\log_{10}(N(^{12}CO)) \gtrsim 18.0$. However, I do not detect any of these bands, which suggests that the CO gas is not at densities much greater than 10^{18} cm^{-2}, or at temperatures much greater than 1000 K, though my models of the (v' - 0) bands alone do not provide strong constraints on the high end of the temperature range. I find similar results within the errors for AA Tau to the absorption line analysis of France et al. (2012a). My b-values are much higher than those found with sub-millimeter observations of the disk of TW Hya ($b \lesssim 0.04$ km s^{-1}) by Hughes et al. (2011), however, this could be a consequence of their observations probing colder, more quiescent CO gas at disk radii of $\sim$ 100 AU.

The errors are driven mainly by three sources: continuum determination, low S/N, and saturation in the absorption lines. Estimates of the continuum fluxes are difficult due to the large number of emission lines in these spectra, especially the emission coincident with the absorption bands. The error in the determination of the continuum flux is $\sim$ 20%, leading to an error on the column densities of $\sim$ 0.25 dex. The low S/N in the continuum (S/N per resolution element $\sim$ 7 for AA Tau) and absorption lines also contribute to the errors. Typical continuum flux values at $\lambda 1420$ Å are listed in Table 2.3. At these low fluxes, the absorbers could not be detected with the Space Telescope Imaging Spectrograph (STIS), and have only recently been detected with COS. Saturation in these lines also leads to a degeneracy between the column densities and the Doppler b-values. I include higher-v' bands in my fit as they have smaller oscillator strengths and are therefore less saturated.

The line optical depths for all the targets (except HN Tau) are of order 100 – 600 for the low-v' transitions ($v' = 0$ - 6) up to J-values of 15 to 25, which puts these lines on the
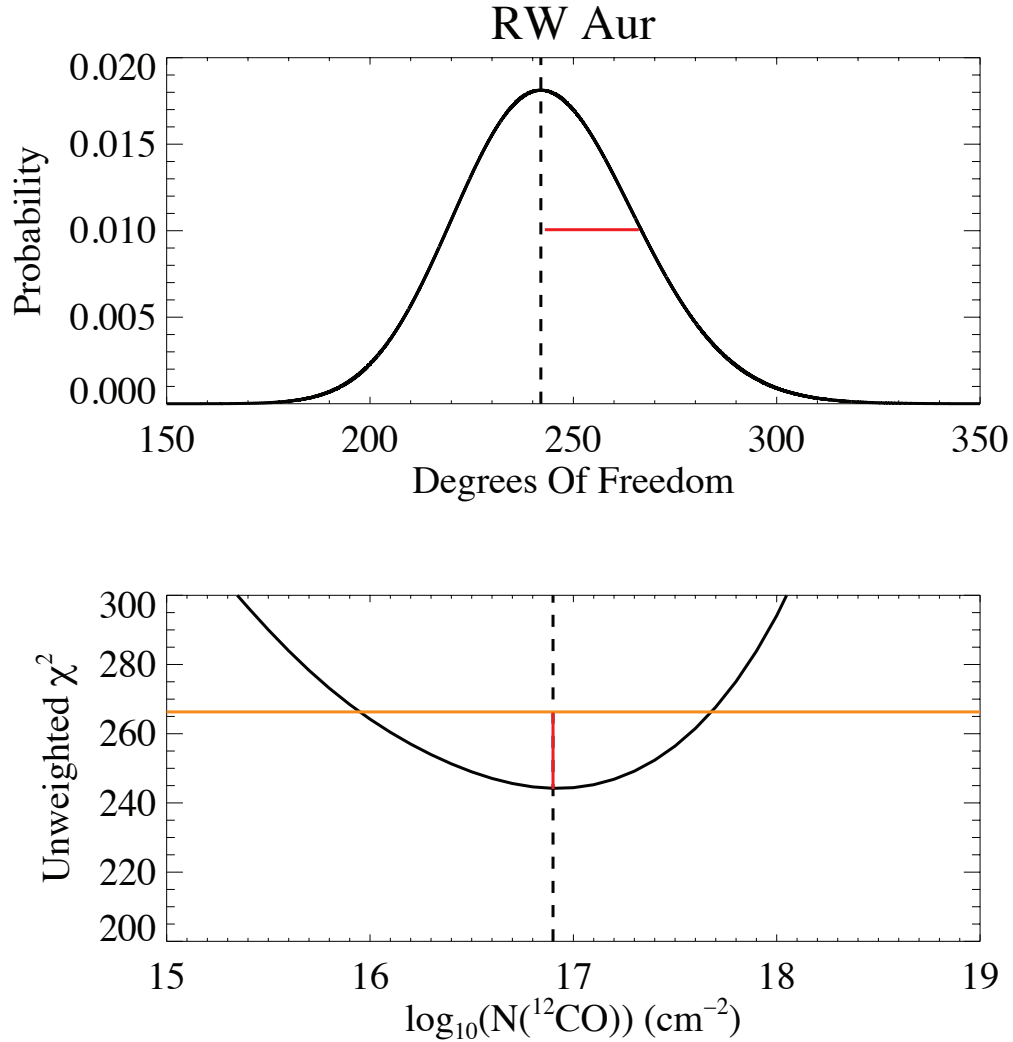
RW Aur

Fig. 2.5.— Illustration of the uncertainty determination. (Above): A plot of the χ^2 distribution for the degrees of freedom of RW Aur. The standard deviation of the distribution is shown in red; the mean is defined by the dashed line. (Below): A plot of the unweighted χ^2 value as a function of $\log_{10}(N(^{12}CO))$. I increased the minimum χ^2 by the standard deviation of the distribution to define my error region. The dashed line shows the best-fit column density for RW Aur ($10^{16.9}$ cm^{-2}), the red line shows the standard deviation of the above χ^2 distribution, and the orange line defines the error region where it crosses the unweighted χ^2 line.

flat portion of the COG. HN Tau, however, has optical depths of about 20 or less for all v' transitions and even reaches optical depths of order unity in the models for the (7 - 0) band and therefore was undetected in the observations. The lower optical depths are caused by the higher temperature and higher b-value of HN Tau. The higher temperature (700 K) of HN Tau lowers the line strength of each J-line compared to if the gas was cooler by distributing the absorption over more transitions. Similarly, the higher b-value (1.4 km s^{-1}) lowers the line center cross-section through larger Doppler broadening spreading out the cross-section in wavelength space. The product of the lower line strength and lower cross-section in each J-line leads to a significantly lower optical depth for HN Tau. None of the other targets approach optical depths as small as 1 until the high-J levels of the $v' = 7, 8$ states.

2.4. Results and Discussion

2.4.1. CO Velocity and Isotopic Fraction

The radial velocities of the CO absorption lines listed in Table 2.3 were obtained with a simple least squares fit. Assuming the best-fit parameters of the CO model, velocity shifts from -200 km s^{-1} to +200 km s^{-1} with 1 km s^{-1} intervals were explored. Due to low S/N, the (8 - 0) band was not used in the velocity calculation. The average and standard deviation of the velocity shifts for the observed bands were taken as each target's velocity and velocity error. Shifting the velocity moves the model high-J CO lines relative to the observed spectra, which can change the best-fit temperature. However, the temperature would change by only ~ 50 K, which is well within the errors. The range of acceptable velocities was small enough that the best-fit parameters from the model were not affected by the shift.

Since RW Aur contains strong, redshifted H$_2$ emission lines (France et al. 2012b), which sometimes places the emission on top of the CO absorption bandhead, I checked the velocity shift by hand. I required that the bandhead of the model and data match for the (1 - 0), (2 - 0), and (4 - 0) bands, which are the cleanest and strongest absorption bands. The best-fit

velocity shift is $+20$ km s^{-1}, consistent with the stellar radial velocity ($+15$ km s^{-1}) in the literature (Nguyen et al. 2012). The fit starts to become noticeably worse at ± 20 km s^{-1} from the best-fit value, which I take as the error.

The fitted CO absorption line velocities are generally consistent with the radial velocities of the stars from the literature to within the 15 km s^{-1} absolute uncertainty in the COS wavelength scale. However, the CO absorption in DE Tau appears to be somewhat blueshifted relative to the stellar velocity (see Table 2.3), but is still consistent within the errors. As noted by Nguyen et al. (2012), the low stellar radial velocity of HN Tau (4.6 km s^{-1}) deviates from the average velocity of the Taurus-Auriga star-forming region (~ 15 km s^{-1}; Hartmann et al. 1986). The quoted stellar radial velocity of HN Tau is inconsistent with my CO velocity, but is only slightly outside my errors. These small velocity differences between the CO absorption and the star ($\Delta v = 2.04$ - 23.4 km s^{-1}) indicate that the CO is approximately at rest in the stellar frame, or at least not in a fast-moving disk wind. This is in agreement with studies presented by Bast et al. (2011) and Najita et al. (2003) who find CO emission generally consistent with stellar velocities, with average velocity difference $\Delta v \sim 3.5$ km s^{-1}. However, the possibility of a slow-moving disk wind, such as described in Pontoppidan et al. (2011), cannot be fully ruled out as an explanation for the location of the absorbing CO gas in my targets.

The best-fit $^{12}CO/^{13}CO$ ratio in my sample disks ranges from $\approx 6 - 158$ (See Table 2.4). The errors in these ratios, however, are very large because of the order of magnitude errors in the column densities. My isotopic ratios are all consistent with the interstellar value of $^{12}CO/^{13}CO \sim 70$ (Sheffer et al. 2007) and the young stellar object environment value of ~ 100 found by Smith et al. (2009), but the S/N and spectral resolution are not optimal for making a precise determination of the isotopic ratio in the disk.

2.4.2. CO Temperature and Density

I now compare my CO absorption temperatures and column densities to other gas measurements of the inner disk in the literature. The rotational excitation temperatures of the disks (300 – 700 K) agree well with the analyses of UV fluorescent CO emission lines (460 ± 250 K) in Schindhelm et al. (2012a) for disks around similar CTTSs. In contrast, the average rotational temperature of the full disk sample of Salyk et al. (2011a) is ∼ 1100 K, albeit with a large range, which is higher than my sample average of ∼ 400 K. The difference is only marginally significant, although suggestive, due to the large uncertainties on the upper limit of the UV CO temperature distribution (see §3.3). For a direct comparison, the model fit to the AA Tau near-IR CO emission by Salyk et al. (2011a) finds a rotation temperature of 950 K and $\log_{10}(N(CO))$= 18.6, which are both higher than my parameter values for the same target. Horne et al. (2012) find a CO column density for AA Tau of 1.2×10^{19} cm^{-2}, also higher than my value. I compare the Salyk et al. (2011a) and Horne et al. (2012) CO parameters for AA Tau to my fit by using their column density and temperature values in my model and plotting them with mine in Figure 2.6. I assume a ^{12}CO/^{13}CO ratio of 70, my b-value, and my velocity shift value for the other models. The other models do not appear to be consistent with my models or data. Because emission line studies probe a much larger region of the disk than the single line-of-sight of absorption line studies, it is not surprising that the Salyk et al. (2011a) study appears to probe a different molecular gas population. The higher temperature gas may be located at a disk height larger than the line-of-sight sampled in my absorption line measurements. The UV spectra may also be preferentially sensitive to lower column density gas due to extinction effects. However, the apparent inconsistency between my model and the Horne et al. (2012) model for AA Tau is surprising because they are both absorption line studies. It may be that the near-IR continuum emission and the UV continuum emission are produced in different locations, so that the lines-of-sight to them are different. Alternatively, if the CO is located in the inner disk, then the difference may be related to the warp of the inner disk, which varies with the

rotation of the star (Bouvier et al. 2007a). The temperature fits to the data show that it is inconsistent with a temperature of 2500 K, the H_2 emission/absorption line temperature found by France et al. (2012a,b) in these disks, and the H_2 fluorescence temperature for TW Hya, modeled by Herczeg et al. (2004) and Nomura & Millar (2005). Assuming that both the CO and H_2 are in local thermodynamic equilibrium, the hot H_2 emission appears to be spatially separate from the CO absorption.

Assuming that my CO rotational temperatures are representative of gas kinetic temperatures $T_{gas} > 300$ K, I estimate the maximum radius where warm CO can be maintained at this temperature (from Figure C.2 of Woitke et al. 2011) to be $r_{CO} \approx 10$ AU. This is consistent with the UV CO emission studied by Schindhelm et al. (2012a) who find that the emission arises from radii $\gtrsim 2$ AU in similar disks. Far-UV CO emission is spectrally unresolved from RECX-15, implying that $r_{CO} \geq 3$ AU. I estimate the number density of the CO in these disks by dividing my column densities by this radius:

$$n_{CO} = \frac{N(^{12}CO)}{r_{CO}} \tag{16}$$

The estimated CO number densities are in the range of $n_{CO} \sim 70 - 4000$ cm^{-3}, and are shown in Table 2.4. With these densities, I computed the CO/H_2 ratio required for the CO to be thermalized up to $J = 25$ (the highest J-state that could be reliably identified in my data). If I assume that collisions with H_2 are the leading contributor to the CO level populations, and that the H_2 density is sufficiently high, then the kinetic temperature will equal the CO rotational temperature, $T_{rot}(CO)$. Significant photoexcitiation would decouple the two temperatures. I computed the H_2 critical density (the density where the spontaneous emission rate equals the collisional de-excitation rate) assuming an H_2 ortho/para ratio of 3 and using collision rates calculated by summing over all collisional routes (Yang et al. 2010) downward out of level $J = 25$. The H_2 critical density for CO excitation in the range 300 – 750 K is $\approx (5.3 - 4.2) \times 10^6$ cm^{-3}. The CO/H_2 ratios needed to thermalize the absorption lines are listed in Table 2.4. They are upper limits and range from $1.6 \times 10^{-5} - 7.9 \times 10^{-4}$. For the CO densities derived with the assumed Woitke maximum radius, typical interstellar
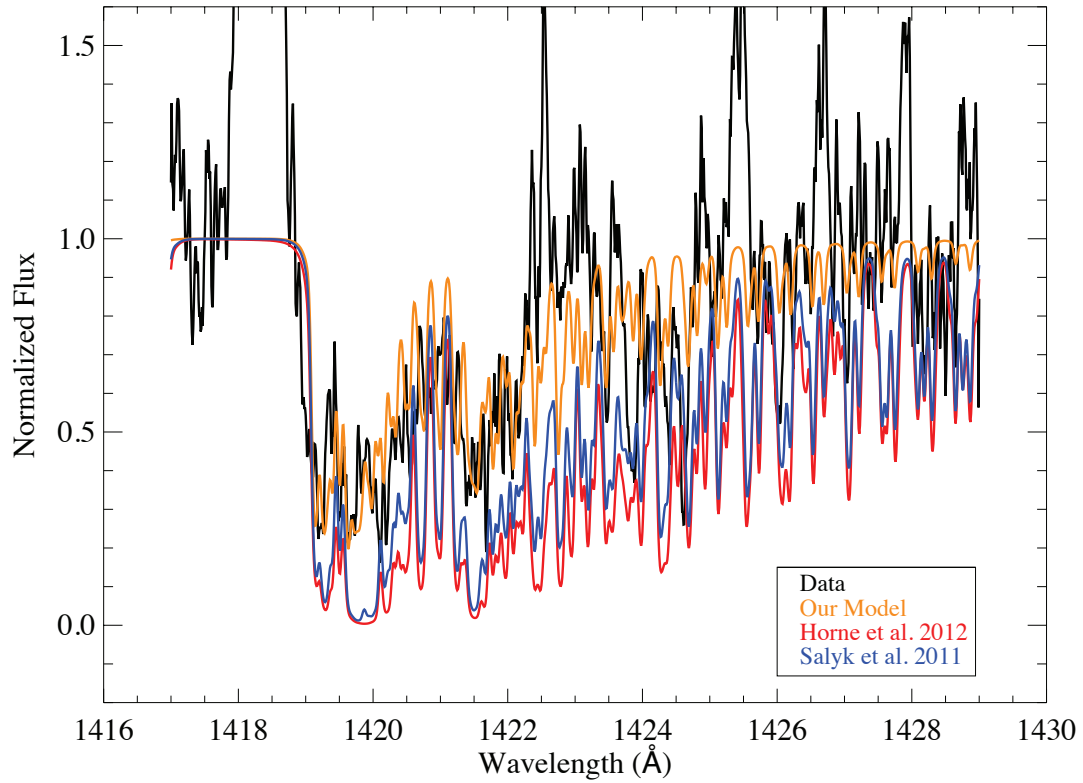
Fig. 2.6.— I use the temperature and column density values of Salyk et al. (2011a) and Horne et al. (2012) for AA Tau in my model and assume $^{12}CO/^{13}CO \sim 70$ to compare their CO gas parameters to mine. For the comparison, I use the (4 - 0) band of AA Tau. The data is in black, my fit is in orange, the Salyk et al. (2011a) model is in blue, and the Horne et al. (2012) model is in red.

Table 2.4.   Protoplanetary Disk Warm Gas Parameters

| Object | n_{CO} | CO/H$_2$[a] | ^{12}CO/^{13}CO |
	cm^{-3}		
AA Tau	$5.3^{+28.1}_{-4.5} \times 10^2$	$< 1.1 \times 10^{-4}$	$25.1^{+373.0}_{-22.6}$
DE Tau	$1.1^{+4.2}_{-0.9} \times 10^3$	$< 2.3 \times 10^{-4}$	$15.8^{+778.5}_{-14.2}$
HN Tau	$6.6^{+26.7}_{-5.8} \times 10^1$	$< 1.6 \times 10^{-5}$	$6.3^{+93.7}_{-5.0}$
RECX-15	$4.2^{+12.5}_{-3.8} \times 10^3$	$< 7.9 \times 10^{-4}$	$12.6^{+113.3}_{-11.8}$
RW Aur	$5.3^{+21.2}_{-4.6} \times 10^2$	$< 9.9 \times 10^{-5}$	$158.5^{+635.8}_{-126.9}$
SU Aur	$1.7^{+6.7}_{-1.5} \times 10^3$	$< 3.1 \times 10^{-4}$	$79.4^{+2432.5}_{-76.2}$

[a]CO/H$_2$ ratio upper limit. For CO/H$_2$ ratio less than this value, the absorption lines are thermalized up to $J = 25$.

translucent and dense cloud CO/H_2 ratios ($10^{-6} - 10^{-4}$; Lacy et al. 1994; Burgh et al. 2007) are sufficient to maintain a thermal distribution for the observed CO absorption lines in five of the targets. Although the derived CO densities for most of the targets suggest that the CO is thermalized, the sample is also consistent with sub-thermal excitation, within the uncertainties. Sub-thermally populated lines would lead to the CO temperatures being underestimated. If the absorbing CO population is in thermal equilibrium, then I conclude that the *observed* CO/H_2 ratios derived by France et al. (2011b, 2012b) are not representative of the *local* CO/H_2 ratios in the warm molecular disk surface.

I compare my derived temperatures and approximated CO densities (which I change to a molecular hydrogen density with an assumed CO/H_2 ratio of 10^{-4}) to the Woitke et al. (2011) model of RECX-15 as a check on the vertical disk structure. Continuing my assumption that collisions with H_2 are the leading contributor to the CO level populations, the averaged hydrogen density will be dominated by H_2 and we can directly compare the plots in Figure C.2 of Woitke et al. (2011) with my temperatures and densities assuming the CO radius to be $r_{CO} \approx 10$ AU as above. For each target's temperature and density pair, the height of the gas determined from the model are consistent with each other. These heights range between $z/r \sim 0.6$ to ~ 0.7 for the six targets, putting the gas in the flared upper disk atmosphere.

2.4.3. Comparison of CO with System Parameters

Using the scale height model from §2.4.2, I calculate that only inclinations of $> 79°$ will intercept the $A_V = 1$ surface of the disk, which is larger than the inclinations in Table 2.1. At the inclinations of the targets, the sightlines are not probing into the depth of the disk where the visual extinction exceeds unity, which indicates that the CO is likely well above the $A_V = 1$ disk surface. However, using a dimensionless height of $z/r = 0.6$, the disk would be intercepted for inclinations $\gtrsim 60°$. This increases the estimate on the unconstrained HN

Tau inclination. The lower limit on inclinations of $\gtrsim 60°$ is compatible with most of the disk inclinations, with the notable exception of DE Tau. The inclination of DE Tau is too small for me to be observing the gas in absorption, yet I clearly see the absorption bands in the data. DE Tau may be a candidate for a protoplanetary disk with a slow-moving molecular disk wind with a more face-on inclination and blue-shifted lines (Pontoppidan et al. 2011). DF Tau, another target in the France et al. (2012b) sample known to have CO (Najita et al. 2003; Salyk et al. 2011a; Schindhelm et al. 2012a) and thought to have a high inclination (85°; Johns-Krull & Valenti 2001), does not show UV CO absorption, which is surprising. DF Tau has an anomalously large radius for a 10^6 Myr star (3.37 $R_\odot$, Gullbring et al. 1998), which leads to the large inclination value. The spectrum for DF Tau is shown in Figure 2.7 with the fit for AA Tau overplotted to illustrate the non-detection. A revised determination of the inclination of DE Tau and DF Tau, and possibly the other sources in the sample, would be useful. With notable exceptions, for the mid- to high-inclination disks known to contain CO, I see absorption if the gas is located at a height of $z/r \gtrsim 0.6$, which is compatible with my derived temperatures and estimated densities. A cartoon of this geometry is shown in Figure 2.8.

In Figure 2.9, I compare the column density and rotational temperature of CO with the mass accretion rate and disk inclination. I do not see any strong correlations between these parameters, though there may be a slight decrease in temperature with increasing disk inclination. At higher inclinations, I am observing the disk more edge-on so that the line-of-sight passes through the colder, denser material lower in the disk atmosphere.

2.5. Conclusions

I present model fits to ultraviolet CO absorption lines in six protoplanetary systems. I find results in AA Tau and HN Tau that are consistent with previous work and extend my analysis to four new targets obtained with *HST*-COS far-UV G130M and G160M modes.

I find CO rotational temperatures in the range 300 - 700 K, which agree well with UV CO fluorescence rotational temperatures. However, my temperatures are cooler than inner disk CO temperatures obtained from the analyses of IR CO emission spectra and warmer than the Rettig et al. (2006) CO temperatures from IR CO absorption. The IR emission data may be probing a different gas population at smaller disk radii, while the IR absorption data is likely probing gas at larger radii. The measured velocities of the CO absorbing gas rule out an origin in a fast-moving disk wind. My derived temperatures and approximated densities of the gas are consistent with models for disk heights of $z/r \sim 0.6$. This CO location constrains the inclination of the disks to be $\gtrsim 60°$ in order to intercept the absorbing gas in the model.

I note that the present analysis is roughly at the limit of what is feasible with the current generation of HST instrumentation. Higher spectral resolution would improve my molecular parameter determination significantly. Unfortunately, observations at these flux levels with HST-STIS E140M mode are not feasible. A new observational capability will be required to derive more robust disk parameters from CO absorption line observations of CTTSs. However, future observations with the new COS G130M $\lambda1222$ mode should be able to directly probe warm H_2 absorption in these disks at wavelengths around 1100 Å. These observations would allow me to directly determine the value of the CO/H_2 ratio in moderate-to-high inclination protoplanetary disks.
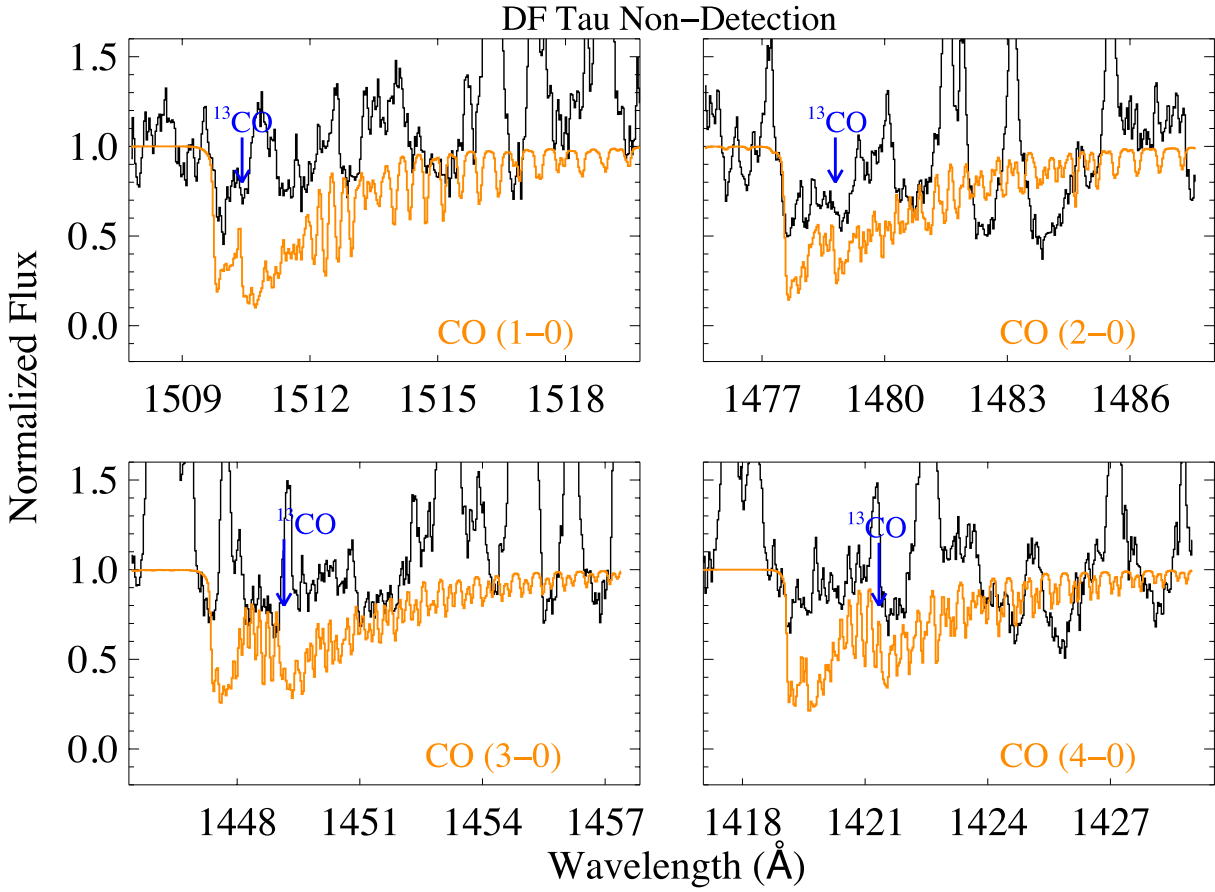
Fig. 2.7.— COS data for DF Tau with the model fit of AA Tau overplotted, showing the absence of CO absorption in the DF Tau spectrum (DF Tau data in black and best-fit model for AA Tau in orange). The ^{13}CO bandheads are marked to show the two different CO species.
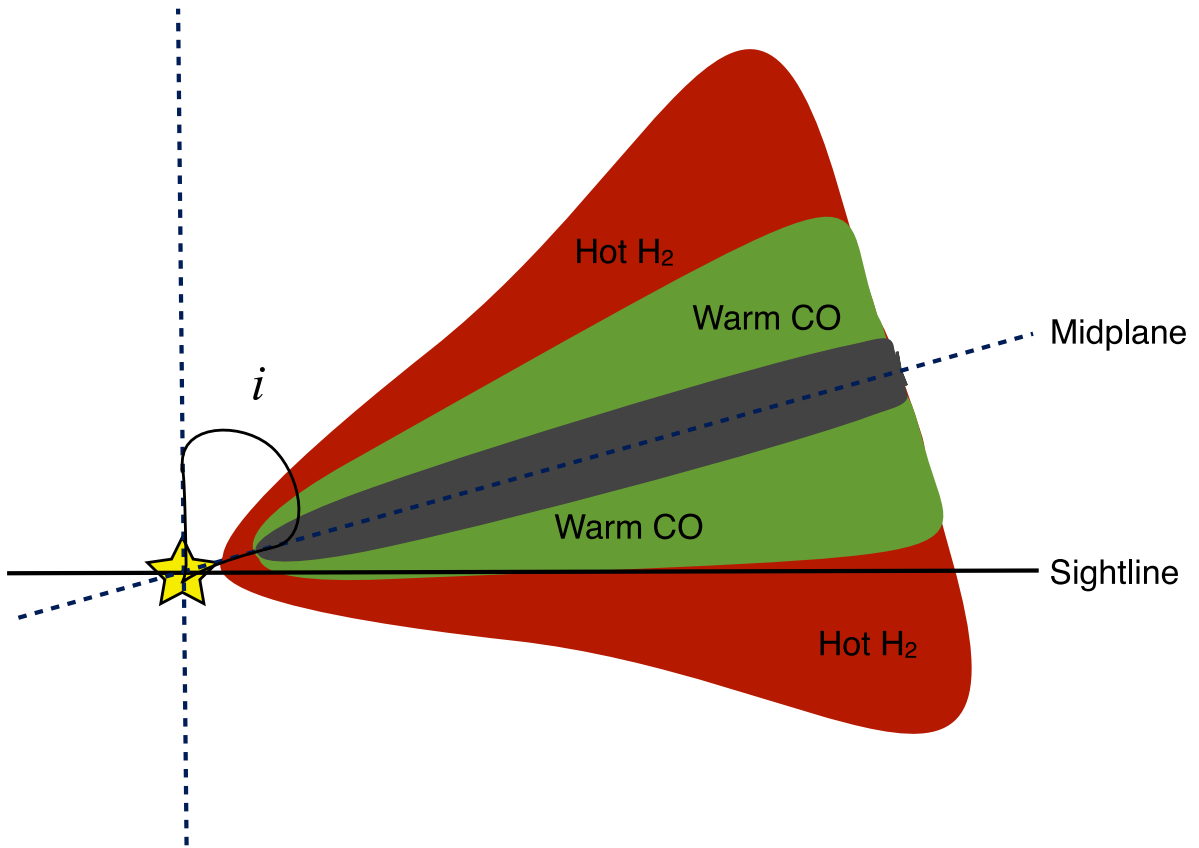
Fig. 2.8.— A schematic representation of the line-of-sight geometry for the inner region of T Tauri star disks. The red layer is observed as low-density, hot (T $\sim$ 2500 K) H_2 emission and absorption (Herczeg et al. 2004; Yang et al. 2011; France et al. 2012a); the green material is observed as intermediate density, warm (T $\sim$ 500 K) CO emission and absorption; and the dark midplane is inaccessible to UV observations.
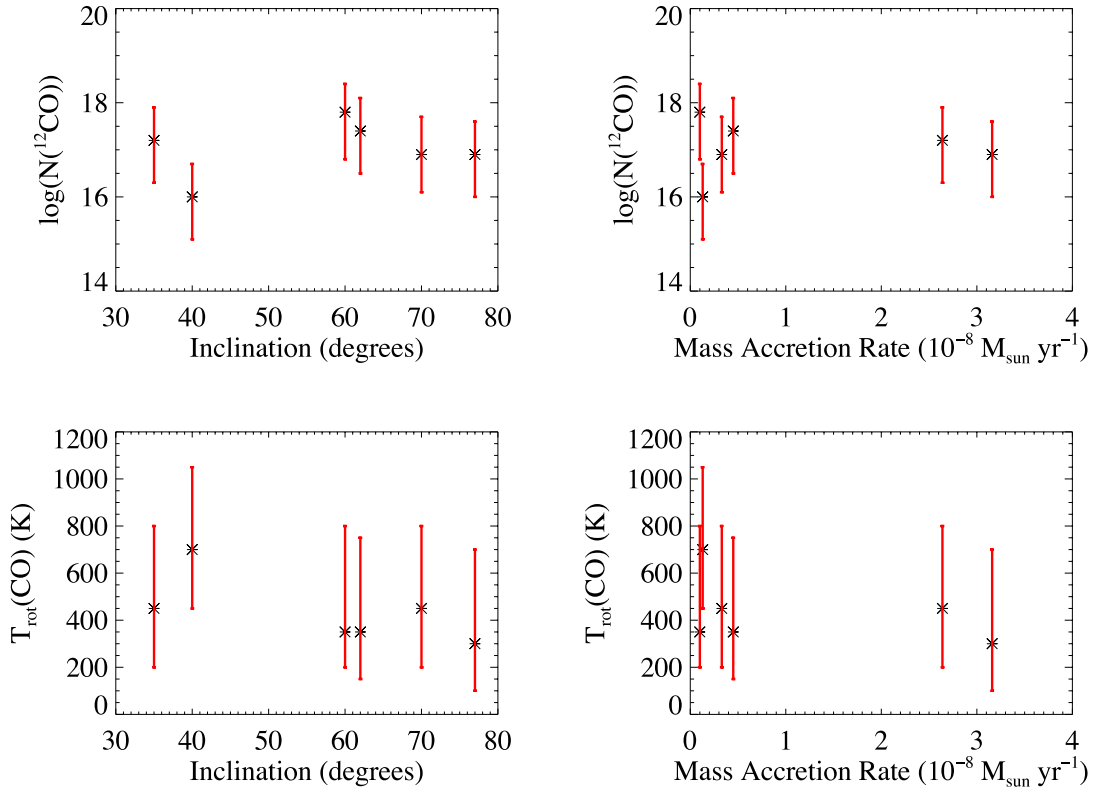
Fig. 2.9.— Correlations of the target parameters and best-fit parameters.

3.   H I Lyα Absorption

"Why ask a question whose answer would demand ten more questions?"

- David Mitchell, *Cloud Atlas*

Interstellar reddening corrections are necessary to reconstruct the intrinsic spectral energy distributions (SEDs) of accreting protostellar systems. The stellar SED determines the heating and chemical processes that can occur in circumstellar disks. Measurement of neutral hydrogen absorption against broad Lyα emission profiles in young stars can be used to obtain the total H I column density (N(H I)) along the line of sight. We measure N(H I) with new and archival ultraviolet observations from the *Hubble Space Telescope* (*HST*) of 31 classical T Tauri and Herbig Ae/Be stars. The H I column densities range from $\log_{10}$(N(H I)) $\approx 19.6 - 21.1$, with corresponding visual extinctions of $A_V = 0.02 - 0.72$ mag, assuming an R_V of 3.1. We find that the majority of the H I absorption along the line of sight likely comes from interstellar rather than circumstellar material. Extinctions derived from new *HST* blue-optical spectral analyses, previous IR and optical measurements, and new X-ray column densities on average overestimate the interstellar extinction toward young stars compared to the N(H I) values by ~ 0.6 mag. We discuss possible explanations for this discrepancy in the context of a protoplanetary disk geometry.

3.1.   Introduction

Extinction correction of an observed short wavelength spectral energy distribution (SED) allows determination of the level of irradiance in the planet-forming environment of the protoplanetary disk (e.g. Aresu et al. 2012). Ultraviolet (UV) radiation plays a particularly important role in gas heating (e.g. Jonkheid et al. 2004; Nomura et al. 2007; Woitke et al.

2009) and protoplanetary disk gas chemistry (e.g. Aikawa & Herbst 1999; Bethell & Bergin 2009; Fogel et al. 2011; Bruderer 2013). Neutral hydrogen (H I) Lyα in emission is a significant component of the far-UV radiation (Bergin et al. 2003; Herczeg et al. 2004; Schindhelm et al. 2012b) produced in the stellar atmosphere and accretion funnel flow (see, e.g., Hartmann et al. 1994; Muzerolle et al. 1998; Kurosawa et al. 2006; Bouvier et al. 2007c; Ingleby et al. 2011).

Line of sight extinction values are typically estimated for young stars from measured color excess relative to an assumed intrinsic color corresponding to the spectral type. However, due to veiling of the photosphere in Classical T Tauri Stars (CTTSs) by excess accretion emission (e.g. Gullbring et al. 1998), the extinction-free color determination becomes challenging without an accurate measurement of the excess flux due to accretion shocks (Hartigan et al. 1995). For this reason, more sophisticated extinction estimates come from modeling of spectrophotometry, including contributions not only from the underlying stellar photosphere but also from a veiling continuum (e.g. Hartigan & Kenyon 2003; Herczeg & Hillenbrand 2014).

Optical extinction measurements, which are often calculated using assumed colors for a particular spectral type (see Section 3.3), can vary due to uncertainties in the spectral type for the target star. Scatter in intrinsic spectral color and effective temperature at a given spectral type (∼ ±2000 K at A0; Gerbaldi et al. 1999) and rapid rotation which leads to large temperature gradients on the star (Müller et al. 2011) can also contribute to a broad range of optical extinction. A further complication in deriving extinction from colors or spectrophotometry is that the optical variability of CTTSs can also be substantial (∼ 0.1 − 2.5 mag in the V band; Herbst et al. 1994), which includes large color variability in many cases, and thus further uncertainty in the extinction estimates if non-simultaneous data is used. The intrinsic color of a star may be inaccurately determined if the star is in a close binary system; however, this is not applicable to most of the targets (except possibly the spectroscopic binaries V4046 Sgr, TWA 3A, AK Sco, and HD 104237). The X-ray and

Lyα H I column densities of these binaries should also not be strongly affected.

Because of the range in techniques employed and wavelengths used, as well as the astrophysical uncertainties due to variability, A_V measurements for the same star can range dramatically in the literature. The reported visual extinction of HD 135344B spans the range 0.30 (Garcia Lopez et al. 2006) to 0.96 (Alecian et al. 2013), and the visual extinction of RW Aur A has been cited from 0.50 (White & Ghez 2001) to 1.58 (White & Hillenbrand 2004). Even small changes in the adopted extinction create large changes in estimates for the UV luminosity. At an A_V value of 2 mag, the normalized flux correction at Lyα (1216 Å) is $\sim$ 600, while at $A_V = 0.5$ mag, the correction is only ~ 5 (see Figure 3.1). The uncertainty in the stellar UV radiation field due to extinction uncertainty has a significant effect on chemical models of disks.

The H I column density is well correlated with interstellar reddening caused by dust grains through the well-known Bohlin et al. (1978) relation ($\langle N(H\,I)/E(B-V)\rangle = 4.8 \times 10^{21}$ atoms cm^{-2} mag^{-1}). This relation was derived from a correlation (typical scatter $\sim 50\%$ about the fit line for stars with accurate $E(B-V)$) of the interstellar H I column densities and color excess ($E(B-V)$) values of 100 stars surveyed with the *Copernicus* satellite. The interstellar H I columns were calculated by fitting the absorption from interstellar gas against the continuum emission of the stars. Diplas & Savage (1994b) found a similar correlation between H I and $E(B-V)$ ($\langle N(H\,I)/E(B-V)\rangle = 4.93 \times 10^{21}$ atoms cm^{-2} mag^{-1}) with 6% uncertainty using archival Lyα absorption line data of 393 stars from IUE.

In this chapter, I present new measurements of the H I column density along the line of sight toward accreting young stars (spectral types roughly A0 to M4) using a UV-based technique. I employ a least-squares fitting routine to simultaneously parameterize the stellar plus accretion Lyα emission profile and the line of sight absorption of H I. Walter et al. (2003), Herczeg et al. (2004), and Lamzin (2006) performed similar fitting routines to a smaller subset of CTTSs. I fit the emission profile with a broad and narrow Gaussian component and employ a Voigt profile to characterize the H I absorption. Adopting the well-characterized
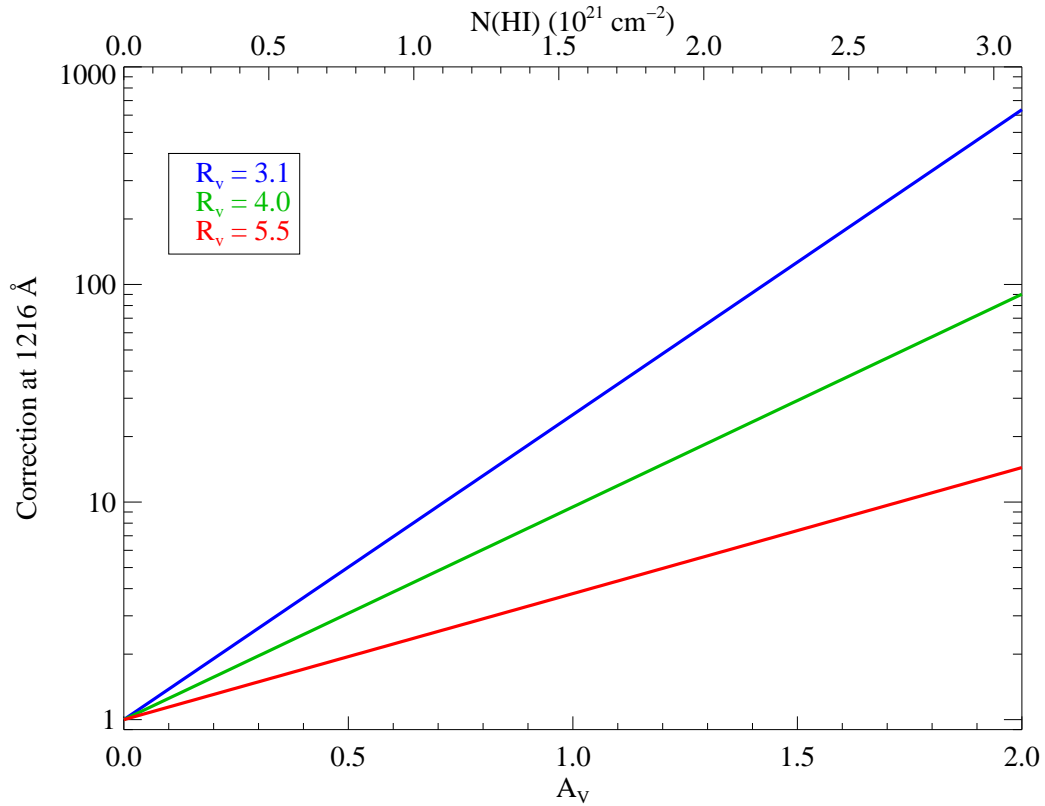
Fig. 3.1.— Correction to the normalized unreddened flux at 1216 Å as a result of changing visual extinction, A_V, using the reddening curve of Cardelli et al. (1989) including the near-UV update of O'Donnell (1994). A_V values are converted to N(H I) values along the top of the figure using the Bohlin et al. (1978) relation assuming $R_V = 3.1$. As the visual extinction increases from 0 to 2, the unreddened flux changes by up to factors of 600.

relationship between the total hydrogen column and $E(B - V)$ (Bohlin et al. 1978), modulo assumptions about the grain distribution (R_V), I can make a straightforward determination of the reddening that is not confused by veiling or interpretation of (spectro)photometric variability.

I describe the targets and observations in §3.2. The analysis of the observations (including new optical and X-ray measurements) and a description of the Lyα model fitting procedure is presented in §3.3. The results of the fits and comparisons to results using different techniques in other wavelengths are described in §3.4. I provide a discussion and offer possible explanations for the discrepancy in extinction values derived in this chapter compared to those measured in the optical, IR, and X-ray in §3.5. Finally, §3.6 contains a summary of my results.

3.2. Targets and Observations

I analyze Lyα spectra of 31 young stars listed in Table 3.1. Many of these observations have been described previously in the molecular hydrogen (H_2) and hot gas surveys of France et al. (2012b) and Ardila et al. (2013), respectively. Several targets are binaries or multiples (DF Tau: Ghez et al. 1993, DK Tau, HN Tau, RW Aur, and UX Tau: all Correia et al. 2006), but only the primary is observed within the aperture. TWA 3A, AK Sco, and HD 104237 are spectroscopic binaries (Muzerolle et al. 2000; Gómez de Castro 2009; Böhm et al. 2004). V4046 Sgr is a known short-period binary system (Quast et al. 2000) which nevertheless acts as a point source for the interstellar absorption. The stars are young; ranging in age from Myr old members of star forming regions (Taurus-Auriga, Chamaeleon I, and η Chamaeleontis) to $10 - 30$ Myr field pre-main sequence stars (e.g. TW Hya, AK Sco) with most targets being in the range of 1 - 10 Myr, comparable to the timescale of depletion for accreting gas and circumstellar dust (Hernández et al. 2007; Fedele et al. 2010) and therefore presumably giant planet formation (Hubickyj et al. 2005). The majority of the targets are located in the

Taurus-Auriga, Chamaeleon I, and η Chamaeleontis star forming regions. The remaining targets belong to other associations and isolated systems. The distances to all the targets are listed in Table 3.1. The sample data was obtained with the *Hubble Space Telescope* Cosmic Origins Spectrograph (*HST*-COS) and Space Telescope Imaging Spectrograph (STIS).

3.2.1. COS Observations

Observations from the DAO of Tau guest observing program (PID 11616; PI - G. Herczeg) comprise the majority of the data. Additional COS observations include those from the COS Guaranteed Time Observing program (PIDs 11533 and 12036; PI - J. Green) and observations of HD 135344B. Most of the CTTS spectra were obtained using the far-UV medium-resolution modes of COS (G130M and G160M (Δv $\approx$ 18 km s^{-1} at Lyα); Green et al. 2012). Multiple central wavelengths and several focal-plane positions covered the wavelength region from $\approx 1150 - 1750$ Å while minimizing fixed pattern noise. The far-UV COS data were processed using the COS calibration pipeline, CALCOS, and aligned and co-added with the procedure described in Danforth et al. (2010). COS, a slitless spectrograph, experiences strong contamination from geocoronal Lyα filling the large (2.5" diameter) aperture. I mask the central region of the Lyα spectra due to geocoronal H I contamination.

3.2.2. STIS Observations

Targets exceeding the COS bright-object limit (AK Sco, CV Cha, and HD 104237) had to be observed with the E140M medium-resolution mode of STIS (Δv $\approx$ 7 km s^{-1} between 1150 and 1700Å; Kimble et al. 1998; Woodgate et al. 1998). The observations were taken through the 0.2" $\times$ 0.2" slit for two to three orbits per object. Archival STIS observations of RU Lupi, TW Hya, and the Herbig Ae/Be stars HD 100546, AB Aur, and HD 163296 along with observations of HD 104237 and TWA 3A with the G140M mode of STIS (Δv $\approx$ 30 km s^{-1} between 1150 and 1700Å) complete the UV sample. The STIS echelle calibration

Table 3.1.   Target Parameters

Object	Spectral Type	Distance (pc)	L_* ($L_\odot$)	M_* ($M_\odot$)	$\dot{M}$ (10^{-8} $M_\odot$ yr^{-1})	Ref.[a]
AA Tau	K7	140	0.71	0.80	0.33	2,4,7,12,16,58,59
AB Aur	A0	140	46.8	2.4	1.8	19,49,50,58,59
AK Sco	F5	103	7.59	1.35	0.09	18,20,34,62
BP Tau	K7	140	0.925	0.73	2.88	7,12,38,58,59
CS Cha	K6	160	1.32	1.05	1.20	21,35,60
CV Cha	G8	160	7.7	2.00	3.16	22,36,60
DE Tau	M0	140	0.87	0.59	2.64	7,10,12,58,59
DF Tau A	M2	140	1.97	0.19	17.7	7,10,58,59
DK Tau A	K7	140	1.45	0.71	3.79	7,10,12,58,59
DM Tau	M1.5	140	0.24	0.50	0.29	16,29,32,58,59
DN Tau	M0	140	0.87	0.60	0.35	7,16,32,39,58,59
DR Tau	K7	140	1.09	0.80	3.16	2,8,16,58,59
GM Aur	K5.5	140	0.74	1.20	0.96	7,16,32,58,59
HD 100546	B9.5	103	32.4	2.4	0.1	19,52,53,65
HD 104237	A7.5	116	34.7	2.50	3.50	19,23,31,45
HD 135344B	F3	140	8.13	1.60	0.54	19,31,42,64
HD 163296	A1	122	24.0	2.0	6.9	18,19,50,51
HN Tau A	K5	140	0.19	0.85	0.13	6,7,12,58,59
IP Tau	M0	140	0.41	0.68	0.08	7,12,58,59
LkCa 15	K3	140	0.72	0.85	0.13	12,29,32,58,59
RECX-11	K4	97	0.59	0.80	0.03	13,24,47,61
RECX-15	M2	97	0.08	0.40	0.10	13,14,15,61
RU Lup	K7	121	0.42	0.80	3.00	25,30,41,62
RW Aur A	K4	140	2.3	1.40	3.16	5,9,11,12,17,58,59
SU Aur	G1	140	9.6	2.30	0.45	1,3,8,11,12,58,59
SZ 102	K0	200	0.01	0.75	0.08	26,37,43,48
TWA 3A	M4Ve	34	0.09	0.15	0.005	54,55,56,57,63
TW Hya	K6	54	0.17	0.60	0.02	27,30,42,62
UX Tau A	K2	140	3.5	1.30	1.00	12,32,58,59
V4046 Sgr	K5	83	0.5+0.3	0.86+0.69	1.30	28,33,44
V836 Tau	K7	140	0.32	0.75	0.01	12,30,46,58,59

[a] (1) Akeson et al. (2002); (2) Andrews & Williams (2007b); (3) Bertout et al. (1988); (4) Bouvier et al. (1999); (5) Eisner et al. (2007); (6) France et al. (2011a); (7) Gullbring et al. (1998); (8) Gullbring et al. (2000); (9) Hartigan et al. (1995); (10) Johns-Krull & Valenti (2001); (11) Johns-Krull et al. (2000); (12) Kraus & Hillenbrand (2009); (13) Lawson et al. (2004); (14) Luhman & Steeghs (2004); (15) Ramsay Howat & Greaves (2007); (16) Ricci et al. (2010); (17) White & Ghez (2001); (18) van den Ancker et al. (1998); (19) van Boekel et al. (2005); (20) Alencar et al. (2003); (21) Lawson et al. (1996); (22) Siess et al. (2000); (23) Feigelson et al. (2003); (24) Lawson et al. (2001); (25) Herczeg et al. (2005); (26) Comerón & Fernández (2010); (27) Webb et al. (1999); (28) Quast et al. (2000); (29) Hartmann et al. (1998); (30) Herczeg & Hillenbrand (2008); (31) Garcia Lopez et al. (2006); (32) Andrews et al. (2011); (33) France et al. (2011b); (34) Gómez de Castro (2009); (35) Espaillat et al. (2007); (36) Hussain et al. (2009); (37) Comerón et al. (2003); (38) Simon et al. (2000); (39) Muzerolle et al. (2003); (40) Espaillat et al. (2010); (41) Stempels et al. (2007); (42) Pontoppidan et al. (2008); (43) Coffey et al. (2004); (44) Rodriguez et al. (2010); (45) Grady et al. (2004); (46) Najita et al. (2008); (47) Ingleby et al. (2011); (48) Hughes et al. (1994); (49) Hashimoto et al. (2011); (50) Donehew & Brittain (2011); (51) Isella et al. (2007); (52) Ardila et al. (2007); (53) Grady et al. (2005); (54) Torres et al. (2008); (55) de la Reza & Pinzón (2004); (56) da Silva et al. (2009); (57) Muzerolle et al. (2000); (58) Bertout et al. (1999); (59) Loinard et al. (2007); (60) Luhman (2004); (61) Mamajek et al. (1999); (62) van Leeuwen (2007); (63) Mamajek (2005); (64) Grady et al. (2009); (65) van den Ancker et al. (1997).

software developed for the StarCAT catalog (Ayres 2010, T. Ayres 2011, private communication) combined the far-UV STIS spectra. Additionally, I use STIS G430L (Δv $\approx$ 600 km s^{-1} between 3050 and 5550Å) blue optical spectra of CV Cha, HD 104237, RU Lupi, SU Aur, and AK Sco (PID 11616; PI - G. Herczeg) to calculate optical measurements of the visual extinction. The geocoronal signal is weaker in the STIS data due to the narrower slit; however, I remove the inner region (typically 0.5 - 2 Å) in all the spectra for consistency.

3.3. N(H I) Analysis

3.3.1. Overview of Lyα Profiles

Lyα emission is the result of the electron in an H I atom transitioning from the $2p$ to the $1s$ state. The radiative lifetime of the $2p$ level is $\sim 2 \times 10^{-9}$ s (Wiese & Fuhr 2009), such that at interstellar densities the collisional depopulation of the state is negligible. At large optical depths, the emitted Lyα photons will be reabsorbed and reemitted in different directions several times by other H I atoms in the vicinity. Due to the velocity of the H I atoms, the scattered Lyα photons undergo a frequency shift (frequency scattering), which tends to move the photons away from the Lyα line center and create a Lyα profile with broad wings. High infall velocities of H I in the accretion flow are able to significantly broaden the Lyα profile (up to several hundred or even a thousand km s^{-1}). Due to both spatial and spectral diffusion, the photons eventually escape the Lyα emitting region, and can then be absorbed by H I along the line of sight of the observations.

The most salient features of the Lyαprofiles in young stars are their spectrally broad emission lines, typically extending out to several hundred km s^{-1} on both the blue and red sides, and their strong central absorption. The breadth of the emission line points to an accretion origin, such that this emission is likely produced close to the star (see §3.5.1). Both the red side emission and blue side emission have contributions from accreting material. The blue side emission is affected by outflowing material, while the central absorption is domi-

nated by the damped interstellar component, though some contribution from self-absorption in the accretion or wind flow may also be present. I ignore the effect of self-absorption in this analysis and do not expect the results or interpretations to be strongly influenced.

3.3.2. Lyα Profile Fitting

I fit the Lyα spectra with a three component, nine parameter model consisting of broad and narrow Gaussian stellar emission lines and a Voigt H I absorption profile to determine the best-fit interstellar H I column density. The models of the broad and narrow emission lines are each characterized by a heliocentric velocity, an amplitude, and a full-width half-maximum (FWHM) value, while the H I absorption profile is characterized by a Doppler b-value, a heliocentric velocity, and a column density. The broad and narrow components of the Lyα emission profile are pictured in Figure 3.2 for RECX-15 to illustrate the model Lyα profile decomposition. Fits showing the full Lyα model profiles for 3 select targets are shown in Figure 3.3. These are not fully reconstructed profiles based on molecular fluorescence line fluxes such as those in Herczeg et al. (2004) and Schindhelm et al. (2012a,b), and are shown only to illustrate the full fitting procedure. Because many of the targets have outflows that absorb the blueward side of the Lyα emission line (Schindhelm et al. 2012b), I restrict the fits to the redward side in order to derive an accurate determination of the interstellar H I column density. There is typically greater optical depth on the blueward side of the line, but without an outflow component in the model, I do not attempt to reproduce the full emission line. I only fit a small region around the emission line such that a continuum parameter was not necessary in the model. Adding a continuum model parameter to selected targets after the initial grid search gave no change to the best-fit column density. The restricted fitting region also allowed me to fit targets with an additional, very broad ($\Delta \mathrm{v} \gtrsim \pm 1500$ km s^{-1}) Lyα emission component as I could isolate the narrower Lyα emissions and mask out the broad features when performing the fit. These very broad profiles can be seen in BP Tau and GM Aur most prominently.
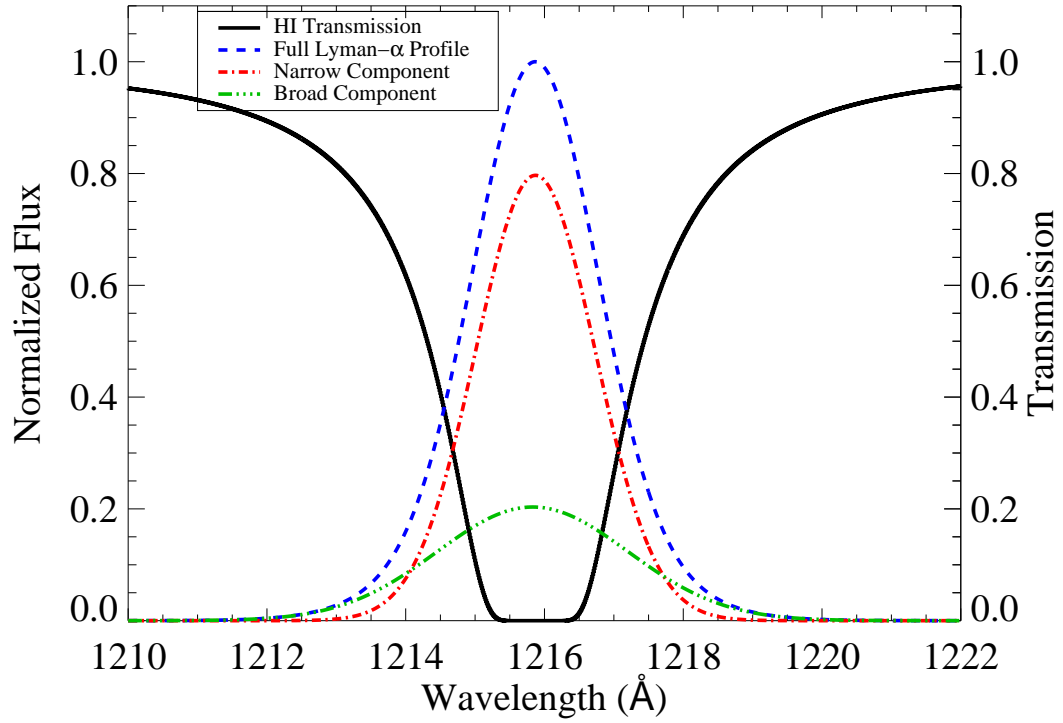
Fig. 3.2.— Components of the normalized Lyα model for RECX-15. The broad component of the Lyα emission line is the green triple-dot-dashed line, the narrow component is the red dot-dashed line, and the unabsorbed model Lyα emission (equal to the broad component added to the narrow component) is marked by the blue dashed line. The H I transmission curve is overplotted in a solid black line.
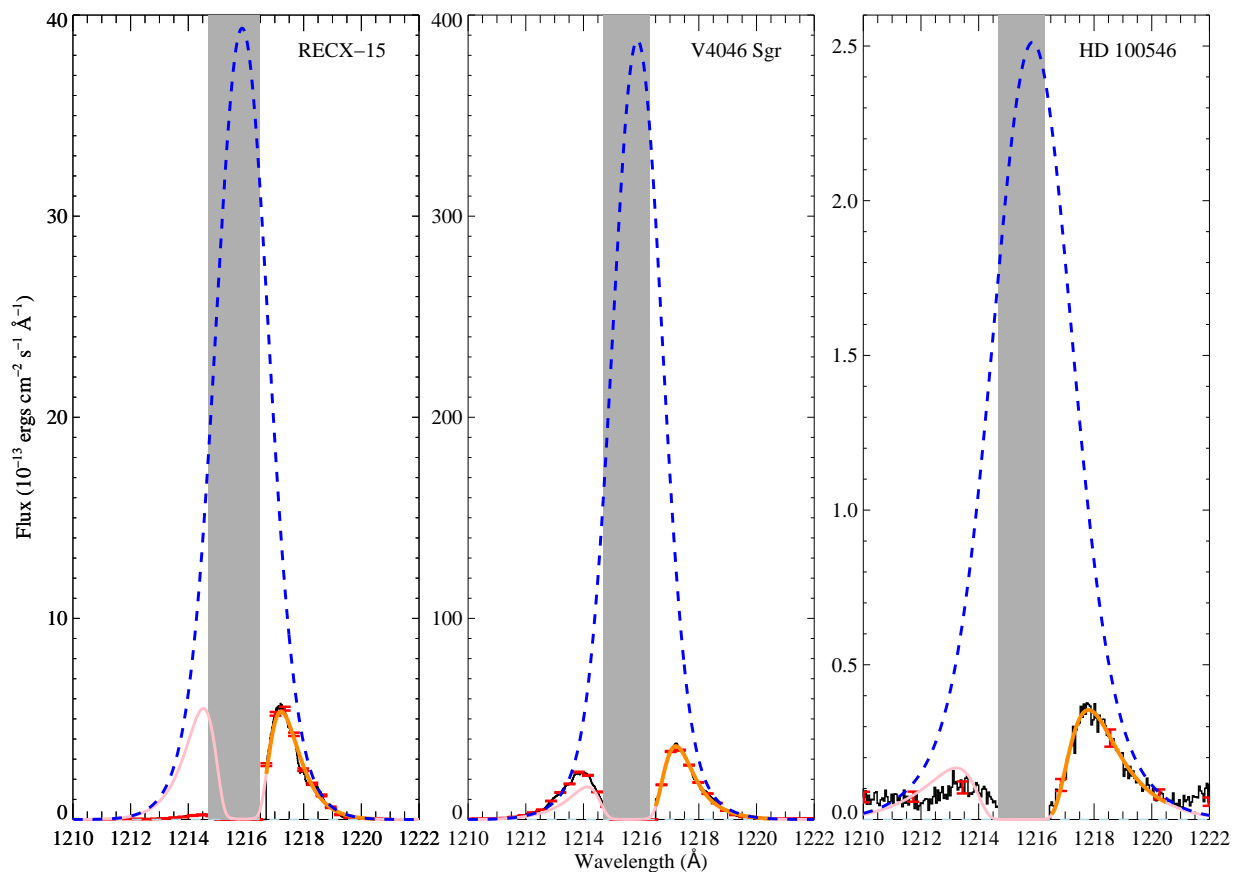
Fig. 3.3.— Model fits of the Lyα emission line in three representative targets (two CTTSs, one with and one without blueward emission, and a Herbig star). The data (with the geocoronal Lyα emission masked out in the shaded region) is in black, with the absorbed profile (Lyα emission plus H I absorption) in pink. Only the redward side of the emission line is used in the least-squares fit due to stellar outflows affecting the blueward side, and this fit is highlighted in orange. Selected error bars are shown in red. The unabsorbed model Lyα emission is marked by the blue dashed line.

I began with a preliminary fit by eye (which assumed an H I velocity shift of 0 km s^{-1}) to determine initial parameter ranges and then performed a grid search, varying the parameters in order to find the best-fit model to the data. Starting with a close fit to the data allowed me to use a higher resolution grid search and reduce the computational time needed to find the best fit.

I varied the model parameters in the grid search in order to find the best-fit values through a least-squares method similar to the procedure described in McJunkin et al. (2013). To decrease the computation time, the velocity shift of the broad and narrow emission line were set to a constant for all the targets (39 km s^{-1} and 49 km s^{-1} for the broad and narrow emission, respectively) based off the initial fit of V4046 Sgr (a high signal-to-noise prototypical example) to keep the fits consistent. For the majority of the targets, the instrumental resolution was Δv $\approx$ 18 km s^{-1}, so these offsets are only $\approx 2 - 2.5$ times the resolution element, and are mostly negligible compared to the breadth of both the Lyα emission and damped H I absorption. Assuming that neutral deuterium (D I) traces H I in the interstellar medium (ISM), I took the average of the D I Doppler b-value from Redfield & Linsky (2004) ($\sim$ 7.5 km s^{-1}), and corrected for the D/H mass difference to give an H I ISM Doppler width of $\sim$ 10 km s^{-1}, and adopted this throughout. The choice of b-value does not significantly affect the derived column densities at low b-values. At the high H I column densities of the initial model fits, we are well into the damping wing ("square root") portion of the curve of growth, which has little dependence on Doppler b-value as long as $b \lesssim 100$ km s^{-1}. I thus used three fixed parameters and six free parameters in my full Lyα absorption model.

Centered on the initial fit, I took eleven grid points in steps of 40 km s^{-1} for both the broad and narrow emission FWHM, seven grid points in steps which were 30% of the size of the initial fit values for the broad and narrow emission amplitudes, and eleven grid points in steps of 0.025 dex for the H I absorption column density. For the H I absorption velocity shift, I chose thirteen grid points ranging from -70 km s^{-1} to 50 km s^{-1} in steps of 10 km

s^{-1}. This absorption velocity grid was chosen based on the observed range of stellar radial velocities, from ~ -7 km s^{-1} (V4046 Sgr; Malaroda et al. 2006) to $+20$ km s^{-1} (DR Tau; Alencar & Basri 2000), and the velocity of D I in the ISM, which ranges from -43 to $+33$ km s^{-1} for the local ($d < 100$ pc) Milky Way (Redfield & Linsky 2004).

Due to the presence of protostellar outflows, the velocity of the absorbing gas is difficult to determine. Changing the velocity shift of the H I absorber relative to the emission lines affects the best-fit column density obtained from the model. Thus, I performed two other grid searches to test the N(H I) dependence on H I velocity in the model: one where I allowed the H I velocity to float around a velocity chosen from a new initial fit by eye (which did not assume an H I velocity shift of 0 km s^{-1}), and one with a constant H I velocity of 0 km s^{-1} (which was typically close to the center of the absorption profile). The floating velocity search had seven grid points in steps of 10 km s^{-1} centered on the H I velocity shift of the new initial fit to better estimate possible systematic errors in the column density due to the uncertainty in the H I absorber velocity. This grid search had the same grids as the first search in all other parameters. Many of the model fits from this floating H I velocity grid search had large H I velocities which systematically shifted the absorption center to longer wavelengths, requiring smaller column densities derived from the redward side of the Lyα line to fit the data, which I take into account in my error budget. The constant zero velocity search, however, had little effect on the best-fit column density from my first grid search. The targets with negative H I absorption velocities in the initial fit decreased their H I column density (if they changed at all) in the zero velocity fit because of the shift to longer wavelengths similar to the floating velocity search. The targets with positive H I absorption velocities in the initial fit tended to increase their H I column density. The majority of the H I column densities, however, did not change, and those that did only changed by $\pm 0.1 - 0.3$ dex. This is because many of the best-fit H I velocities from the first search were already close to zero, so that the velocity shift was minimal.

A montage of the model fits from my first grid search with constrained velocities for all

of the targets can be seen in Figures 3.4a - 3.4d. The best-fit H I column densities (from the first search) with errors are listed in Table 3.2. The best-fit values of additional parameters that were allowed to vary in the grid search are listed in Table 3.3. To estimate the errors, I set the model parameters to their best-fit values and varied the column density in steps of 0.025 dex. Following the χ^2 probability distribution for 1 degree of freedom, $\Delta\chi^2 = 1$ defines a 68% probability region. I increased the minimum χ^2 of the best-fit model by unity to obtain an estimate of the column density parameter range. The initial errors were defined as the width of this range. To account for the change in velocity systematically shifting the column densities lower (see above), I added the column density difference between the constrained and floating velocity grid searches in quadrature to the lower error bars on the column densities.
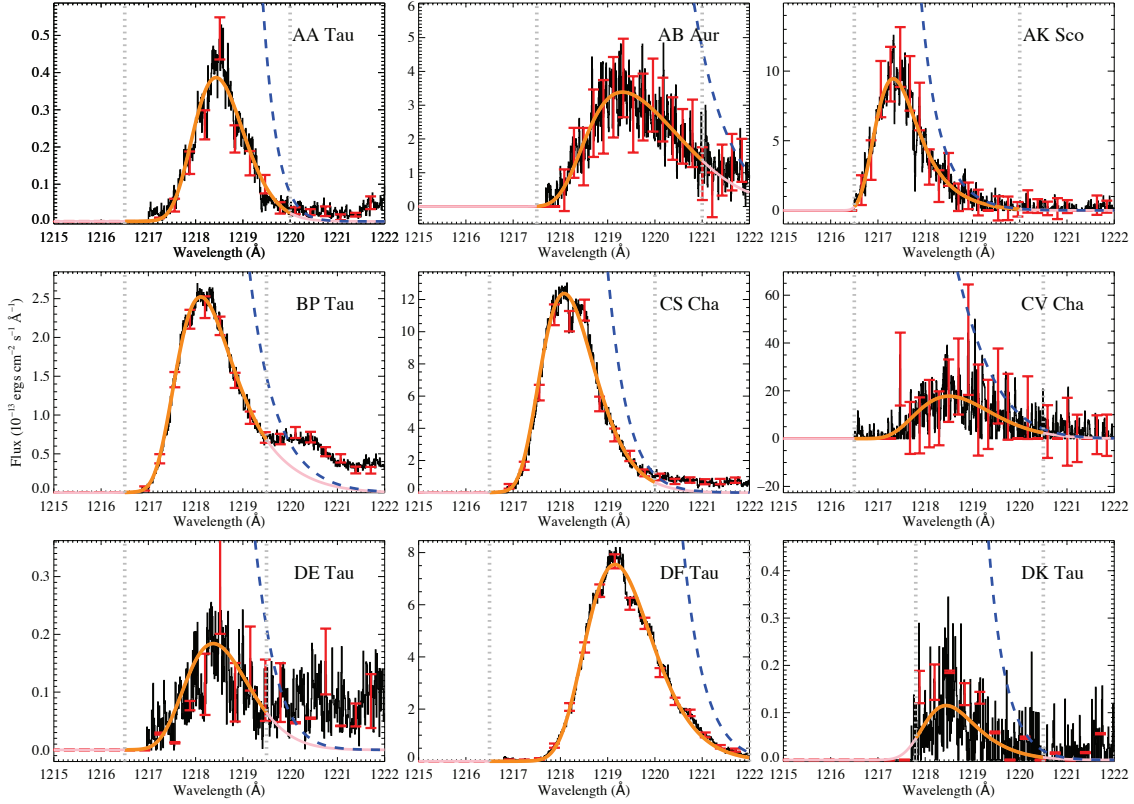
Fig. 3.4a.— Model fits of the red side of the Lyα emission line. The data, with geocoronal Lyα emission masked (zero flux is assumed in the region) is in black, with the fit in orange. Selected error bars are shown in red and the wavelength region that is fit for each target is marked by horizontal dashed lines. The unabsorbed model Lyα emission is marked by the blue dashed line. Some targets have less reliable fits due to noise in the data and some fits may have failed to find a detectable redward Lyα emission line. These targets (CV Cha, DE Tau, DK Tau, DM Tau, DN Tau, HN Tau, IP Tau, UX Tau, and V836 Tau) are identified with pink points in Figure 3.6.
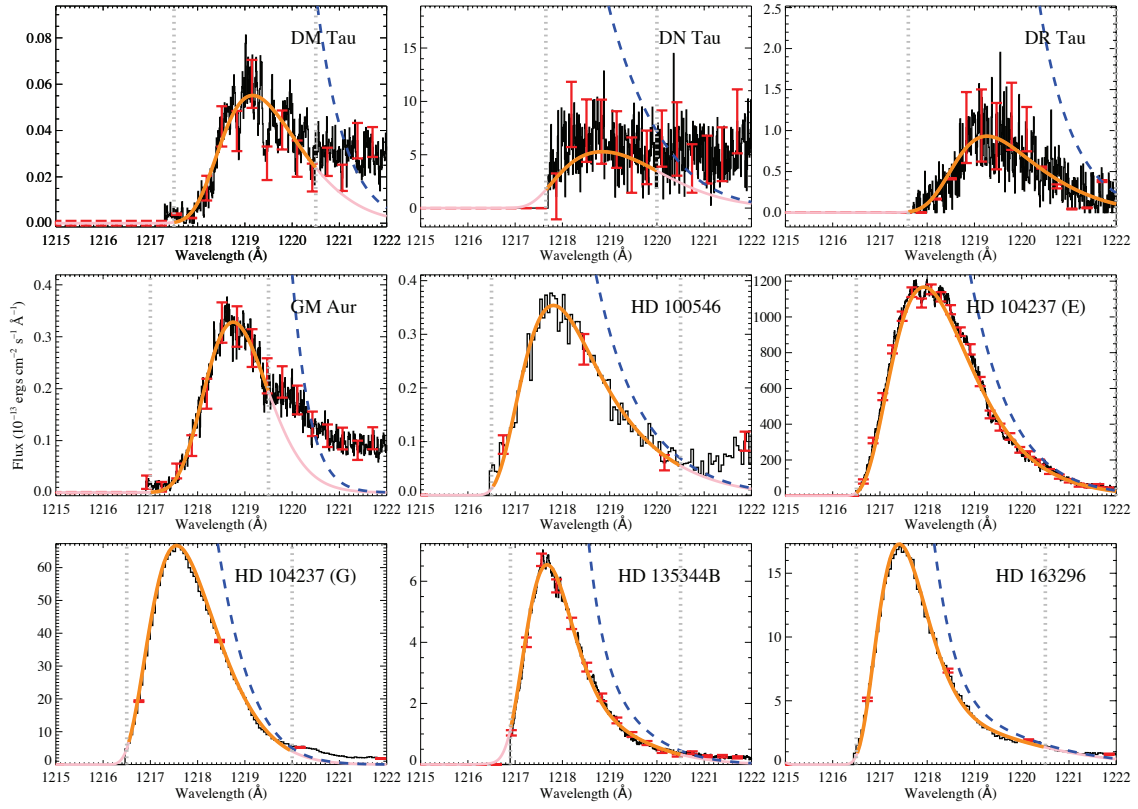
Fig. 3.4b.— Same as 4a.
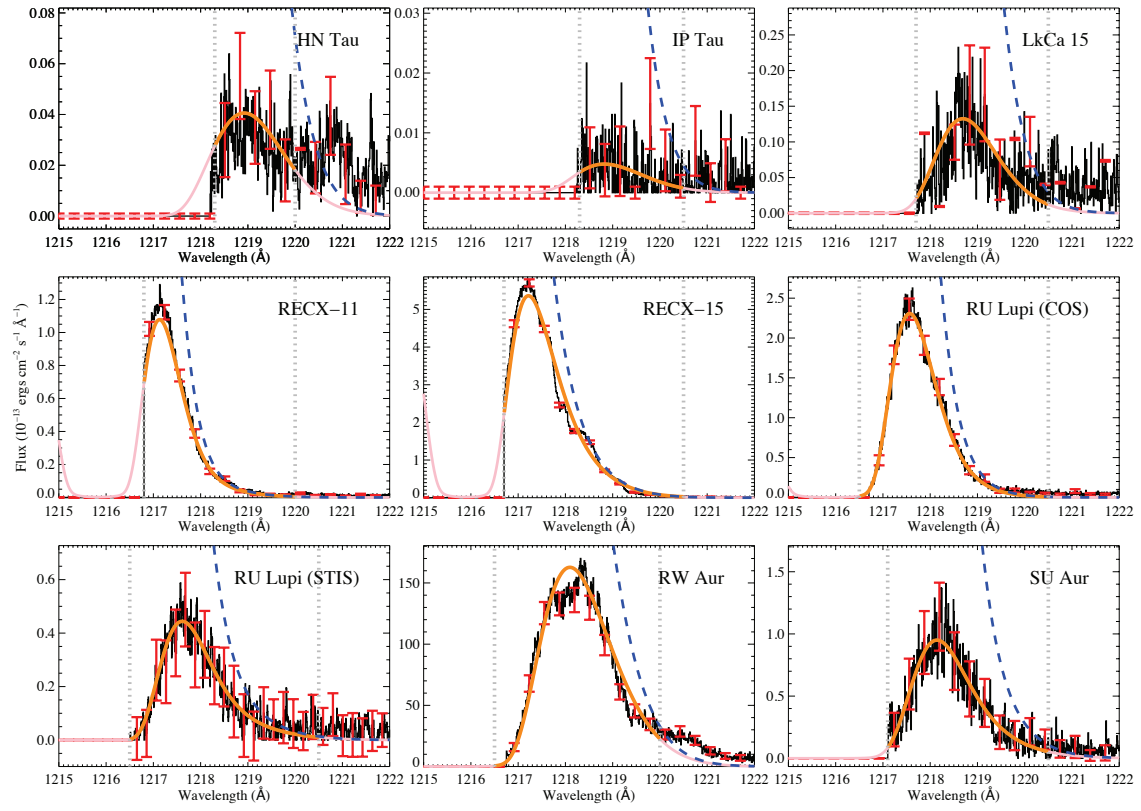
Fig. 3.4c.— Same as 4a.
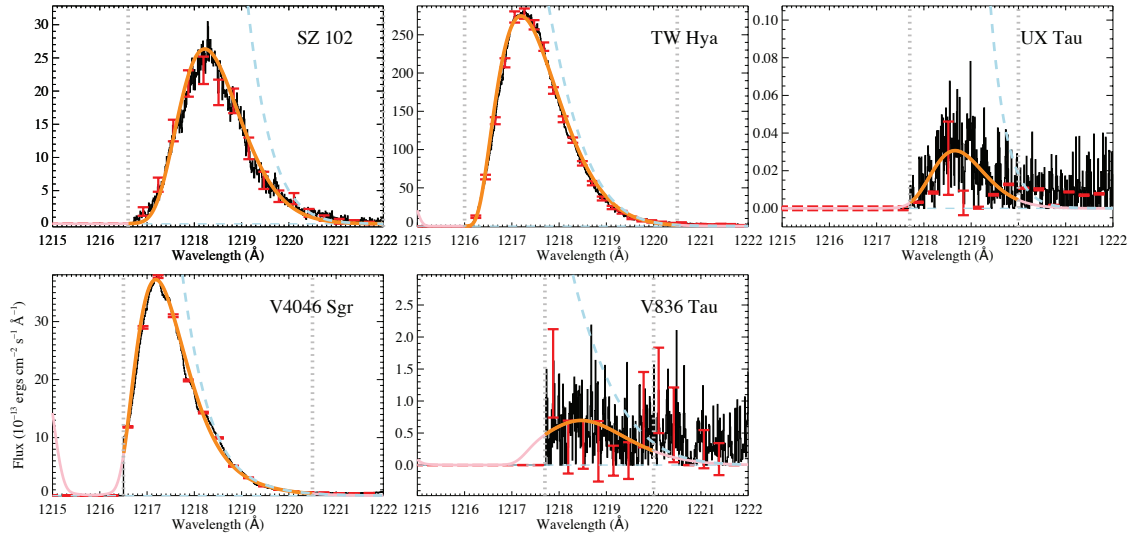
Fig. 3.4d.— Same as 4a.

Table 3.2.   Extinction Values

Target	HST PID[a]	PI	A_V(lit)	A_V(lit) Ref.[b,c]	$\log_{10}(N(H\ I))$	$A_V(3.1)$[d]	$A_V(4.0)$[d]	$A_V(5.5)$[d]
AA Tau	11616	G. Herczeg	0.49	1	$20.73^{+0.03}_{-0.13}$	0.34	0.44	0.61
AB Aur	$8065-S$	B. Woodgate	0.5	2	$20.90^{+0.05}_{-0.11}$	0.51	0.66	0.91
AK Sco	$11616-S$	G. Herczeg	0.5	3	$20.10^{+0.08}_{-0.35}$	0.08	0.10	0.14
BP Tau	12036	J. Green	0.49	1	$20.43^{+0.03}_{-0.13}$	0.17	0.22	0.30
CS Cha	11616	G. Herczeg	0.8	4	$20.400^{+0.03}_{-0.15}$	0.16	0.21	0.29
CV Cha	$11616-S$	G. Herczeg	1.67	5	$20.45^{+0.05}_{-0.16}$	0.18	0.23	0.32
DE Tau	11616	G. Herczeg	0.59	1	$20.68^{+0.13}_{-0.18}$	0.31	0.39	0.54
DF Tau A	11533	J. Green	0.60	6	$20.93^{+0.03}_{-0.03}$	0.54	0.70	0.96
DK Tau A	11616	G. Herczeg	0.76	1	$20.85^{+0.23}_{-0.05}$	0.46	0.59	0.81
DM Tau	11616	G. Herczeg	0.0	1	$20.88^{+0.05}_{-0.09}$	0.48	0.62	0.86
DN Tau	11616	G. Herczeg	1.89	7	$20.45^{+0.13}_{-0.14}$	0.18	0.23	0.32
DR Tau	11616	G. Herczeg	1.2	8	$20.88^{+0.10}_{-0.08}$	0.48	0.62	0.86
GM Aur	11616	G. Herczeg	0.14	1	$20.90^{+0.03}_{-0.35}$	0.51	0.66	0.91
HD 100546	$8895-S$	S. Heap	0.36	9	$20.13^{+0.05}_{-0.38}$	0.09	0.11	0.15
HD 104237 (E140M)	$11616-S$	G. Herczeg	0.7	2	$20.15^{+0.03}_{-0.40}$	0.08	0.12	0.16
HD 104237 (G140M)	$9241-S$	A. Danks	0.7	2	$20.03^{+0.03}_{-0.03}$	0.07	0.09	0.12
HD 135344B	11828	A. Brown	0.30	2	$20.28^{+0.03}_{-0.27}$	0.12	0.16	0.22
HD 163296	$8065-S$	B. Woodgate	0.30	2	$19.90^{+0.03}_{-0.40}$	0.05	0.07	0.09
HN Tau A	11616	G. Herczeg	0.52	1	$20.75^{+0.13}_{-0.05}$	0.36	0.47	0.64
IP Tau	11616	G. Herczeg	0.24	1	$21.05^{+0.40}_{-0.32}$	0.72	0.94	1.29
LkCa 15	11616	G. Herczeg	0.62	1	$20.68^{+0.15}_{-0.09}$	0.31	0.39	0.54
RECX-11	11616	G. Herczeg	0.0	10	$19.70^{+0.03}_{-0.20}$	0.03	0.04	0.06
RECX-15	11616	G. Herczeg	0.0	10	$19.58^{+0.05}_{-0.18}$	0.02	0.03	0.04
RU Lup (COS)	12036	J. Green	0.07	11	$20.05^{+0.03}_{-0.06}$	0.07	0.09	0.13
RU Lup (STIS - E140)	$8157-S$	F. Walter	0.07	11	$20.23^{+0.10}_{-0.33}$	0.11	0.14	0.19
RW Aur A	11616	G. Herczeg	1.58	7	$20.25^{+0.05}_{-0.21}$	0.11	0.15	0.20
SU Aur	11616	G. Herczeg	0.9	1	$20.65^{+0.05}_{-0.40}$	0.29	0.37	0.51
SZ 102[e]	11616	G. Herczeg	1.13	12	$20.58^{+0.05}_{-0.18}$	0.24	0.31	0.43
TWA 3A	11616	G. Herczeg	0.7	13	$19.20^{+0.10}_{-0.20}$	0.01	0.01	0.02
TW Hya	$8041-S$	J. Linsky	0.0	14	$19.80^{+0.03}_{-0.25}$	0.04	0.05	0.07
UX Tau A	11616	G. Herczeg	0.21	1	$20.90^{+0.05}_{-0.17}$	0.51	0.66	0.91
V4046 Sgr	11533	J. Green	0.0	15	$19.85^{+0.03}_{-0.28}$	0.04	0.06	0.08
V836 Tau	11616	G. Herczeg	1.68	7	$20.70^{+0.28}_{-0.46}$	0.32	0.42	0.57

[a]Program IDs with $-S$ are STIS observations.

[b]   (1) Kenyon & Hartmann (1995); (2) Garcia Lopez et al. (2006); (3) Alencar et al. (2003); (4) Espaillat et al. (2007); (5) Gauvin & Strom (1992); (6) Hartigan & Kenyon (2003); (7) White & Hillenbrand (2004); (8) Gullbring et al. (2000); (9) Ardila et al. (2007); (10) Luhman & Steeghs (2004); (11) Herczeg et al. (2005); (12) Hughes et al. (1994); (13) Geoffray & Monin (2001); (14) Rucinski & Krautter (1983); (15) Quast et al. (2000).

[c]Garcia Lopez et al. (2006) A_V(lit) values are calculated from V, $B-V$ magnitudes from Testi et al. (1998)

[d]This chapter, $A_V(R_V) = (N(H\ I)/4.8 \times 10^{21}) \times R_V$

[e]Edge-on disk; emission is in reflected light

Table 3.3.   Additional Model Parameters

Object[a]	FWHM$_n$ km s^{-1}	FWHM$_b$ km s^{-1}	v_{HI} km s^{-1}
AA Tau	560	610	10
AB Aur	650	1110	30
AK Sco	440	730	-20
BP Tau	600	970	20
CS Cha	620	835	30
CV Cha	500	900	0
DE Tau	710	760	-60
DF Tau A	740	965	20
DK Tau A	750	520	-20
DM Tau	670	1020	30
DN Tau	550	1175	40
DR Tau	720	1160	40
GM Aur	340	730	-60
HD 100546	740	1310	-50
HD 104237 (E140M)	825	1260	-40
HD 104237 (G140M)	570	850	-40
HD 135344B	535	1090	-10
HD 163296	580	1500	10
HN Tau A	450	830	40
IP Tau	510	760	-70
LkCa 15	650	795	50
RECX-11	435	800	40
RECX-15	500	800	50
RU Lup (COS)	510	750	50
RU Lup (STIS - E140)	550	950	-30
RW Aur A	800	875	0
SU Aur	590	920	-60
SZ 102	700	760	-50
TWA 3A	340	480	-30
TW Hya	615	775	-50
UX Tau A	550	800	10
V4046 Sgr	485	880	-10
V836 Tau	550	750	0

[a]All targets have narrow-component heliocentric velocities of 49 km s^{-1} and broad-component heliocentric velocities of 39 km s^{-1}

3.3.3. Extinction from Optical/Infrared Colors and Spectrophotometry

Previously for the sample, extinction has been estimated from a variety of techniques applied to optical or near-infrared data, the wavelengths at which the stellar photospheric flux is at a maximum. These include extinction: 1) calculated by comparing the observed stellar colors to normal main-sequence stellar colors (e.g., Kenyon & Hartmann 1995), 2) computed from V and $(B - V)$ magnitudes (e.g., Testi et al. 1998), 3) estimated by comparing the SED of the star to accretion emission of less veiled T Tauri stars (e.g., Gullbring et al. 2000), 4) derived from Two Micron All Sky Survey magnitudes with assumed $J - H$ or $J - K$ photospheric colors and a standard interstellar reddening law (e.g., White & Hillenbrand 2004; Furlan et al. 2011), or 5) assessed from Paschen and Brackett line ratios compared to local line excitation models (e.g., Edwards et al. 2013). Recently, near-IR extinctions have been determined by fitting the observed target flux, the extinction corrected photospheric template flux, and the veiling of the photospheric template at a given wavelength (Fischer et al. 2011; McClure et al. 2013).

In addition to these literature values, new optical extinctions are obtained here from fitting a combination of accretion continuum and weak-line T Tauri star (WTTS) photospheric templates to the observed optical emission. The optical extinctions listed in Table 3.4 are obtained mostly from fits to broadband optical spectra (Herczeg & Hillenbrand 2014) or, for earlier spectral types, to optical photometry and accurate spectral types (Alecian et al. 2013). Following Herczeg & Hillenbrand (2014), optical extinctions for CV Cha, HD 104237, SU Aur, and AK Sco are recalculated here based on their spectral types and their flux-calibrated SITS spectra, while the extinction to RU Lup is calculated by assuming the blue continuum is flat. The uncertainties in extinction are $\sim 0.2-0.3$ mag, which for most stars in the sample is attributable to uncertainty in spectral type. The optical extinction estimates always assume a total-to-selective extinction of $R_V = 3.1$. Some variability in extinction has

Table 3.4.   Additional A$_V$ Values

Object	A$_V$(3.1) (This Chapter)	Furlan et al. (2011) A$_V$[a]	Optical A$_V$	Optical Ref.[b]	X-ray A$_V$[c]	X-ray Ref.[d]
AA Tau	0.34	1.95	0.34	2	6.07	1
AB Aur	0.51	0.25[e]	0.53, 0.65	2,1	0.39	1
AK Sco	0.08		0.84	4		
BP Tau	0.17	1.06	0.41	2	0.58	1
CS Cha	0.16				0.75	13
CV Cha	0.18		1.16	4	1.16	13
DE Tau	0.31	0.89	0.43	2		
DF Tau A	0.54	1.95	0.12	2		
DK Tau A	0.46	2.62			2.00	1
DM Tau	0.48	0.0	0.09	2	0.78	1
DN Tau	0.18	0.92	0.52	2	0.39	1
DR Tau	0.48	1.42			1.23	13
GM Aur	0.51	0.57	0.30	2	2.97	13
HD 100546	0.09					
HD 104237	0.08		0.01	4	0.50,1.1	2,3
HD 135344B	0.12		0.96	1	0.55	13
HD 163296	0.05		0.32	1	0.45,0.49	4,5
HN Tau A	0.36	1.06			1.29	1
IP Tau	0.72	1.70	0.46	2	2.91	13
LkCa 15	0.31	1.06	0.34	2	2.39	6
RECX-11	0.03		0.0	3	0.04	7
RECX-15	0.02		0.0	3	0.84	7
RU Lup	0.07		0.25	4	1.16	8
RW Aur A	0.11	0.50[f]			1.16	13
SU Aur	0.29	0.89[g]	0.67,0.76	2,4	2.13, 3.62	9,1
SZ 102	0.24					
TWA 3A	0.01				0.06	10
TW Hya	0.04		0.0	3	0.13	11
UX Tau A	0.51	0.46	0.57	2	0.39	13
V4046 Sgr	0.04				0.19	12
V836 Tau	0.32	1.49	0.64	2		

Table 3.4—Continued

Object	$A_V(3.1)$ (This Chapter)	Furlan et al. (2011) A_V[a]	Optical A_V	Optical Ref.[b]	X-ray A_V[c]	X-ray Ref.[d]

[a]Most values calculated from the Furlan et al. (2011) A_J values using the Rieke & Lebofsky (1985) extinction law.

[b] (1) Alecian et al. (2013); (2) Herczeg & Hillenbrand (2014); (3) Default by association; (4) DAO STIS G430L data

[c]Calculated from X-ray column densities using $N_H = $ (X-ray A_V) $\times$ $(4.8 \times 10^{21}/R_V)$ atoms cm^{-2} mag^{-1} assuming $R_V = 3.1$. Some targets have multiple X-ray columns from the literature.

[d] (1) Güdel et al. (2007a); (2)Skinner et al. (2004); (3) Testa et al. (2008); (4) Günther & Schmitt (2009); (5) Swartz et al. (2005); (6) Skinner & Güdel (2013); (7) López-Santiago et al. (2010); (8) Robrade & Schmitt (2007); (9) Franciosini et al. (2007); (10) Huenemoerder et al. (2007); (11) Stelzer & Schmitt (2004); (12) Argiroffi et al. (2012); (13) This chapter. See Section 3.3.4 and Table 3.5.

[e]Calculated from the DeWarf et al. (2003) A_J value cited in Furlan et al. (2011) using the Rieke & Lebofsky (1985) extinction law.

[f]Calculated from the White & Ghez (2001) A_J value cited in Furlan et al. (2011) using the Rieke & Lebofsky (1985) extinction law.

[g]Calculated from the Calvet et al. (2004) A_J value cited in Furlan et al. (2011) using the Rieke & Lebofsky (1985) extinction law.

been documented for a few of the sources (Herbst et al. 1994; Skrutskie et al. 1996), with AA Tau and RW Aur being a particularly notable examples (Bouvier et al. 2013; Rodriguez et al. 2013). One source, SZ 102, is ignored in this analysis because the star is seen only through scattered light from the edge-on disk, which yields an unreliable extinction. In §3.4 I compare these dust derived estimates of A_V to those derived above from the H I column density.

3.3.4. X-ray Spectral Fitting

For the vast majority of young stars the typical available X-ray data consists of CCD resolution (R $\sim 15 - 20$) spectra. Such spectra are normally parameterized using global fitting tools, such as XSPEC (Arnaud 1996). The X-ray emission from young stars is a combination of emission line and continuum emission. X-ray spectra for a range of young stars have been observed using grating spectroscopy with the *Chandra* HETG and LETG spectrographs and the *XMM-Newton* RGS spectrograph. These higher resolution spectra show the detailed emission line spectrum, which provides a firm foundation for modeling lower resolution CCD spectra, but usually provide only low signal-to-noise information on the continuum emission. Parameterization of CCD spectra can only be performed in limited ways, because the number of free parameters can quickly overwhelm the information content of the data. A common approach is to fit one or two temperature components and an interstellar column that introduces a low energy cutoff to the spectrum.

Two temperature components are almost always necessary for CCD spectra with a reasonable number of counts, because accreting T Tauri stars show two distinct sources of X-ray emission (originally discovered by Kastner et al. 2002). A harder (~ 1 keV) component is produced within the hot coronal magnetic loops of a relatively standard active star corona, while a cooler ($\sim 0.2 - 0.3$ keV) component is associated with the highly-localized accretion shock hot-spot. The cooler component has a complex thermal structure whose properties

are only crudely approximated by a single temperature.

I have compiled all the available information of X-ray determined hydrogen column densities for 25 of the stars being studied in this chapter (see Table 3.4), based on very similar two-temperature parameterization methods. Seventeen of these measurements are from the refereed literature, while for eight additional stars I present new measurements from Alex Brown in Table 3.5. The two-temperature parameterizations were derived using XSPEC assuming sub-solar metalicities in the $0.2 - 0.3$ range.

Compared to Lyα absorption, which directly traces the atomic hydrogen content, and optical/near-IR measurements, which trace the dust content, X-rays are attenuated by gas, grains, and molecules in the line of sight. The absorption derived from X-ray observations is usually expressed as an equivalent hydrogen column density ($N_H = $ N(H I) $+$ 2N(H$_2$) $+$ N(H II)), however the hydrogen column density is not directly measured. Available X-ray observations of CTTS cannot distinguish individual elements of the absorber. In fact, the equivalent N_H is derived using an assumed (usually solar) abundance pattern and tabulated absorption cross-sections since hydrogen does not dominate the X-ray absorption in the energy windows of *Chandra* and XMM-Newton ($0.3 - 8\,$keV or $2 - 40\,$Å). Therefore, the relation between measured X-ray absorption and column density does not involve empirical calibrations but depends only on the applied abundance pattern. In the relevant energy range, the X-ray absorption cross-section is dominated by helium (up to $50\,\%$) and oxygen (up to $\approx 40\,\%$). Depending on the considered wavelength, hydrogen provides only a small fraction ($\lesssim 22\,\%$) to the absorption cross-section (see Figure 3.5). Because the hydrogen column density is not directly measured in the X-ray absorption, and only derived from the strong He and O absorption, it is difficult to distinguish an absorber with solar abundances of H I from an absorber with fully ionized or fully molecular hydrogen. I thus take the equivalent N_H values in the X-ray to be the "best estimate" of N(H I) on the line of sight to the region of X-ray production and compare these values to those calculated in my Lyα absorption modeling in §3.4.

Table 3.5.   X-ray Measurements for Pre-Main Sequence Stars in the Sample

Star	Instrument	Obsid	N_H (10^{21} cm^{-2})	kT_1 (keV)	VEM_1 (10^{52} cm^{-3})	kT_2 (keV)	VEM_2 (10^{52} cm^{-3})	log L$_X$ (ergs s^{-1})
CS Cha	Chandra	6396	1.2±0.3	0.28±0.02	47.5±20.8	1.03±0.05	26.3±3.4	30.41
CV Cha	XMM	0203810101	$1.8^{+0.5}_{-0.4}$	0.8±0.1	$5.9^{+1.9}_{-1.2}$	$3.2^{+3.0}_{-1.0}$	8.3±1.5	30.3±0.1
DR Tau	XMM	0406570701	$1.9^{+0.7}_{-0.5}$	0.8±0.2	$1.0^{+0.5}_{-0.3}$	$3.5^{+4.4}_{-1.3}$	$1.9^{+0.5}_{-0.4}$	29.6±0.1
GM Aur	Chandra	8940	4.5±0.8	0.20±0.02	5.5±1.6	0.98±0.06	11.5±1.6	29.86
GM Aur	Chandra	9928	3.6±1.3	0.19±0.02	5.8±1.7	0.69±0.04	21.2±3.9	29.94
GM Aur	Chandra	9929	4.6±2.1	0.30±0.04	12.3±5.4	1.73±0.26	5.4±1.2	29.67
HD135344B	Chandra	9927	0.85±0.48	0.12±0.04	1.4±4.9	0.63±0.03	3.9±1.3	29.44
IP Tau	Chandra	10998	$4.5^{+1.9}_{-1.5}$	0.18±0.03	99^{+473}_{-71}	$1.0^{+0.2}_{-0.1}$	$7.1^{+1.7}_{-1.2}$	$30.1^{+0.6}_{-0.4}$
RW Aur A	XMM	0401870301	1.9±1.0	0.81±0.05	4.3±0.7	2.0±0.2	8.0±0.7	30.2±0.1
UX Tau A	Chandra	11001	$0.6^{+0.9}_{-0.6}$	$0.7^{+0.1}_{-0.2}$	$6.2^{+2.8}_{-2.1}$	$1.6^{+0.8}_{-0.3}$	8.5±2.1	$30.3^{+0.2}_{-0.1}$
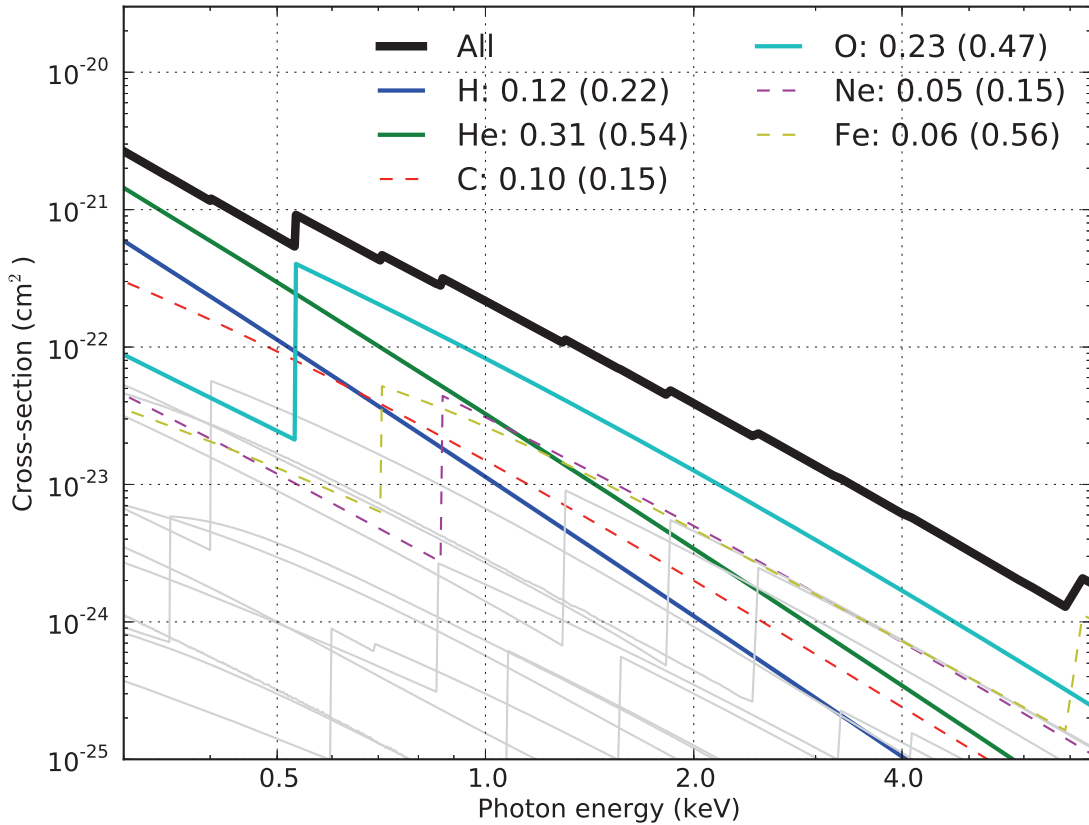
Fig. 3.5.— Absorption cross-sections at X-ray wavelengths from Balucinska-Church & Mc-Cammon (1992) with the contributions of the most important elements. Numbers give the mean fractional contributions to the total absorption cross-section in the displayed energy range (maximum fractions are given in parentheses). Thin gray lines indicate the absorption cross-sections of other elements.

3.4. Results

The Bohlin et al. (1978) relation as well as the relation between $E(B-V)$ and visual extinction, $(R_V = A_V/E(B-V))$ yields a relation between column density and visual extinction: $N(H\ I)/A_V = 4.8 \times 10^{21}/R_V$ atoms cm^{-2} mag^{-1}. Calvet et al. (2004) and Whittet et al. (2004) find extinction laws for Taurus that are unlike the diffuse ISM (for

which the Bohlin et al. (1978) relation is applicable). Both papers find a weak to nonexistent 2175 Å extinction bump. However, in the far-UV, where the reddening correction is most critical, there is almost no difference between diffuse ISM reddening laws and those Calvet et al. (2004) find more appropriate (see Figure 3 of Calvet et al. 2004). I include in Table 3.2 my calculated A_V values from the N(H I) - A_V relation assuming R_V values of 3.1, 4.0, and 5.5. Errors are not assigned to the extinction values due to uncertainty in the choice of R_V. I checked the Spearman's rank correlation coefficient and no correlation is seen between the N(H I) values and the inclination of the targets. This suggests that the majority of the H I being measured along the line of sight toward the targets is likely interstellar. I compare the literature A_V values listed in Table 3.2 to my computed A_V values in Figure 3.6.[3] Targets with less reliable fits due to low signal-to-noise or negligible Lyα flux (CV Cha, DE Tau, DK Tau, DM Tau, DN Tau, HN Tau, IP Tau, UX Tau, and V836 Tau) are marked in pink in the plot.

Most of the extinction values in the literature are larger than the values calculated from my best-fit column densities. For $A_V \gtrsim 0.5$ mag, column densities N(H I) $\gtrsim 10^{20.6}$ cm^{-2} would be required. The higher extinction values would require N(H I) $\gtrsim 10^{21}$ cm^{-2}. At these high column densities, attenuation along the line of sight would extinguish the stellar Lyα emission line completely (France et al. 2012a), which may be happening in the highest column density target, IP Tau (N(H I) = $10^{21.05}$ cm^{-2}). This fit is poor and may only be fitting continuum, in which case I could not reliably call this measurement an extinction value. However, 19 out of the 26 CTTSs and all of the Herbig Ae/Be stars observed in the sample show unambiguous evidence for broad Lyα emission lines, arguing that the true interstellar H I column densities to the Lyα emission must be lower than suggested by A_V values in the literature. Most of the 7 CTTSs with marginal Lyα emission detections (CV Cha, DK Tau, DN Tau, HN Tau, IP Tau, UX Tau, and V836 Tau) have large literature A_V

---

[3]I compare my A_V values using $R_V = 3.1$ because all of the literature A_V measurements assume that value of R_V.
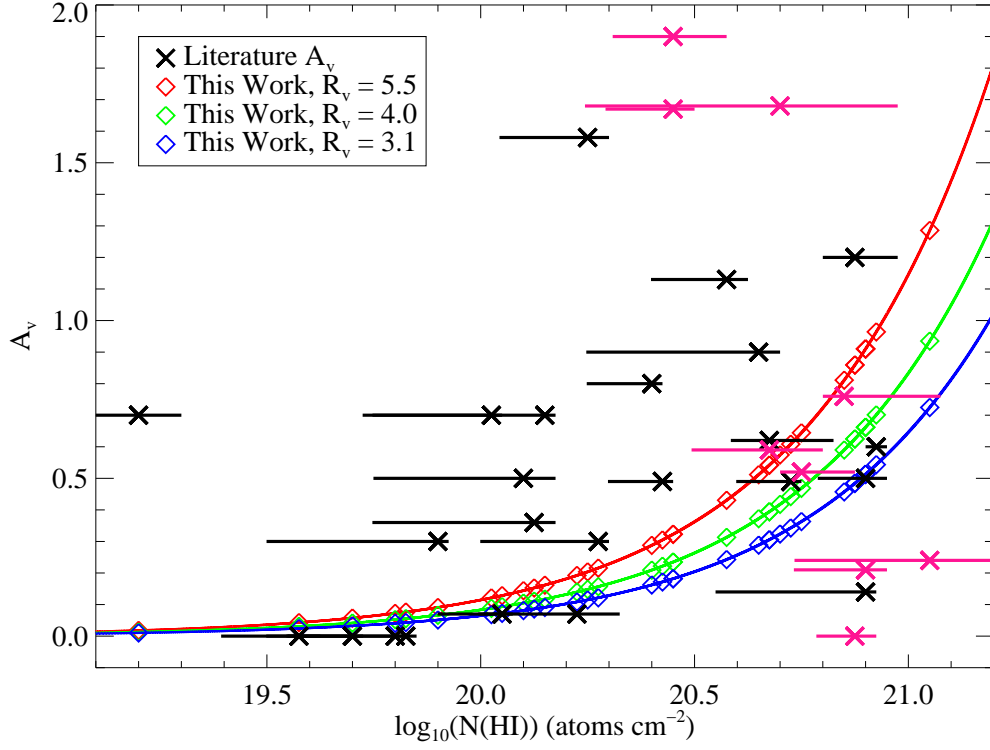
Fig. 3.6.— Literature values of A_V compared against my computed H I column densities (see Table 3.2). The black points are targets with reliable model fits, while the pink points (CV Cha, DE Tau, DK Tau, DM Tau, DN Tau, HN Tau, IP Tau, UX Tau, and V836 Tau) are targets with less reliable fits. The Bohlin et al. (1978) relation between H I column density and visual extinction for three different values of R_V is overplotted with points corresponding to the A_V values that are inferred in this chapter from the measured N(H I). The dust extinctions are typically higher than the gas extinctions.

values. However, as some of the extinction may be circumstellar, a non-interstellar dust-to-gas ratio in the disk (among other possibilities discussed in §3.5.2) may cause my column density measurements to be lower than expected from the published extinction values.
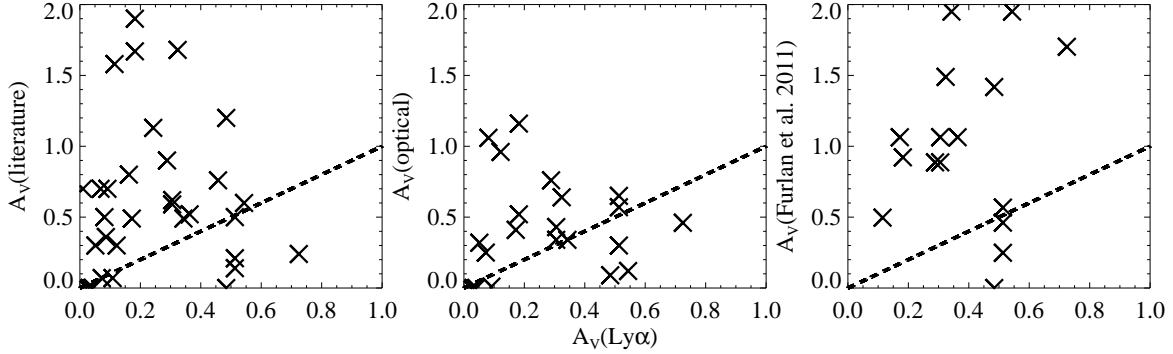
Fig. 3.7.— Comparison of my calculated visual extinction values from the far-UV analysis with the literature values from Table 3.2, as well as the optical, and IR (Furlan et al. 2011) values from Table 3.4. Dashed lines showing a 1:1 correspondence are overplotted. My values are generally lower than any other visual extinction calculation.

In Figure 3.7, I compare my calculated visual extinctions from the UV analysis (assuming $R_V = 3.1$) to the literature values in Table 3.2 as well as infrared (IR) values from Furlan et al. (2011) and optical values (both listed in Table 3.4 alongside my reprinted A_V values for comparison). The A_V values from this chapter are generally lower than any other calculation of the visual extinction. The optical extinctions are in best agreement with my values (though still larger for most targets), while the IR extinctions are consistently larger.

The reddening towards accreting K and M dwarf stars are difficult to accurately determine due to high amounts of veiling. Changing the spectral type, accretion continuum shape, and the relative contribution of the two can greatly affect the A_V value that is determined. The early-type stars in the sample (AB Aur, AK Sco, CV Cha, HD 100546, HD 104237, HD 135344B, HD 163296, and SU Aur) should have minimal veiling affecting their optical

spectra and relatively well-determined spectral types. The large photospheric flux of the hot early-type stars dwarfs the flux from the accretion excess at optical wavelengths, while the cooler late-type stars generally have higher veiling (Basri & Batalha 1990) due to their lower photospheric flux and consequently higher accretion flux to photospheric flux ratio. This makes early-type stars critical to determine if the veiling is introducing large errors in the determination of the extinction. I find that the discrepancy between the optical and Lyα determined extinction values is about the same in the early-type stars as the late-type stars in my sample. I conclude that veiling alone cannot be the primary cause of the extinction discrepancies between optical and Lyα based measurements.

In Figure 3.8 I compare the H I column densities obtained through my Lyα fitting procedure to the equivalent hydrogen column density, N_H, obtained in the X-ray. The X-ray columns are higher than the Lyα ISM columns in 23 out of 25 cases, implying that either a sizable fraction of circumstellar hydrogen does not contribute to the Lyα absorption (see the possibilities in §3.5.2), or that neutral hydrogen is depleted (most likely through ionization) with respect to O and He which dominate the X-ray absorption. Hydrogen is only of minor importance for the X-ray absorption so that changing the atomic hydrogen content has only a minor impact on the X-ray derived absorption. The X-ray columns may also be higher due to the accretion shock punching deep into the dense photosphere of the star. The soft X-rays produced in this shock region could thus probe the higher density photosphere, while the Lyα photons are emitted outside the densest shock region. Much of the extra absorbing material is very hot and contains hydrogen that is mostly ionized so that the soft X-rays produce an equivalent hydrogen column density (see §3.4) that is an overestimation of the neutral hydrogen column density measured by the Lyα absorption. I also detect in Figure 3.8 an increase in the ratio between Lyα and X-ray columns with increasing Lyα column density. This trend brings the two measurements closer to agreement as the Lyα column density increases, possibly suggesting an increased relative contribution to the total X-ray absorption from interstellar H I on higher column density sightlines.
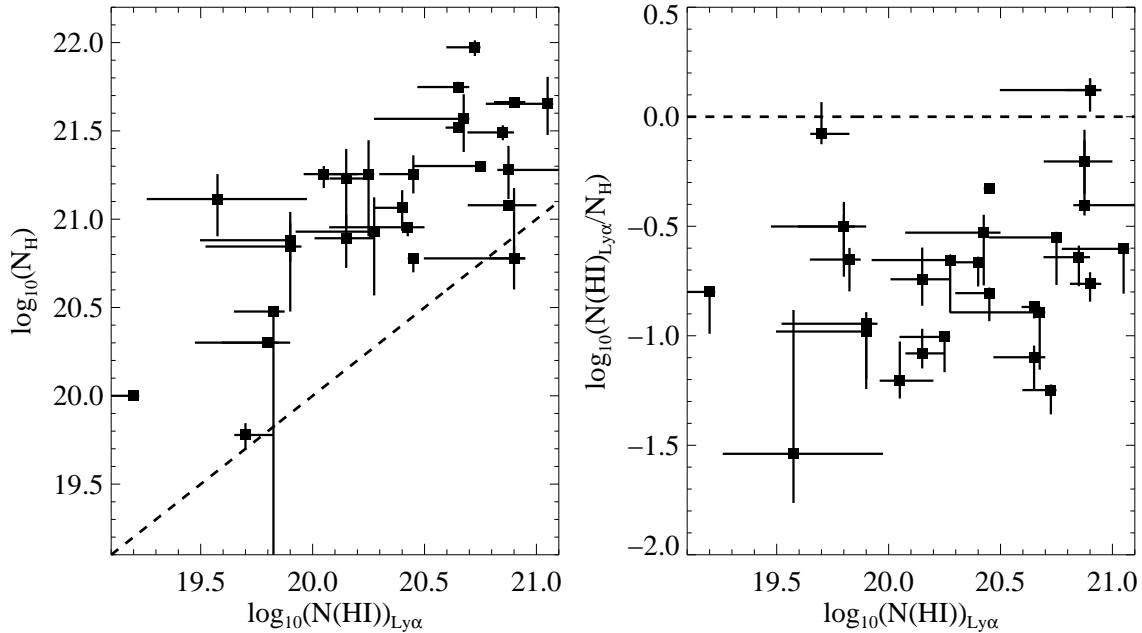
Fig. 3.8.— Comparison of X-ray equivalent hydrogen column densities (N_H) from the literature and my measurements with those from my Lyα absorption model fits. The X-ray equivalent hydrogen column density is taken as my "best estimate" of N(H I) derived from X-ray measurements. A dashed line showing a 1:1 correspondence is overplotted.

3.5. Discussion

3.5.1. Sources of Hydrogen Along the Line of Sight

Lyα absorption from partially ionized, primarily neutral, and primarily molecular gas can arise in several environments along the line of sight: in the protostellar outflow, in the disk atmosphere, and in the ISM. Figure 3.9 illustrates the important components that may contribute to the absorption of the pre-main sequence stellar emission. A systematic error associated with my fits is the absence of an outflow component in my model. Without a complete Lyα emission profile reconstruction (see e.g., Herczeg et al. 2004; Schindhelm

et al. 2012a,b), the Lyα outflow properties are challenging to determine. An outflow absorbs mostly the blueward side of the Lyα emission (see §3.3.2), but can affect the redward side of the line in smaller amounts as well. This leads to a systematic overestimation of the interstellar column density (and an underestimation of the total N(H I), see §3.5.2) as my best-fit value is a combination of the true interstellar column density and H I absorption from a protostellar outflow.

Far-Ultraviolet Spectroscopic Explorer (*FUSE*) measurements of H$_2$ along the line of sight to the Herbig Ae/Be stars (AB Aur, HD 100546, HD 104237, HD 135344B, HD 163296; Martin-Zaïdi et al. 2008) can be combined with my H I columns to check for agreement in the extinction values derived using the N(H I)-$E(B-V)$ and N(H I + H$_2$)-$E(B-V)$ relations in Bohlin et al. (1978). They can also be combined to give a hydrogen column ($N_H =$ N(H I) + 2N(H$_2$) + N(H II)) which directly compares with the equivalent hydrogen column measured by the X-ray absorption assuming a low ionization fraction. The H$_2$ column densities measured in Martin-Zaïdi et al. (2008) for the targets ($\sim 10^{16.5} - 10^{20.0}$ cm^{-2}) are generally much lower than my H I columns, making N_H only slightly larger than N(H I). So the *FUSE + HST* N_H values are still lower (~ 0.8 dex) than the X-ray N_H values for all of the Herbig Ae/Be targets except AB Aur. The AB Aur *FUSE* value is 0.2 dex higher than the X-ray value due to its larger molecular hydrogen column density (log(N(H$_2$)) = 20.03; Martin-Zaïdi et al. 2008). Using the Bohlin et al. (1978) relation for a combined H I and H$_2$ column, I obtained new extinction values for the Herbig Ae/Be targets that differed by 0.03 mag or less from those obtained from my H I columns alone. I conclude that the majority of this H$_2$ is most likely circumstellar rather than interstellar for my subset of targets based on their derived kinetic temperatures (56 - 758 K). Only AB Aur has H$_2$ temperatures less than 300 K, suggesting that it is the only Herbig Ae/Be star in the sample with an unambiguous interstellar H$_2$ absorption component.

To determine the amount of H I absorption that the circumstellar and interstellar material contribute along the line of sight, I compared N(H I) measurements from hot, main-
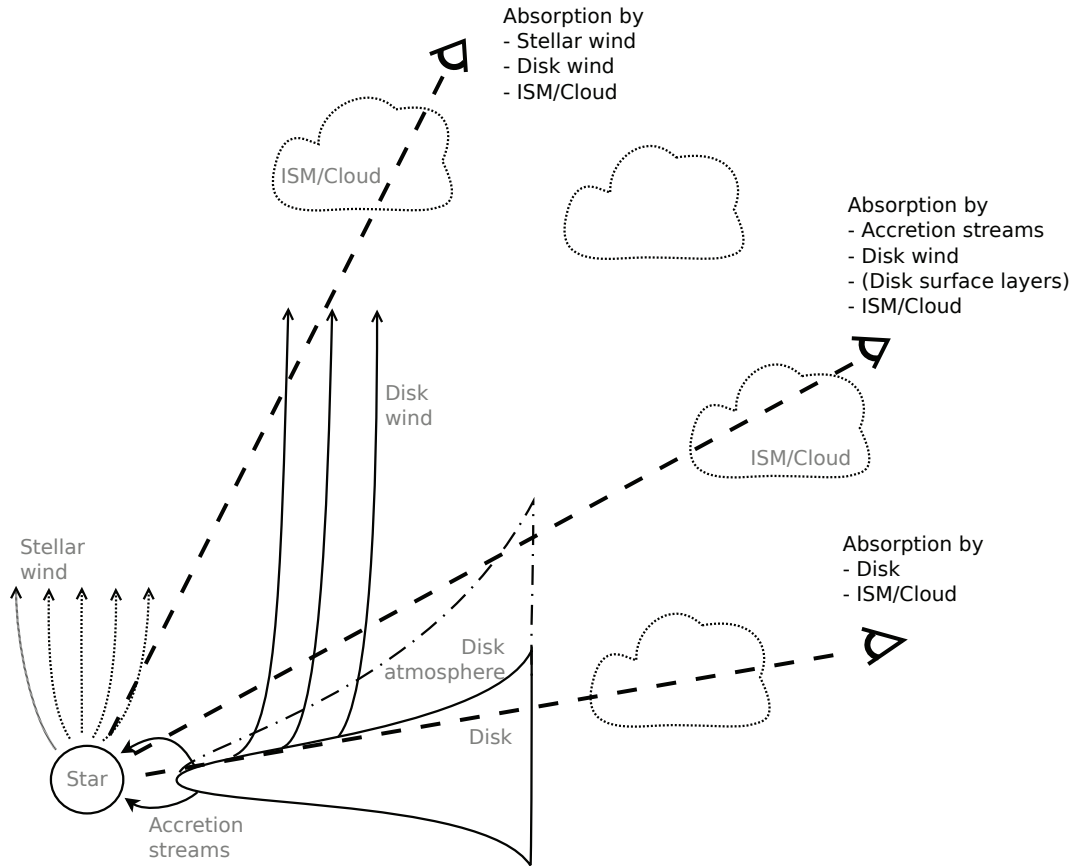
Fig. 3.9.— Sketch of the important components contributing to the absorption of the stellar emission. The absorption depends strongly on the viewing geometry. Lines with arrows indicate the plasma motion. Sightlines are dashed.

sequence stars, which should have little circumstellar material, to my Lyα measurements. I hoped to use stars from Bohlin et al. (1978) and Diplas & Savage (1994a) that sampled the Taurus-Auriga star-forming region ($168 < l < 181, -8 < b < -24, 80$ pc $< d < 220$ pc), but there were none to be found. I instead searched only in distance, requiring the stellar distance to be between 80 pc and 220 pc, which led to a large sample of stars. The average H I column for the hot stars in the Bohlin et al. (1978) sample is $\log(N(H\ I)) = 20.27$ and for those in the Diplas & Savage (1994a) sample is $\log(N(H\ I)) = 20.92$. My average H I column is $\log(N(H\ I)) = 20.39$. The similarity in the average H I columns in the three samples suggests that most of the absorption I am measuring is interstellar rather than circumstellar.

Using my new extinction values calculated from H I column densities, I can recalculate the intrinsic Lyα flux for the targets reported in France et al. (2012b). Due to my extinction values generally being lower than those used by France et al. (2012b) to reconstruct the Lyα flux, I find fluxes that can be up to ~ 6500 times smaller (DR Tau; France et al. (2012b) assuming $A_V = 3.2$ from Kraus & Hillenbrand 2009) than the Lyα fluxes reported in that work. However, most target Lyα fluxes average between 2 and 300 times smaller with my new extinction values being used. These lower flux values may greatly affect the chemistry of the gas in the protoplanetary disk region (Gorti & Hollenbach 2009; Gorti et al. 2009; Owen et al. 2012; Tanaka et al. 2013).

3.5.2. Discrepancy Among Lyα, Optical, and IR-based extinction determinations

Several possibilities exist for the disagreement between my Lyα based extinction measurement (which samples the gas along the line of sight, through both the ISM and circumstellar material, to the Lyα emitting region) and the optical and IR-based extinctions (which measure the dust column to the stellar optical/IR photosphere).

High dust-to-gas ratio – Some of the H I absorption could be located in the stellar vicinity in material that has a large dust-to-gas ratio or a non-ISM extinction law. In

particular, the dust-to-gas ratio may be enhanced in a static disk through radial drift of dust grains (Youdin & Shu 2002), and in star formation regions (e.g. Vuong et al. 2003). Because the dust-to-gas ratio may differ from that observed for the ISM in Bohlin et al. (1978), the relation derived in that work may not be appropriate for the circumstellar environment. Rachford et al. (2009) fit direct measurements of H_2 column densities, H I columns calculated from $E(B-V)$ values, and extinctions along translucent lines of sight, getting a relation very similar to Bohlin et al. (1978). However, my low H I column densities may be in the same vicinity as large amounts of dust that has not settled (high dust-to-gas ratio) contributing to the high A_V values measured in the optical and IR bands, making the Bohlin et al. (1978) relation provide inaccurate extinctions for my H I columns.

Molecular or ionized hydrogen – The hydrogen may also be mostly ionized or molecular in the stellar vicinity. If the hydrogen is mostly molecular, there would need to be a large column of H_2 to provide the extra extinction to match the optical A_V values listed in Table 3.4. The average $N(H_2)/N(H\,I)$ ratio needed (using the Bohlin et al. (1978) relation) is $N(H_2)/N(H\,I) \sim 1.7$, or a molecular fraction of 0.77, for the stars which have higher optical-based extinctions than $Ly\alpha$ derived extinctions. This molecular fraction is higher than any directly measured molecular fraction in the ISM measured in the UV, even on high-A_V sightlines. In particular, Rachford et al. (2002, 2009) and Burgh et al. (2007, 2010) find molecular fractions ≤ 0.76 along translucent lines of sight. However, a large molecular fraction may not be uncommon in a magnetized protostellar disk wind (Panoglou et al. 2012) and should be common in molecular clouds predicted by models (e.g. Maloney et al. 1996; Visser et al. 2009), though no direct measurement yet exists.

Using $N(H_2)/N(H\,I) \sim 1.7$ and my average derived H I column density, the average required H_2 column density to match the optical extinctions for the targets is $\log(N(H_2)) \sim 20.5$. The $T \sim 2500$ K H_2 absorber in the $Ly\alpha$ profile of AA Tau has $\log(N(H_2)) = 17.9$ (France et al. 2012a) and the ubiquitous H_2 fluorescence observed by France et al. (2012b) is explained by $\log(N(H_2)) < 20.0$ as well. The direct measurements of the Herbig stars in

Martin-Zaïdi et al. (2008) do find $\log(N(H_2)) \gtrsim 20.0$ for a few targets that are not studied in this chapter (HD 141569, HD 176386, HD 259431, HD 38087, and HD 76543), but these all have modest molecular fractions (≤ 0.35). However, the H_2 may be at T $\sim$ 500 K and cospatial with the CO absorption that is observed toward some CTTSs (McJunkin et al. 2013), which could possibly lead to a sufficient reservoir of H_2 to account for the additional reddening (assuming $N(H_2) \sim 10^4\,N(CO)$). If there is a large reservoir ($\log(N(H_2)) \gtrsim 20.5$) of warm (T $\sim$ 500 K) molecular gas at a high molecular fraction ($f_{H2} \gtrsim 0.8$), then dust associated with this medium may be sufficient to explain the discrepancy between my Lyα-based extinction measurements and those measured in the optical and IR.

If the hydrogen is mostly ionized so that there is little H I absorption, there would need to be large quantities of dust in the same vicinity to contribute to the visual extinction. This seems unlikely because any radiation that can ionize hydrogen should be strong enough to destroy dust grains as well. If the hydrogen is ionized by a time-dependent outflow (Pudritz et al. 2007), however, the dust grains may not yet be destroyed. The dust destruction may also be out of equilibrium (Finocchi et al. 1996), leading to large quantities of dust that is co-spatial with ionized hydrogen.

Outflows – Smaller H I column densities may be measured for an absorbing outflow that is not centered on the line of sight. A geometry where the H I is at the center of the Lyα absorption maximizes the H I column density and could lead to a better agreement between the Lyα and optical/IR-based extinction values. However, for most of the sources, the amount of H I in the outflow is small compared to the amount of H I in the ISM. I can compare the ISM H I column densities with the H I outflow columns that were derived from the inner disk Lyα profile reconstructions presented by Schindhelm et al. (2012b). For nearby sources like V4046 Sgr, $N(H\,I)_{ISM}/N(H\,I)_{outflow} \sim 10$. For a more distant source like DM Tau, $N(H\,I)_{ISM}/N(H\,I)_{outflow} \sim 200$. The average for all the targets in Schindhelm et al. (2012b) is $N(H\,I)_{ISM}/N(H\,I)_{outflow} \sim 74$. However, because there is generally a larger optical depth on the blueward side of the Lyα line, the outflow N(H I) may be significant

for some sources.

An outflow could also have a high molecular fraction (Panoglou et al. 2012) or a high dust fraction, which could contribute to the extinction discrepancy as described above. I calculated the amount of extinction that may be in the outflow by subtracting my Lyα H I columns from the optical and Furlan et al. (2011) extinctions. I then used this difference to calculate an average gas-to-dust ratio in the outflow by comparing the extinction from the outflow to the outflow columns in Schindhelm et al. (2012b). This gave me a gas-to-dust ratio for the outflow in the same manner as Bohlin et al. (1978). I find $\langle$N(H I)$_{outflow}/E(B-V)_{outflow}\rangle = 1.49 \times 10^{20}$ atoms cm^{-2} mag $^{-1}$ (assuming R$_V = 3.1$), ~ 30 times lower than the Bohlin et al. (1978) gas-to-dust ratio, meaning the outflow would need to be very dusty in order to explain the large difference between my Lyα extinctions and the optical/IR-based extinctions.

Geometric differences – Lastly, it could also be possible that the Lyα emission is produced far out in the system (at large radii, $\gtrsim 100$ AU from the star). The optical and IR observations may be probing the full extinction along the line of sight, whereas the Lyα profile that I observe the H I absorption against may be generated further out in the system so that I am only probing the outer parts of the disk and ISM. However, the large breadth of the Lyα profiles (Δv $\gtrsim 500$ km s^{-1}) points to an accretion origin for the emission, suggesting that the spatial differences between the two measurements may be only a few stellar radii. RU Lup is an exception as the Lyα emission in the narrow (0.2" $\times$ 0.06") STIS slit was spatially extended and produced in the outflow. Similarly, the broad Lyα emission (500 km s^{-1}) of HD 163296 in the STIS long-slit data extends out to a few 10's of AU, though is subdued compared to the central Lyα emission ($F_{broad}/F_{central} \sim 33 - 50\%$; P.C. Schneider (2013), private communication).

3.5.3. Origin of X-ray Absorbing Gas

Emission in different spectral regions can originate from very different parts of the spatially complex young stellar atmosphere and disk. The hot emitting gas seen in the FUV and X-ray regions can be produced in both the accretion hot-spot (which is thought to dominate in the FUV and soft-X-rays) and from more typical coronal magnetic loops (which produce most of the harder X-ray emission). The absorbing column seen by different spectral features therefore depends on where they originate in the accretion shock. In the soft X-rays, systematically enhanced absorbing columns have been measured for emission lines produced within the concentrated accretion shock (Brickhouse et al. 2010).

The absorption of the X-ray emission by the components shown in Figure 3.9 may lead to the excess X-ray column density that I detect. One possibility for the observed excess X-ray absorption is that a sizable fraction of the hydrogen is ionized while helium or at least oxygen preserve a sufficiently low ionization, e.g., in the accretion streams connecting the inner edge of the disk and the stellar surface. The inner parts of disks should have low ionization fractions (Dullemond et al. 2001; Najita et al. 2007). Disk winds should be mainly neutral initially (Safier 1993), but temperatures behind internal shocks in a jet can be sufficient ($\sim 10^6$ K; Güdel et al. 2007b; Schneider & Schmitt 2008) to produce extreme ultraviolet and X-ray photons that significantly ionize the material coming off the disk surface. Another possibility is that hydrogen is mainly molecular, located either in the outer parts of the protostellar system where the temperatures are sufficient for the existence of significant amounts of molecular hydrogen or in the ISM within the star forming region. Lastly, some kind of hot stellar wind might be transparent to Lyα photons but not to X-ray photons.

The excess X-ray absorption has been studied previously in some of the targets. Studies of the AA Tau system show that the absorption pattern of the circumstellar material differs from the ISM. The AA Tau system is viewed at high inclination ($i \approx 75°$; Andrews & Williams 2007b) and the star is periodically eclipsed by a disk warp. The associated optical

extinction can be directly measured (Bouvier et al. 2007b) and the optical brightness variations are accompanied by periodic changes of the X-ray derived column density (Schmitt & Robrade 2007). However, the associated X-ray absorption is about ten times larger than expected based on A_V. Due to the periodicity of the absorption pattern, it is possible to locate the associated absorber to a region about 0.1 AU from the star, i.e., close to the dust sublimation radius for this system. It is most likely that either the region around the disk warp is already dust-depleted or that the hot accretion streams provide the excess X-ray absorption since they are assumed to rigidly connect the star and the disk close to the radius of the disk warp. Other key targets are TW Hya and RU Lup which are seen almost pole-on but also show excess X-ray absorption (Robrade & Schmitt 2007; Günther & Schmitt 2008). Robrade & Schmitt (2007) interpret the extra X-ray absorption of RU Lup as being related to accretion flows and an optically transparent wind emanating from the star or the disk while Johns-Krull & Herczeg (2007) show that the FUV lines do not require a hot (stellar) wind in the case of TW Hya.

3.6.   Conclusions

I present interstellar H I column densities for 31 young stars determined from fitting absorption against the Lyα emission line. I find that the literature A_V values based on optical and IR observations are generally higher than the interstellar extinctions calculated from my derived column densities. I also find that the Lyα derived column densities are smaller than the X-ray columns (which trace the gaseous part of the absorption like my Lyα measurements) for my targets. Possible explanations for the extinction and column density discrepancies include 1) a high dust-to-gas ratio in the stellar vicinity, 2) the Lyα emission being produced far from the star, 3) the majority of the hydrogen being ionized or molecular, and 4) the N(H I) absorption being dominated by a non-centered outflow. The Lyα measurements determine the N(H I) column density well, while the X-ray and optical extinctions may also be probing ionized and molecular gas along the line of sight. Of these, I

consider large dust-to-gas ratios or high molecular fractions to be the most likely. However, these discrepancies may also arise because emission in the different spectral regions can be produced in many different regions around the star and disk. Thus, these discrepancies do not necessarily imply that any measurement is wrong, but may be the result of the spatial complexity of the young star and disk system. My data suggests that the majority of the H I absorption is interstellar in origin. Targets with larger Lyα columns have better agreement between the Lyα and X-ray column density measurements. My lower visual extinctions lead to smaller Lyα fluxes in the protoplanetary region than previously calculated, possibly affecting the gas heating and chemistry in the disk. In the next chapter, an H_2 fluorescence model will enable me to constrain the shape of the far-UV extinction curve and possibly the grain-size distribution in these protoplanetary disks.

4.   H2 Fluorescence Modeling

"A half-read book is a half-finished love affair."

- David Mitchell, *Cloud Atlas*

Measurements of extinction curves toward young stars are essential for calculating the intrinsic stellar spectrophotometric radiation. This flux determines the chemical properties and evolution of the circumstellar environment, including the environment in which planets form. H_2 emission lines pumped by stellar Lyα photons allow us to characterize the extinction curve by comparing the measured far-ultraviolet H_2 line fluxes with model H_2 line fluxes. The difference between model and observed fluxes can be attributed to the dust attenuation along the line of sight through both the interstellar and circumstellar material. The extinction curves are fit by a Cardelli et al. (1989) model, and the $A_V(H_2)$ for the 10 targets studied with "good" extinction fits range from 0.5 - 1.5 mag, with R_V values ranging from 2.0 - 4.7. Column densities and temperatures for the fluorescent H_2 populations are also determined and range from $\log_{10}(N(H_2)) = 15.2 - 22.0$ and $T = 1000 - 2500$ K. Some targets are not well fit by a Cardelli et al. (1989) extinction curve, suggesting grain evolution in the circumstellar environment.

4.1.   Introduction

The protoplanetary disk environment regulates the type of planets that can form around a young star. The stellar radiation, specifically the ultraviolet (UV) radiation, plays a strong role in chemical heating (Jonkheid et al. 2004; Nomura et al. 2007; Woitke et al. 2009) and processing (Aikawa & Herbst 1999; Bethell & Bergin 2009; Fogel et al. 2011; Bruderer 2013) in the disk. The interstellar and circumstellar media, however, can absorb the stellar

radiation along the line of sight and change the observed spectral energy distribution (SED). Characterizing the extinction allows us to recover the intrinsic stellar SED in order to better understand the environment of planet formation around these objects.

The canonical interstellar curve of Cardelli et al. (1989) describes the wavelength dependence of interstellar extinction using the color excess $(E(B-V))$ value and the R_V parameter which describes the grain size distribution $(R_V = A_V/E(B - V)$, with A_V being the visual extinction). The extinction curve is described by the formula $A_\lambda/A_V = a(x) + b(x)/R_V$ (where $x = 1/\lambda$), which is broken up into 4 regions (Infrared, Optical/NIR, Mid-UV, and Far-UV), with unique polynomial parameterizations of $a(x)$ and $b(x)$. The diffuse interstellar medium (ISM) has a canonical R_V value of 3.1 (Rieke & Lebofsky 1985) . Larger R_V values indicate grain populations with more large grains and less small grains, such as the $R_V \sim 5.6$ typical of dense molecular clouds (Cardelli et al. 1989). Allen et al. (2014) find an extinction curve toward the young cluster Cep OB3b that is intermediate between the $R_V = 3.1$ law used for the diffuse atomic ISM and the $R_V \sim 5.6$ law used for dense molecular clouds. Due to this observed variation in R_V, measuring the correct extinction curve toward individual targets is crucial.

In protoplanetary disk environments, grain growth can lead to non-interstellar dust populations and different gas phase abundances. Simulations of dust populations in disks have been performed by Birnstiel et al. (2012b), showing that turbulence in disks is necessary to explain the small grain population observed. The turbulence increases the collision rate, which helps create new small grains from larger grains. Vasyunin et al. (2011) argue that although disk grain growth allows UV photons to penetrate more easily into the disk interior, it also leads to increased gas phase molecular column densities due to the reduction of the total grain surface. Circumstellar grain growth can affect the extinction curve such that the shape is no longer well-described by the Cardelli et al. (1989) parameterization. In this case, the extinction curve has both interstellar and circumstellar components, with the line of sight passing through multiple different dust grain populations. In such a case, an

empirically-derived extinction curve is required.

Typically, line of sight extinction curves are measured via the pair method by comparing the SED of a reddened star to the SED of another star with similar properties, but little to no reddening (Rudnick 1936). This method assumes we can find an unreddened star that is similar enough to the star we are studying. More recently, Fitzpatrick & Massa (2005) have created a method to determine extinction curves using a stellar atmosphere model to create the unreddened SED rather than using an unreddened standard star. This method relies on having an accurate spectral type of the target star in order to create an accurate unreddened model spectra of the same type. However, this method cannot be applied to young, classical T Tauri stars (CTTSs) because the wavelength dependent veiling from excess accretion emission (e.g., Gullbring et al. 1998) cannot currently be predicted with sufficient accuracy to derive reliable stellar masses and radii (Hartigan et al. 1995).

In this chapter, I present a novel technique using H_2 line emission from the protoplanetary disk surface to constrain the wavelength dependent attenuation towards classical T Tauri stars. It is also important to explore the limitations of this new method in order to improve it in future work. Comparing H_2 fluorescent line fluxes to theoretical models allow me to calculate an extinction curve between $1100 - 1700$ Å. The broad (Lyα) profile of a protostar pumps H_2 electronic transitions which then fluoresce in the UV. Previous work modeling H_2 fluorescence in different targets and/or different techniques has been calculated by Wood et al. (2002), Herczeg et al. (2004, 2005), France et al. (2012b), and Hoadley et al. (2015a). I use a reconstructed Lyα profile (e.g., Schindhelm et al. 2012b) to pump the H_2 molecules and model the predicted fluorescence spectrum. Differences between the observed and theoretical H_2 fluorescence lines indicate attenuation occurring along the line of sight. This attenuation is caused by dust extinction and self-absorption in the interstellar and circumstellar medium. The effects can be separated using the derived properties of the emitting H_2 populations.

My measurements of the attenuation of UV photons by dust as a function of wavelength

requires several steps:

- Column density and temperature fit - I fit the long wavelength UV lines (1450 Å < λ < 1620 Å) where self-absorption is negligible by using the reconstructed Lyα profiles of Schindhelm et al. (2012b) and France et al. (2014) to excite the H_2 molecules. For a grid of column densities and temperatures, I compute the ground state H_2 populations and calculate the resulting fluorescent cascade. The minimum difference between the model and data line fluxes gives the best-fit parameters.

- Construct an initial attenuation curve - Dividing the observed line fluxes by the predicted line fluxes over the full wavelength range gives an initial curve showing the absorption occurring between the location of the H_2 fluorescence and the observations from HST. This attenuation can be attributed to interstellar and circumstellar extinction as well as self-absorption of the H_2 molecules, so I must next correct for the self-absorption in order to characterize the extinction.

- Self-absorption correction - To account for H_2 self-absorption in the disk, I find the transmission of each rovibrational transition at the best-fit column density and temperature. The transmission determines the amount of self-absorption that occurs, so I divide each line by its transmission value to determine the extinction curve.

- A_V and R_V fit - Searching a grid of A_V and R_V values and assuming a standard Cardelli et al. (1989) ISM extinction curve, I find the best-fit parameters for my self-absorption corrected extinction curve.

§4.2 presents the targets and observations used in this chapter. The H_2 fluorescence process is discussed in §4.3. The H_2 fluorescence models, self-absorption correction, and A_V-R_V extinction curve fits are described in detail in §4.4. §4.5 contains the results of all of the model fits, followed by a discussion in §4.6 comparing my work with previous extinction work as well as an exploration of the limitations of this new technique. I finish with a summary in §4.7.

4.2. Targets and Observations

I analyze the UV spectra of 16 young stars, which are a subset of the targets studied in the previous chapter. These targets are chosen because they have reconstructed Lyα profiles from Schindhelm et al. (2012b) and France et al. (2014), which I use to pump the H_2 molecules in my fluorescence model. The majority of the targets are in the Taurus-Auriga star-forming region, with a few from the η Chamaeleontis star-forming region or field stars. The ages of the young stars calculated from placing individual stars on HR diagrams range from 1-30 Myr, but most of the targets are 1-10 Myr old.

The majority of the data was obtained using the *Hubble Space Telescope* Cosmic Origins Spectrograph (*HST*-COS). The TW Hya data is archival Space Telescope Imaging Spectrograph (STIS) E140M data (PI - J. Linsky). COS is a slitless spectrograph with a 2.5" diameter, while the TW Hya data was taken through the 0.5" x 0.5" slit of STIS. The *HST*-COS data is comprised mostly of observations from the Disks, Accretion, and Outflows (DAO) of Tau guest observing program (PID 11616; PI: G. Herczeg), with a few targets from the COS Guaranteed Time Observing program (PID 11533 and 12036; PI: J. Green). The far-UV COS data were calibrated using the COS calibration program (CAL-COS), then aligned and co-added using the procedure described in Danforth et al. (2010). Multiple central wavelengths and focal-plane positions were used to cover the wavelength range from $\approx$1150-1750 Å while minimizing fixed pattern noise.

4.3. H$_2$ Fluorescence

H$_2$ fluorescence from protoplanetary disks can be used as a probe of the UV extinction curve along the line of sight towards these objects. The H$_2$ in the disk is pumped into electronically excited states by the stellar Lyα emission, and fluoresces as the electron returns to the ground electronic state, $X^1\Sigma_g^+$. This emission then travels through the interstellar and circumstellar media before being observed (see Figure 4.1). The interstellar and circumstellar

media can absorb some of the fluorescent emission along the line of sight, causing us to see a weaker and redder H_2 fluorescence spectrum. Comparing this reduced spectrum to a model fluorescence spectrum will reveal the extinction curve as the difference between the two.

I study seven strong H_2 progressions ((v', J') = (0,1), (0,2), (1,4), (1,7), (4,4), (2,12), and (3,13)) in the Lyman electronic band ($B^1\Sigma_u^+ - X^1\Sigma_g^+$). The progression lines arise from the H_2 in each (v', J') state of the excited $B^1\Sigma_u^+$ electronic state transitioning into many different (v'', J'') states of the ground electronic state. The branching ratios of the excited state determine the amount of flux distributed into each downward transition. I use reconstructed Lyα profiles from Schindhelm et al. (2012b) and France et al. (2014) to excite the H_2 molecules in my fluorescence model. These profiles are reconstructed using measured line fluxes from 12 H_2 progressions in the 1395 - 1640 Å wavelength range, where self-absorption is negligible. The total fluoresced flux from each progression is found by adding up the flux divided by the branching ratio for each line in the progression. These fluxes are divided by the equivalent width of the absorbing transition of each progression to get the flux incident on the H_2 at each progression wavelength. Model profiles which include H I absorption between the star and the H_2 are then fit to the 12 incident flux data points to determine the best fit Lyα profile. I then use these reconstructed profiles to predict the flux at shorter wavelengths, compare the prediction to observed H_2 line fluxes, and estimate a UV extinction curve.

Calculating the Lyα profiles with this method included certain assumptions. The fluorescing H_2 is assumed to be thermal, which I also assume in this chapter, and is supported by recent modeling work from Ádámkovics et al. (2016), who find that including Lyα irradiation onto the disk atmosphere produces a hot (1500 - 2500 K) molecular gas region which is hot enough to thermally excite the H_2 to vibrational levels capable of being pumped by Lyα photons. The H_2 gas that is absorbing and emitting in each progression is assumed to be well-mixed, co-spatial, and at rest with respect to the star. The co-spatial assumption is necessary due to the fact that there is not a good prediction for the H_2 distribution in the
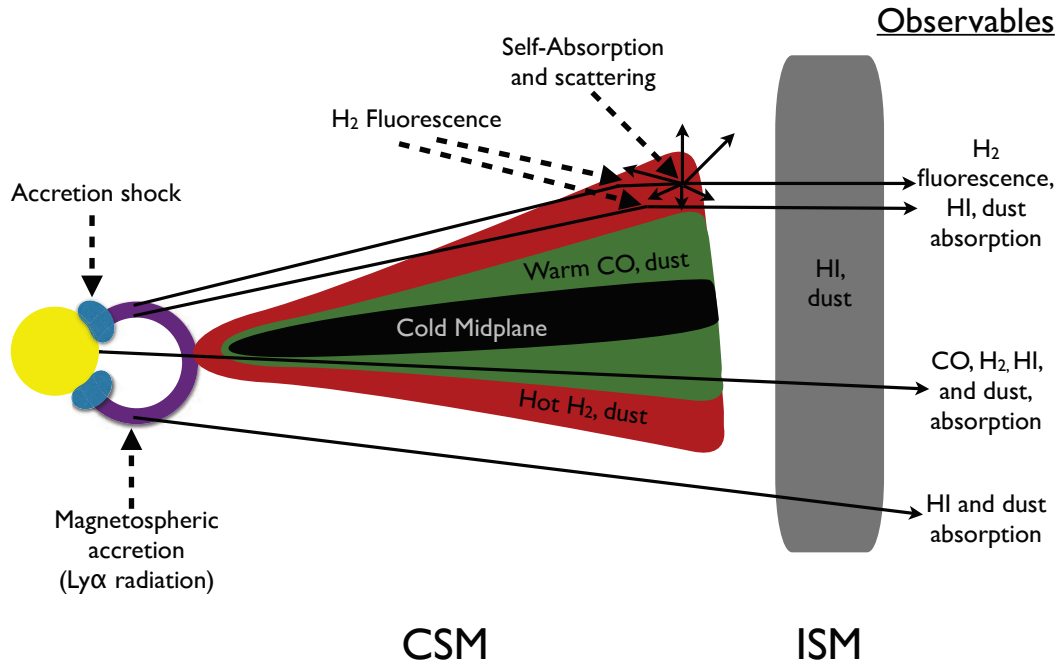
Fig. 4.1.— Sketch of some important observables along different lines of sight toward young stars. Different photon paths are the solid black lines, and the dotted black lines label important locations. The sketch is broken into circumstellar material (CSM) and interstellar material (ISM). The circumstellar material consists of the disk with components of a cold, unobservable, midplane, a warm middle layer with H_2, CO and dust, and a hot upper layer with H_2, dust, and possibly H I. The interstellar material consists of interstellar dust and H I. Lines of sight that pass through the lower layers of the disk and upper layers of the disk are shown as well as a line of sight that avoids the disk entirely. Only one side of the disk is shown, though H_2 fluorescence measurements probe emission from both sides of the disk. The amount of emission and absorption observed for any given source depends on inclination and the degree of disk flaring. Observables are listed on the right.

disk. I use this assumption in my model as well to simplify the geometric dependence in the radiative transfer. H_2 gas located in the disk will have velocities that are not completely at rest with respect to the star due to thermal and turbulent broadening as well as possible line of sight velocities if the gas is located in a disk wind. However, due to the observed, broad Lyα profile wings in these stars, even if the H_2 molecules have fairly large velocities with respect to the star (e.g., ~ 20 km s^{-1} in a disk wind; see Pontoppidan et al. 2011), it will not largely affect the reconstructed Lyα profiles as the profiles are essentially flat at these velocity scales.

Schindhelm et al. (2012b) do not account for the filling fraction (η) in their models, essentially setting $\eta = 1$. This implies that the H_2 completely surrounds the star, which is unlikely. Herczeg et al. (2004) find $\eta = 0.25$ for TW Hya, while Wood et al. (2002) find $\eta > 2$ for Mira B, which possibly indicates the preferential scattering of Lyα photons out of, or H_2 photons into, the line of sight. Better treatment of this filling fraction is needed in future Lyα profile reconstructions. Lastly, it is assumed that H I is the only opacity source between the stellar Lyα profile and the H_2. H I is the most prevalent gas species between the star and the H_2, producing a deep, broad absorption line. Other absorptions against the Lyα profile before reaching the H_2 would not be resolved by the rough resolution provided by the 12 progression data points; and, as discussed in Section 4.5.1, the dust in this region is also negligible. I discuss the impact of the reliance on the Schindhelm et al. (2012b) and France et al. (2014) Lyα profiles in the next section.

H_2 self-absorption, however, can mimic the effects of extinction, and must be taken into account before comparing the model to the observations (Wood et al. 2002). The fluoresced photons from a Lyα-pumped H_2 molecule falling back down to the ground state can be re-absorbed by another H_2 molecule along the line of sight before the photons escape the disk. The photons are then fluoresced again, possibly out of the original line of sight, causing that flux to be lost. This flux loss mimics interstellar absorption, where interstellar dust absorbs and scatters flux out of the line of sight as photons move from the star toward the instrument.

Self-absorption is stronger at shorter wavelengths since there is a larger molecular population in these lower rovibrational states. I can predict the amount of self-absorption that occurs in the disk by fitting the H_2 fluorescence lines at longer wavelengths ($\lambda > 1450$ Å, high v", J", where self-absorption is negligible) to derive a best-fit temperature and column density of H_2 molecules. These parameters then predict the amount of self-absorption based on the optical depth of H_2 in each absorbing level. The optical depths of the H_2 progressions for an average column density ($\log_{10}N(H_2) = 19.0$) and temperature (T = 1500 K) are shown in Figure 4.2. My 1450 Å self-absorption cutoff corresponds roughly to $\tau < 10^{-4}$.

4.4. Models

4.4.1. $\lambda > 1450$ Å Fits

To model the longer wavelength H_2 fluorescence lines, I used a directory of UV H_2 line properties from Abgrall et al. (1993a,b) containing laboratory wavelengths, upper and lower v and J values, band identifiers, Einstein A-values, and Γ values (see below) for 62,785 H_2 lines. I then calculated the oscillator strengths and branching ratios using the equations

$$f_{lu} = \frac{m_e c}{8\pi^2 e^2} \frac{g_u}{g_l} \lambda_{lu}^2 A_{ul} \tag{17}$$

$$f_{ul} = \frac{g_l}{g_u} f_{lu} \tag{18}$$

$$r_{branch} = \frac{A_{ul}}{\Sigma A_{ul}} \tag{19}$$

where f_{lu} and f_{ul} are the absorption and emission oscillator strengths, r_{branch} is the branching ratio, g_u and g_l are the degeneracies of the upper and lower states (equal to $2J_u + 1$ and $2J_l + 1$, respectively), and A_{ul} is the Einstein A-value. I used the reconstructed Lyα profiles of Schindhelm et al. (2012b) and France et al. (2014) as the pumping radiation and calculated the absorbing cross-sections of the H_2 molecules using

$$\sigma_{lu} = \frac{\sqrt{\pi} e^2}{m_e c b} f_{lu} \lambda_{lu} H(a, y) \tag{20}$$
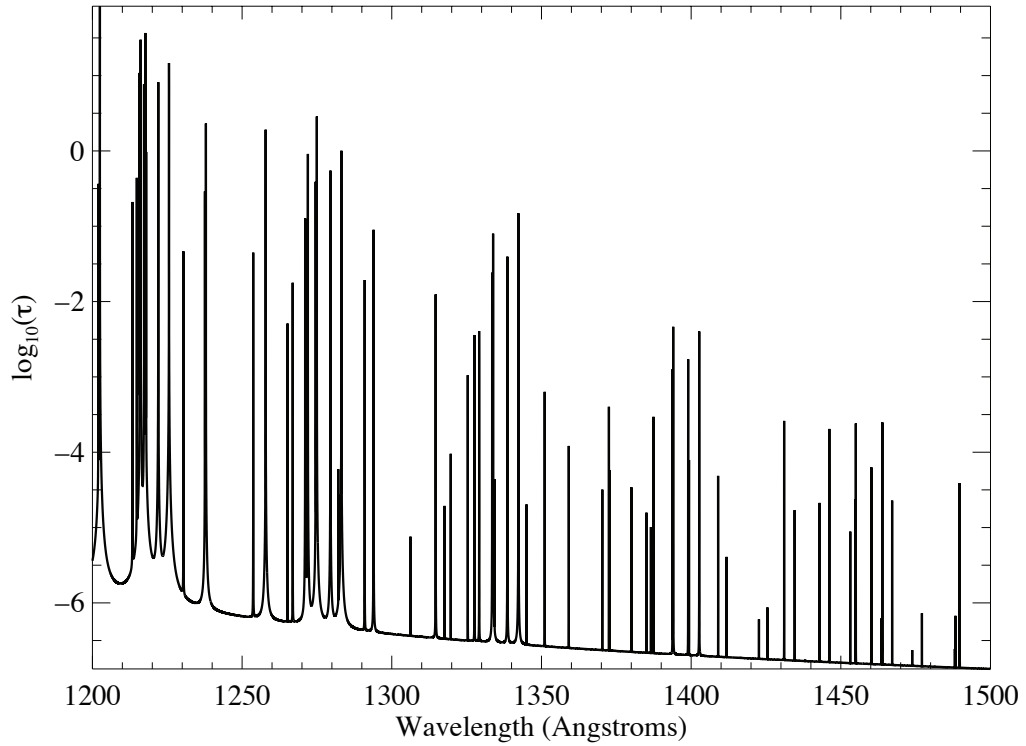
Fig. 4.2.— Plot of the logarithm of the optical depth as a function of wavelength for many of the far-UV H_2 lines. The optical depths assume $\log_{10}N(H_2) = 19.0$ and T = 1500 K. The increasing low-level opacity toward shorter wavelengths come from the broad Lorentzian wings of the $(v' - v) = $ (0-0) Lyman band absorption.

where $H(a, y)$ is the Voigt function with

$$a = \frac{\Gamma}{4\pi\Delta\nu} \tag{21}$$

$$y = \frac{|\nu - \nu_0|}{\Delta\nu} \tag{22}$$

$$\Delta\nu = \frac{b}{c}\nu \tag{23}$$

The Γ parameter is listed for each line in the Abgrall et al. (1993a,b) directory and is the inverse of the mean lifetime of the upper level. The y parameter takes into account shifts in the frequency of the line due to velocity shifts, and the b parameter is the Doppler b-value.

I thermally populated the H_2 molecular energy levels with each (v, J) level having a column density of

$$N(v, J) = N_{tot}\frac{(2J + 1)(2s + 1)e^{-E(v,J)/k_bT}}{\sum_{v,J}(2J + 1)(2s + 1)e^{-E(v,J)/k_bT}} \tag{24}$$

where s is the nuclear spin (0 for even J-values, 1 for odd J-values), $E(v, J)$ is the energy in each (v, J) state, N_{tot} is the total column density in all states, and k_b is the Boltzmann constant. The ground state energies are defined by

$$E(v, J) = G(v) + F_v(J) \tag{25}$$

$$= \omega_e(v + \frac{1}{2}) - \omega_e x_e(v + \frac{1}{2})^2 + ... + B_vJ(J + 1) - D_vJ^2(J + 1)^2 + ... \tag{26}$$

where G_v represents the energy from the vibrational state v, and $F_v(J)$ represents the energy from the rotation in a given vibrational level. The terms ω_e, x_e, B_v, and D_v are measured constants (Herzberg 1950).

The optical depth in each absorption line is the combination of the absorbing cross-section and the column density in each line:

$$\tau = N(v, J)\sigma_{lu}. \tag{27}$$

However, as some absorption lines overlap, I must correct the optical depths so that the lines do not over-absorb the available Lyα flux. The flux is shared between adjacent absorbing

transitions using the formula for the corrected optical depth (Liu & Dalgarno 1996; Wolven et al. 1997):

$$\tau_{corr} = \tau \frac{\tau}{\Sigma \tau} \qquad (28)$$

where I sum over the optical depths of all of the lines sharing the wavelength space.

The amount of flux absorbed by each absorbing transition is then

$$F_{abs} = \int (1 - e^{-\tau_{corr}}) F_{Ly\alpha} \qquad (\text{erg cm}^{-2}\ \text{s}^{-1}) \qquad (29)$$

where $F_{Ly\alpha}$ is the reconstructed Lyα flux profile I integrate over the full Lyα line. This flux is then stored in an array of excited states labeled by the v' and J' values. The model absorption of the H_2 against the Lyα flux is shown in the left plot of Figure 4.3 for TW Hya. Warm H_2 absorption superimposed on the Lyα emission spectra has been observed in DF Tau, V4046 Sgr, and AA Tau (Yang et al. 2011; France et al. 2012a). The right plot of Figure 4.3 shows the procedure for the optical depth correction for overlapping lines. The flux in the excited states is redistributed into the H_2 fluorescent lines. Each fluorescent line out of a particular excited state is assigned a flux equal to the branching ratio of that state multiplied by the flux in the excited state. The absorbed flux is thus completely re-distributed into the H_2 fluorescence.

I compared the flux (in erg cm^{-2} s^{-1}) in the model lines to the flux in the matching line in the data focusing on seven strong progressions: $(v', J') = (0,1), (0,2), (1,4), (1,7), (4,4), (2,12)$, and $(3,13)$. I measured the data line fluxes using the interactive multi-Gaussian line-fitting code of France et al. (2012b). The code fits the background flux with a second-order polynomial, and fits the H_2 emission with a Gaussian line shape convolved with the COS line spread function. For the TW Hya STIS data, unconvolved Gaussians were used for the H_2 line fits. I checked the data and removed lines that were blended, had low signal-to-noise, or were badly fit by the H_2 line-fitting code. This means that not every target has the same number of studied lines as other targets, and that certain wavelength regions may be less populated for some targets. I searched over a grid of logarithmic column densities ranging
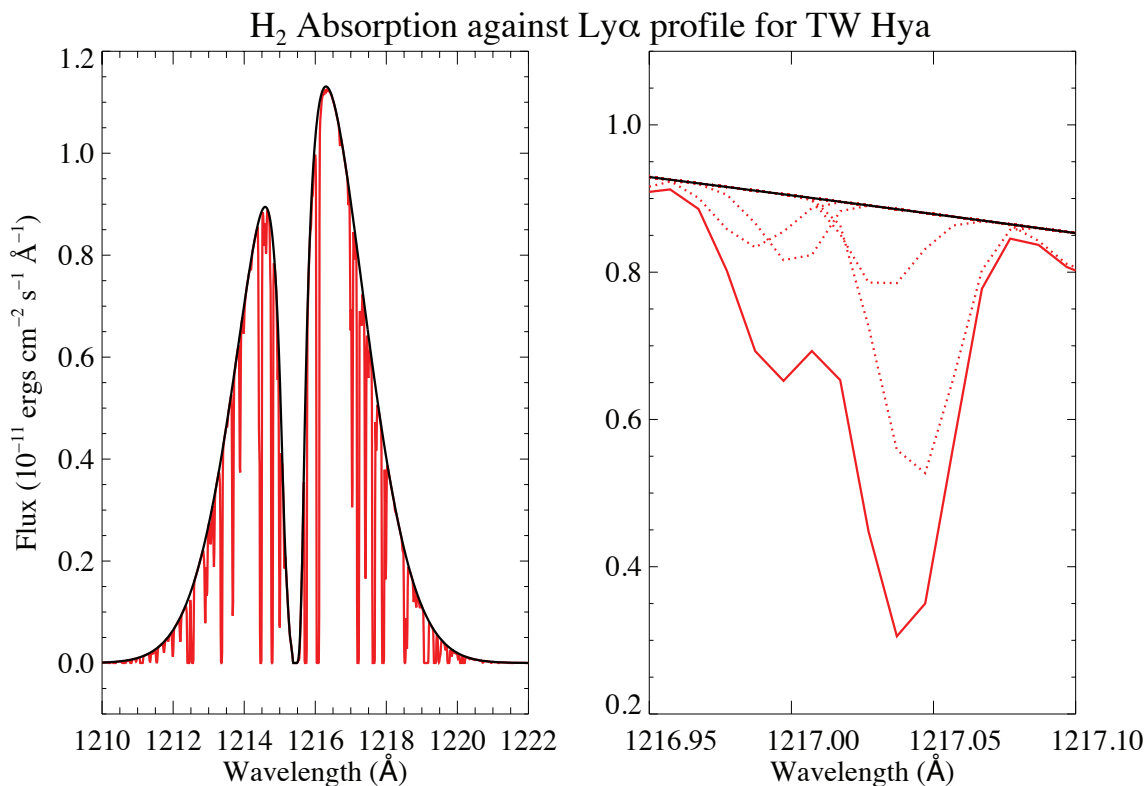
Fig. 4.3.— Plot showing the H$_2$ absorption against the pumping Lyα radiation. Left: Full wavelength figure of the pumping Lyα profile in black and the absorbed profile in red. Right: A zoom-in of the absorption against the Lyα profile showing four absorption lines (dotted lines) sharing the optical depth space. The four lines combine to create the solid red absorption line.

from 17.5 to 22.5 dex in increments of 0.1 dex, and a grid of temperatures ranging from 500 to 3500 K in increments of 100 K. The column density fit had to be extended down to $\log_{10}(N(H_2)) = 15.0$ for DR Tau, which was found to have a very low column density of $\log_{10}(N(H_2)) = 15.2$. I only compared the flux in the model and data lines. Line shapes were not important for the total flux comparison and were not calculated in the present model (see Hoadley et al. (2015a) for a detailed H_2 line shape analysis).

To assess the impact of the reliance on the Schindhelm et al. (2012b) and France et al. (2014) Lyα profiles, I performed a grid search to determine the best-fit absorbed flux to the data. I took a grid of 0% - 200% of the absorbed flux in my Lyα-pumped model (F_{abs}) for each progression, with steps of 10%. I then calculated the resulting flux in each H_2 emission line with the branching ratios as before. For most of the progressions of each target, I find best-fit absorbed flux values within 30% of the flux absorbed from the Schindhelm et al. (2012b) and France et al. (2014) Lyα profiles. Only the (4,4) progression of some targets is outside of this range, sometimes needing $\sim 50\%$ more absorbed flux into the progression to explain the fluoresced flux. I hope to better understand this anomalous progression in future work by modeling each progression with a different H_2 column density and temperature (see Section 4.6).

The best-fit temperatures and column densities from the fluorescence flux fits are listed in Table 4.1. Figure 4.4 shows the ratio of the data line fluxes over the model line fluxes for RECX-11. The flux difference at $\lambda \sim 1180$ Å is a factor of 8.1, at $\lambda \sim 1280$ Å is a factor of 2.0, and at $\lambda \sim 1380$ Å is a factor of 1.1. The strong wavelength dependence of the model/observed flux ratio is the result of the combined effects of self-absorption and dust attenuation.

Table 4.1. H_2 Model Best-Fit Parameters

Object	$\log_{10}(N_{H2})$	T (K)
AA Tau	$20.0^{+0.3}_{-0.4}$	1000^{+800}_{-200}
BP Tau	$18.1^{+0.2}_{-0.4}$	1600^{+500}_{-300}
DE Tau	$18.0^{+1.1}_{-1.4}$	1700^{+1100}_{-600}
DF Tau	$18.1^{+0.2}_{-0.3}$	1300^{+600}_{-200}
DM Tau	$22.0^{+0.4}_{-0.7}$	1200^{+700}_{-200}
DR Tau	$15.1^{+0.4}_{-0.7}$	1500^{+200}_{-300}
GM Aur	$20.0^{+0.5}_{-0.7}$	1500^{+1100}_{-200}
HN Tau	$20.1^{+0.3}_{-0.3}$	1000^{+800}_{-200}
LkCa15	$18.0^{+0.3}_{-0.6}$	1500^{+500}_{-300}
RECX-11	$18.1^{+0.2}_{-0.1}$	1800^{+600}_{-300}
RECX-15	$20.1^{+0.4}_{-0.5}$	1400^{+800}_{-200}
RU Lupi	$18.0^{+0.2}_{-1.4}$	1800^{+800}_{-600}
SU Aur	$18.5^{+0.2}_{-0.3}$	1200^{+500}_{-200}
TW Hya	$19.0^{+0.8}_{-1.0}$	2500^{+1000}_{-800}
UX Tau	$21.0^{+0.6}_{-0.6}$	1000^{+700}_{-200}
V4046 Sgr	$19.5^{+0.5}_{-0.5}$	1700^{+600}_{-200}
Avg.	19.0	1500
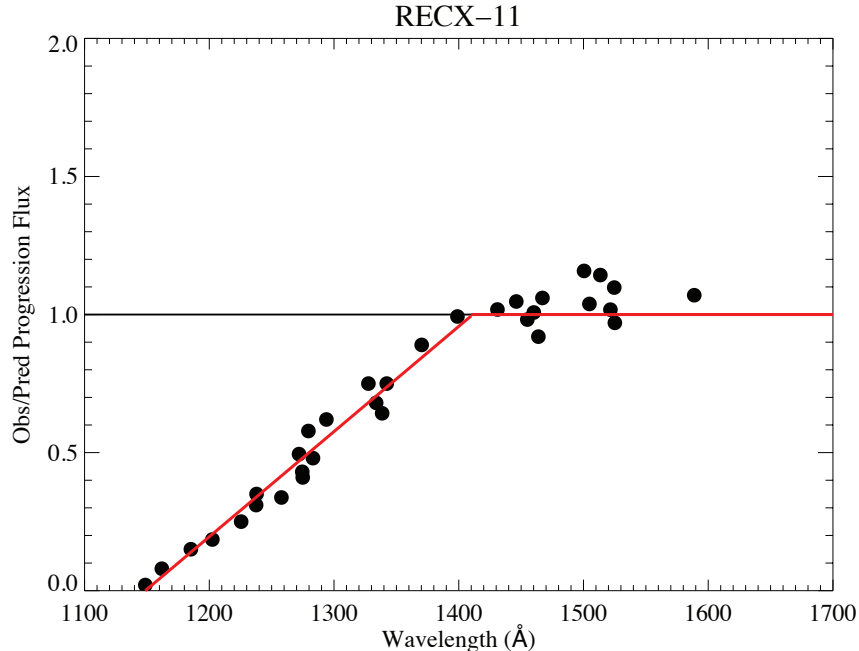
Fig. 4.4.— Plot of the data H_2 line fluxes divided by the model H_2 line fluxes for RECX-11 before the self-absorption correction. A fit to the falloff at short wavelengths is shown as a linear function overplotted in red for display.

4.4.2. Self-Absorption Calculation

In the case of an optically thick H_2 population, light previously fluoresced by H_2 molecules can be reabsorbed by nearby H_2 and subsequently scattered out of the line of sight. Self-absorption preferentially occurs at shorter wavelengths where the energy levels are well populated. Attenuation due to dust extinction also increases with decreasing wavelength. This process can thus be confused with extinction and must be corrected for in the calculations. To correctly account for self-absorption, a full radiative transfer calculation should be used. This involves taking into account velocity broadening (including thermal and turbulent broadening along with potential line of sight velocities due to disk winds), as well as geometry effects (such as the clumping and density gradients of the disk material).

The thermal and turbulent velocities are treated by including a physically motivated Doppler b-value in the model. I calculated a range of b-values assuming the turbulent velocity was $\lesssim$ 1.0 km s^{-1} and that the H$_2$ rotational temperature was $\lesssim 5 \times 10^3$ K. The b-values ranged from 0.0 - 3.0 km s^{-1}, of which I chose 1.5 km s^{-1} as a representative value. There is evidence of disk winds (e.g., Pontoppidan et al. 2011; Schneider et al. 2013) which are largely perpendicular to the disk, so I therefore neglect the radial velocity offsets with respect to the stellar Lyα. As mentioned in Section 4.3, due to the Lyα profiles being very broad, even H$_2$ molecules in winds that are not perpendicular to the disk with velocities of ~ 20 km s^{-1} have negligible impact on the amount of Lyα flux absorbed. However, the density distribution of the disk gas is currently not well known in disk models. Without an approximation of the expected clumpiness, the calculation is prohibitively computationally expensive. To simulate the effect of self-absorption without knowing the disk gas density distribution, I used the best-fit temperature and column density of the H$_2$ fluorescence lines to calculate the optical depth (Equations 27 and 28) of each transition. The transmission is a direct measure of the total self-absorption so that dividing the observed/predicted plot points in Figure 4.4 by the corresponding line transmission gives the self-absorption corrected curve. I plot the self-absorption corrected curves for all 16 targets as black points in Figure 4.5a and Figure 4.5b with the extinction curve fit overplotted in blue.

4.4.3. Extinction Curve Fits

I found the best-fit UV extinction curve by comparing the self-absorption corrected curves to Cardelli et al. (1989) extinction curves for a grid of A$_V$ and R$_V$ values. I ranged the A$_V$ value from 0 to 2 in steps of 0.1. Higher extinction values correspond to larger interstellar H I values through the Bohlin et al. (1978) relation of N(H I)/E$(B-V) = 4.8 \times 10^{21}$ atoms cm^{-2} mag^{-1} because E$(B-V) =$ A$_V$/R$_V$. I set A$_V = 2$ as the upper limit because for A$_V = 2$ and R$_V = 3.1$, N(H I) $= 3.1 \times 10^{21}$ atoms cm^{-2}, which would lead to a Lyα profile completely absorbed by interstellar H I (France et al. 2012a; McJunkin et al. 2014). The R$_V$
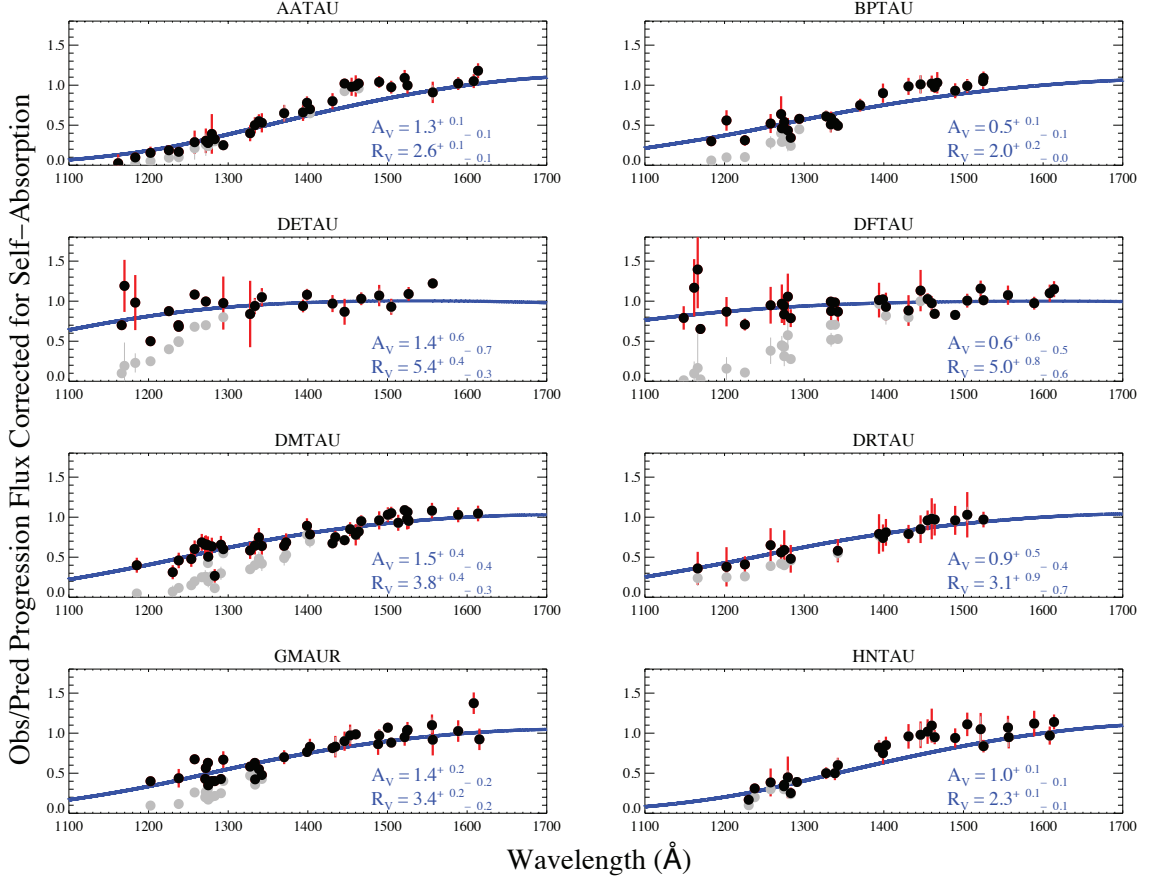
Fig. 4.5a.— Far-UV extinction curve fits for the first half of the targets. The black points are corrected for self-absorption, the grey points are before the self-absorption correction, and the blue line is the extinction curve. Errors on the black points are shown in red, while the grey points also have grey errors. Some error bars are smaller than the data points. Extinctions of $A_V(H_2) = 2.0$ represent the numeric upper limit of the parameter searches. Targets such as V4046 Sgr and TW Hya have extinction fits with large $A_V(H_2)$ values, but the scatter in the V4046 Sgr data points is consistent with an extinction of zero, and the lack of lines in TW Hya at the shortest wavelengths fails to constrain the extinction well.
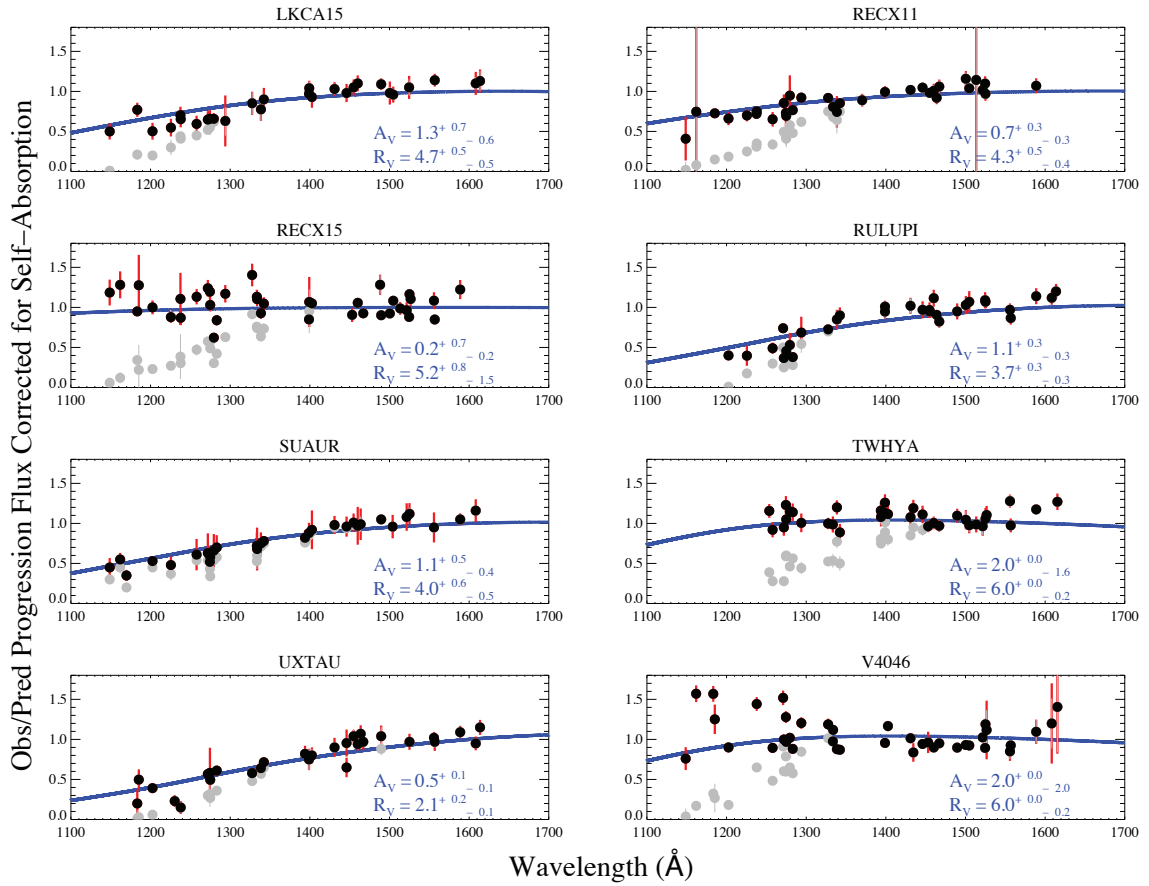
Fig. 4.5b.— Same as Figure 4.5a for the second half of the targets.

values ranged from 2 to 6 in steps of 0.1 based on the spread of well-determined literature R_V values ($R_V = 2.1$ for HD 210121 (Welty & Fowler 1992) to $R_V \approx 5.7$ for HD 36982 (Cardelli et al. 1989; Fitzpatrick 1999)). The minimum χ^2 value between the models and the data was chosen as the best-fit extinction model. The extinction curve fits are plotted in blue in Figure 4.5a and Figure 4.5b.

4.5. Results

4.5.1. Best-Fit Models and Parameters

The best-fit H_2 column densities and temperatures are listed in Table 4.1. The column densities range from approximately $\log_{10}N(H_2) = 18.0$ to $\log_{10}N(H_2) = 20.0$, while the temperatures are centered around $T = 1500$ K with large errors. Within the large errors, the targets are all at roughly the same temperature. The error bars for each parameter were calculated by increasing (or decreasing) the parameter from the best-fit value, keeping other parameters constant, and finding the point where the χ^2 value increased by one. Within the error bars, the temperatures are consistent with those found in the H_2 radiative transfer model of Hoadley et al. (2015a) for all targets except AA Tau. Hoadley et al. (2015a) find a temperature for AA Tau of 4000^{+250}_{-1500} K, while my temperature is much lower at 1000^{+800}_{-200} K. This could be due to Hoadley et al. (2015a) performing an initial extinction correction to the Lyα flux as well as the corresponding H_2 fluorescent flux using literature A_V values before fitting the data with their model, while I do not. Previous H_2 line studies (Ardila et al. 2002; Herczeg et al. 2004; France et al. 2012a; Hoadley et al. 2015a) have also found temperatures for these types of targets in the range 1000 - 4000 K. The temperatures are difficult to tightly constrain due to the fact that one needs to measure the weaker, higher-J lines, which often blend into the noise of the data.

The best-fit extinction curves for the targets can be seen in Figure 4.5a - Figure 4.5b and the best-fit $A_V(H_2)$ and R_V values for all the targets are listed in Table 4.2. Black points in

Figure 4.5a - Figure 4.5b are the points corrected for self-absorption, while the grey points are the data before the self-absorption correction. Some targets (such as V4046 Sgr and RECX-15) have extinction curves that are not well-fit by the model curve (defined in Section 4.5.2). This hints that the disk may be contributing significantly to the extinction and that grain processing could be occurring in the disk vicinity. The ISM and disk likely have different R_V values, possibly leading to the poor single-R_V fits. The circumstellar material that I am probing is most likely material outside the fluorescence location. Hoadley et al. (2015a) find outer limits of the H_2 fluorescence radii (r_{out,H_2}) which range between 0.87 and 12.03 AU for the overlapping targets. Dust inside the H_2 fluorescence radii is unappreciable if we assume an interstellar dust-to-gas ratio as well as an upper limit on the N(H I) between the star and the H_2 fluorescence radii from Schindhelm et al. (2012a). They find the N(H I) between the star and the fluorescent CO disk surface is $\log_{10}(N(H I)) \sim 19 - 20$ (Schindhelm et al. 2012a, table 5). The amount of N(H I) between the star and the H_2, which lies closer to the star, is necessarily larger. The dust-to-gas ratio would need to be ~ 100 times interstellar to have appreciable dust in this region.

4.5.2. Model and Parameter Analysis

Targets with good extinction fits, defined as those with reduced χ^2 values between 0.75 and 1.25, are listed in Table 4.3 with $A_V(H_2)$ values from this chapter as well as values from previous works. The literature extinctions in the Table utilize methods in four different wavelength regions: IR, UV, optical, and X-ray. For clarity, extinctions derived from the IR and X-ray measurements are designated as A_V(IR) and A_V(X-ray) respectively, with the UV method of the previous chapter designated by A_V(N(H I)), and the optical method of Herczeg & Hillenbrand (2014) designated by A_V(SED). Furlan et al. (2011) derive IR extinction values using Two Micron All Sky Survey magnitudes, assumed $J - H$ or $J - K$ photospheric colors, and a standard interstellar reddening law. In the previous chapter, I used interstellar H I absorption against the stellar Lyα profile to measure N(H I) and derive

Table 4.2.   Extinction Model Best-Fit Parameters

Object	$A_V(H_2)$	R_V	$A_V(H_2)$ $(R_V = 3.1)$[a]
AA Tau	$1.3^{+0.1}_{-0.1}$	$2.6^{+0.1}_{-0.1}$	$1.8^{+0.2}_{-0.1}$
BP Tau	$0.5^{+0.1}_{-0.1}$	$2.0^{+0.2}_{-0.0}$	$1.1^{+0.1}_{-0.2}$
DE Tau	$0.8^{+0.3}_{-0.3}$	$4.5^{+0.5}_{-0.4}$	$0.3^{+0.1}_{-0.2}$
DF Tau	$0.3^{+0.3}_{-0.3}$	$4.3^{+1.2}_{-0.8}$	$0.1^{+0.2}_{-0.1}$
DM Tau	$1.5^{+0.4}_{-0.4}$	$3.8^{+0.4}_{-0.3}$	$0.9^{+0.3}_{-0.2}$
DR Tau	$0.9^{+0.5}_{-0.4}$	$3.1^{+0.9}_{-0.7}$	$0.9^{+0.5}_{-0.4}$
GM Aur	$1.4^{+0.2}_{-0.2}$	$3.4^{+0.2}_{-0.2}$	$1.1^{+0.2}_{-0.1}$
HN Tau	$1.0^{+0.1}_{-0.1}$	$2.3^{+0.1}_{-0.1}$	$1.7^{+0.2}_{-0.1}$
LkCa15	$1.3^{+0.7}_{-0.6}$	$4.7^{+0.5}_{-0.5}$	$0.4^{+0.2}_{-0.2}$
RECX-11	$0.7^{+0.3}_{-0.3}$	$4.3^{+0.5}_{-0.4}$	$0.3^{+0.1}_{-0.2}$
RECX-15	$0.2^{+0.7}_{-0.2}$	$5.2^{+0.8}_{-1.5}$	$0.0^{+0.2}_{-0.0}$
RU Lupi	$1.1^{+0.3}_{-0.3}$	$3.7^{+0.3}_{-0.3}$	$0.7^{+0.2}_{-0.2}$
SU Aur	$1.1^{+0.5}_{-0.4}$	$4.0^{+0.6}_{-0.5}$	$0.6^{+0.3}_{-0.3}$
TW Hya	$2.0^{+0.0}_{-1.6}$	$6.0^{+0.0}_{-0.2}$	$0.0^{+0.1}_{-0.0}$
UX Tau	$0.5^{+0.1}_{-0.1}$	$2.1^{+0.2}_{-0.1}$	$1.0^{+0.2}_{-0.1}$
V4046 Sgr	$2.0^{+0.0}_{-2.0}$	$6.0^{+0.0}_{-0.2}$	$0.0^{+0.1}_{-0.0}$

[a]Best-fit $A_V(H_2)$ values from my extinction curve modeling assuming $R_V = 3.1$

Table 4.3. A_V Comparison For Best-Fit Targets

Object	$A_V(H_2)$ (this chapter)	McJunkin et al. (2014) $A_V(N(HI))$	Furlan et al. (2011) $A_V(IR)$	$A_V(SED)$	$A_V(X\text{-ray})$
AA Tau	$1.3^{+0.1}_{-0.1}$	0.34	1.95	0.40[a]	6.07[d]
BP Tau	$0.5^{+0.1}_{-0.1}$	0.17	1.06	0.45[a]	0.58[d]
DE Tau	$0.8^{+0.3}_{-0.3}$	0.31	0.89	0.35[a]	
DF Tau	$0.3^{+0.3}_{-0.3}$	0.54	1.95	0.10[a]	
GM Aur	$1.4^{+0.2}_{-0.2}$	0.51	0.57	0.30[a]	2.97[e]
HN Tau	$1.0^{+0.1}_{-0.1}$	0.36	1.06	1.15[a]	1.29[d]
LkCa15	$1.3^{+0.7}_{-0.6}$	0.31	1.06	0.30[a]	2.39[f]
RECX-11	$0.7^{+0.3}_{-0.3}$	0.03		0.0[b]	0.04[g]
RU Lupi	$1.1^{+0.3}_{-0.3}$	0.07		0.25[c]	1.16[h]
UX Tau	$0.5^{+0.1}_{-0.1}$	0.51	0.46		0.39[e]

[a]Herczeg & Hillenbrand (2014)

[b]Testa et al. (2008)

[c]DAO STIS G430L analyzed in McJunkin et al. (2014)

[d]Güdel et al. (2007a)

[e]X-ray data analyzed in McJunkin et al. (2014)

[f]Skinner & Güdel (2013)

[g]López-Santiago et al. (2010)

[h]Robrade & Schmitt (2007)

visual extinctions assuming standard interstellar gas-to-dust ratios. Herczeg & Hillenbrand (2014) obtain visual extinction values using weak-line T Tauri star photospheric templates and an accretion continuum fit to broadband optical spectra. The X-ray extinction method uses two-temperature fits to CCD resolution ($R \sim 15 - 20$) spectra to obtain H I column densities, which are converted to A_V(X-ray) values similar to the previous chapter. The $A_V(H_2)$ values derived in this chapter for AA Tau, GM Aur, and RECX-11 are inconsistent with all previous literature values, while the other targets are inconsistent with some literature values and consistent with others.

V4046 Sgr and TW Hya have A_V values that are consistent with the low A_V expected from previous studies (e.g., 0.04 mag (McJunkin et al. 2014) and 0.19 mag (Argiroffi et al. 2012) for V4046, and 0.04 mag (McJunkin et al. 2014) and 0.13 mag (Stelzer & Schmitt 2004) for TW Hya) and their relative proximity to the Sun, though with their large error bars, I do not constrain the A_V values of the two targets. V4046 Sgr and TW Hya are nearby stars with distances of 73 pc (Torres et al. 2008) and 54 pc (van Leeuwen 2007) respectively. Bohlin et al. (1978) find that stars with distances less than 100 pc have color excesses $E(B - V) \ll 0.1$ mag, or $A_V \ll 0.3$ mag assuming $R_V = 3.1$.

BP Tau and DE Tau have very similar H_2 column densities and temperatures, but quite different A_V and R_V values. This difference is driven by the observed flux ratios between the higher and lower wavelength lines. The ratio of the higher wavelength lines to the lower wavelength lines of BP Tau is larger than that of DE Tau. The ratio also starts increasing at a larger wavelength in BP Tau (1400 Å) than DE Tau (1300 Å), leading to different extinction curve shapes. DE Tau has a much shallower turnoff at lower wavelengths than BP Tau. This can be described in two different ways, as A_V and R_V are not independent in creating an extinction curve. The shallower curve of DE Tau can be described by a larger R_V value indicative of grey extinction, or a smaller A_V value. For better comparison with previous literature extinction values, I performed a second extinction curve fit in which I set $R_V = 3.1$ and only let the A_V value vary. The results are listed in the far right column of

Table 4.2. Some targets, such as RECX-11, TW Hya, and V4046 Sgr have best-fit extinctions consistent with previous literature values with the new fit, though others such as AA Tau, BP Tau, and HN Tau have best-fit values more inconsistent with literature values than the previous fit.

RECX-11 and RECX-15 are quoted in the literature as having zero extinction from measurements of optical colors (Luhman & Steeghs 2004). I find that RECX-15 is consistent with zero extinction ($A_V(H_2) = 0.2^{+0.7}_{-0.2}$ mag), but RECX-11 is not ($A_V(H_2) = 0.7^{+0.3}_{-0.3}$ mag). RECX-15 has a bit of scatter in the data-to-model H_2 line fluxes at short wavelengths, similar to V4046 Sgr and TW Hya, so that even though the fit finds an extinction of 0.2 mag, $A_V(H_2)$ = 0 mag (a horizontal line) also fits the data. RECX-11 has a noticeable turnoff in the data at shorter wavelengths and is not well-fit by an $A_V(H_2) = 0$ mag curve. Inclination and disk flaring could play a role in this discrepancy between the two η Cha stars as the fluorescing H_2 is primarily in the upper atmosphere of the disk. However, Lawson et al. (2004) find inclinations of 70° and 60° for RECX-11 and RECX-15, respectively. The stars have little difference in published inclination, though these inclinations are derived from $H\alpha$ profile fits, which are less accurate than inclinations for other targets in the literature (described in the last chapter: e.g., McJunkin et al. 2014).

4.5.3.   Predicted 2175 Å NUV Bump

I plot six targets with their best-fit extinction curves in Figure 4.6. Most of the errors on the points are too small to see in the figure. The extinction curves are extended to longer wavelengths in order to see the predicted 2175 Å bump, which is very pronounced for some targets. The size of the bump changes with the different $A_V(H_2)$ and R_V values. However, the predicted 2175 Å bump is not very pronounced in DM Tau or LkCa15. For these targets as well as others in the sample, the weak 2175 Å bump is similar to the anomalous extinction laws of HD 229647 and HD 283809 in Calvet et al. (2004). Converting these

extinction curves into transmission curves, I can predict the visibility of the 2175 Å bump for NUV observations. The process is shown in Figure 4.7. I make a linear fit to the UV "background" as in Fitzpatrick & Massa (1990), and directly measure the difference between the UV background and the transmission curve at 2175 Å to calculate the amount of absorption predicted against the linear fit. Defining a 10% absorption against the UV fit as the observation limit, I predict that all of the targets with good extinction fits would have noticeable 2175 Å bumps. Future work with NUV data for these sources can further test this prediction and help constrain the validity of these extinction curves.

4.6. Discussion

While the majority of the targets are uncontaminated sources, a few have been shown to have strong outflows that may affect the H_2 line profiles. Using COS observations, France et al. (2012b) find that DF Tau, HN Tau, LkCa 15, RECX-15, and RU Lup have H_2 emission with extended blue wings, possibly indicating origin in an outflow component. However, LkCa 15 and RU Lup had weaker extended emission and were adequately fit with a single Gaussian emission line, implying a disk origin. Using STIS spectra, Herczeg et al. (2005, 2006) find that all of the H_2 fluorescence of RU Lup is contained in outflows. The difference between the COS and STIS data is puzzling, possibly indicating a time-dependent outflow or geometrical changes between observations (France et al. 2012b).

In my model fits, I assume a single H_2 column density and temperature for all progressions. This simplification works for the majority of my progressions, though I do see that for some of my targets the (4,4) progression is not well-fit by the best-fit model. This progression may absorb at a different location in the disk, better described by a separate temperature and column density, or may be the result of non-thermal excitation processes (e.g., France et al. 2012a). In the future, modifying the model to include a different column density and temperature value for each progression may lead to better line fits and a better
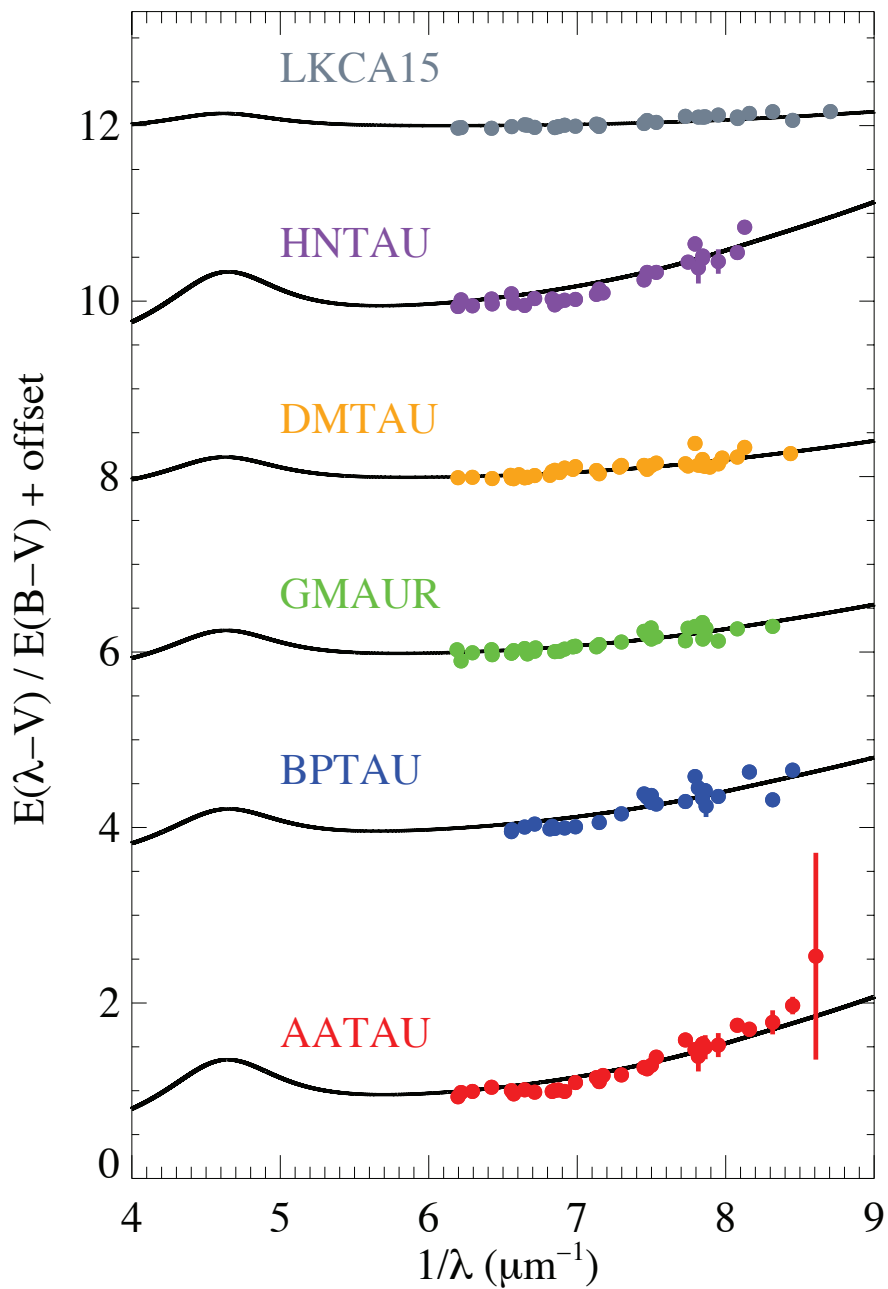
Fig. 4.6.— Extinction curves for 6 targets with noticeable extinction compared to their best-fit Cardelli et al. (1989) extinction curve. I can predict the strength of the 2175 Å bump feature by extending the extinction fits to longer wavelengths. All of these targets predict noticeable dips in the transmission curve against the linear UV "continuum" fit, which I hope to detect in future observations.
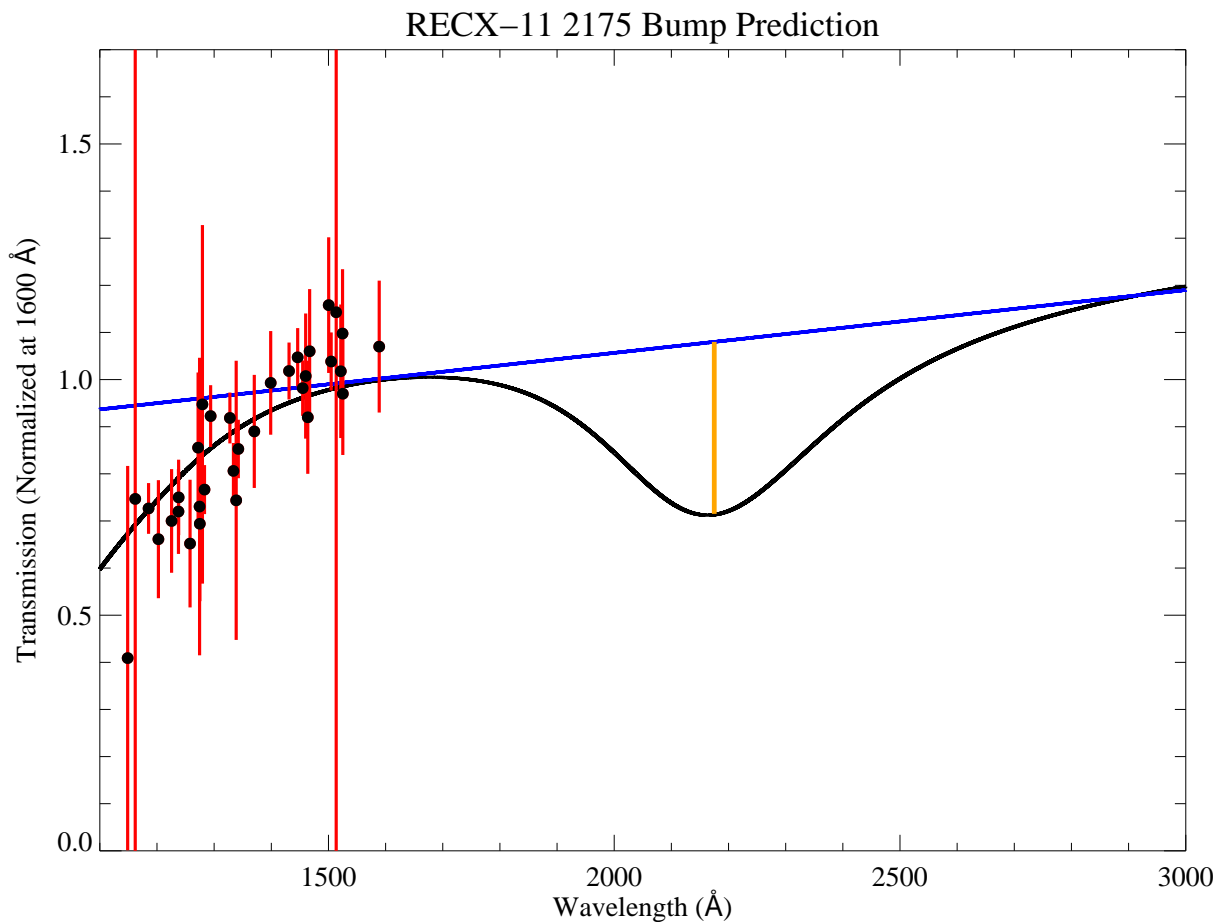
Fig. 4.7.— Plot of the 2175 Å bump strength calculation. My transmission curve (normalized at 1600 Å and extended out to 3000 Å) for RECX-11 is in black, with the measured observed/predicted line fluxes with errors overplotted at the shorter wavelengths. A linear fit to the UV "background" for wavelengths greater than 1500 Å is shown in blue. The predicted absorption is the difference between the linear fit and the transmission curve at the central wavelength of the bump, and is indicated by the orange line.

understanding of the fluorescence location of each progression.

Little agreement exists between previous extinction studies in the literature over different wavelength ranges, and the $A_V(H_2)$ values found in this chapter are also quite disparate from the optical, H I, IR, and X-ray (see Table 4.3). While all these methods traverse the same path through the interstellar medium, they likely travel different paths through the circumstellar medium. These different paths sample different areas of the disk, so it is not particularly surprising that the extinctions derived from different wavelength bands do not agree. Many of these CTTSs are also variable, which may be caused by varying circumstellar obscuration (Herbst et al. 1994). Alencar et al. (2010) saw very prevalent variability in lightcurves of CTTSs in NGC 2264 with CoRoT, possibly due to variable disk extinction from an inner disk warp. This variable disk extinction could be contributing to the different A_V values found in the literature for the targets.

The $A_V(H_2)$ values I obtain in this chapter are generally higher than the $A_V(N(H\ I))$ values found in the previous chapter using interstellar H I absorption against the Lyα line. The H_2 method contains circumstellar extinction, whereas the H I method does not, most likely contributing significantly to the A_V difference. Many of the targets with higher $A_V(H_2)$ values have R_V values that differ from the typical interstellar value of 3.1, which is assumed in the calculation of the extinction in the last chapter. Changing the R_V value of the extinction curve directly affects the $A_V(H_2)$ value found for the extinction fit, possibly contributing to the A_V differences between the two studies. R_V and A_V are strongly correlated, as increasing the A_V value or decreasing the R_V value both lead to faster, deeper falloffs of the extinction curve at shorter wavelengths. Similar extinction curves are created by the (A_V, R_V) pairs of (0.5,2.2), (1.0,3.1), and (1.5,4.0). These three curves are plotted in Figure 4.8. This degeneracy can be broken by assuming a value for either A_V or R_V that is physically motivated or based on previous measurements, which I do by setting $R_V = 3.1$ in Section 4.5.2. Requiring A_V or R_V to be calculated independently seems to be a limitation of my new technique, which I hope to improve upon in future iterations. Using the calculated A_V

values, the predicted transmission at 1400 Å differs between this chapter and the previous chapter by $\lesssim 0.15$ for most targets. This is about the average size of the error bars on the extinction curve points in this chapter (see Figure 4.5a-4.5b). The outliers are AA Tau, BP Tau, and LkCa 15. Thus, the predicted extinctions are not vastly different for most targets even though the A_V values differ because the R_V value is allowed to change.

R_V values greater than the canonical interstellar value of 3.1 indicate a dust grain population with relatively more larger grains and fewer smaller grains (Draine 2003) . Conversely, R_V values less than 3.1 may indicate a dust grain population with more smaller grains and fewer larger grains. An enhanced small-grain population, seen in some of the targets with $R_V < 3.1$, is the opposite of what one would expect if grain growth was occurring in the star-forming region. I directly probe the upper layers of the disk with the H_2 fluorescence, so the larger grains may be settling toward the disk midplane faster than smaller grains, artificially increasing the fraction of small grains to large grains. Turbulence in the disk could also be breaking up larger grains and resupplying the population of small grains (Birnstiel et al. 2012b).

This apparent grain evolution could also result in non-LTE H_2 level populations as grain photoelectric heating becomes less efficient, dropping the gas temperature at the disk surface (Nomura et al. 2007). France et al. (2012a) also find evidence for non-thermal H_2 level populations in AA Tau at high excitation temperatures. They find an increased population at high-J levels (excitation temperatures $> 2 \times 10^4$ K), suggesting that non-equilibrium photoexcitation processes or H_2 formation on grain surfaces may be occurring in the disk. If the H_2 lines are not in LTE, the fluorescent line ratios may be modified, possibly producing anomalous R_V values.
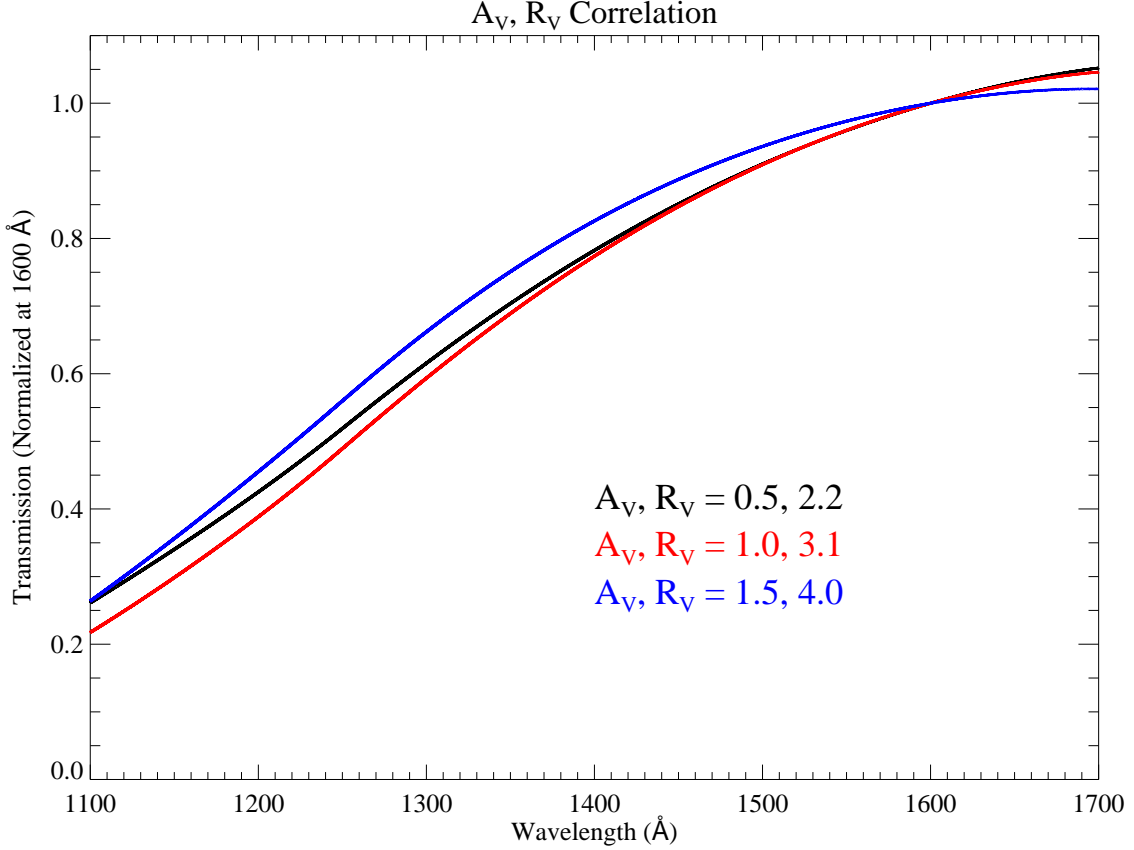
Fig. 4.8.— Three extinction curves for different (A_V, R_V) value pairs. The black line is (0.5,2.2), the red line is (1.0,3.1), and the blue line is (1.5,4.0). A_V and R_V are strongly correlated, so that a unique (A_V, R_V) extinction curve is difficult to determine without having a good estimate of either value. I present A_V values assuming a typical $R_V = 3.1$ value in Table 4.2 in order to break the degeneracy and for better comparison with the literature, which often assumes this R_V value in extinction calculations.

I calculate the total dust-to-gas ratio along the line of sight using my best-fit $A_V(\mathrm{H_2})$ and $N(\mathrm{H_2})$ values from this chapter and the H I column densities from the previous chapter. Using $N_{H,tot} = N(HI) + 2N(H_2)$, I find $A_V(\mathrm{H_2})/N_{H,tot}$ ratios ranging from 0.5 to 25 times the canonical ISM value of $A_V/N_H = 5.3 \times 10^{-22}$ mag cm^{-2} H^{-1} (Bohlin et al. 1978; Savage & Mathis 1979). A moderate amount of turbulence ($10^{-3} < \alpha_t < 10^{-2}$) could explain the larger

dust-to-gas ratios. The turbulence could provide significant radial drift velocities to enrich the inner disk in dust, as well as provide a means to replenish the small grain population through collisions (Birnstiel et al. 2012b).

4.7. Conclusions

I find the best-fit UV extinction curve toward 16 protostars with circumstellar disks, correcting for molecular self-absorption in the disk, using a new H_2 fluorescence technique. Some targets are not well-fit by a typical interstellar extinction curve, suggesting grain processing occurring in the circumstellar environment, or non-thermal H_2 level populations. I predict the strength of the 2175 Å bump for the targets by extending the best-fit extinction curves out to longer wavelengths. Future NUV data can test this prediction and better constrain these extinction curves. H_2 column densities and temperatures are measured for these disks, which are generally consistent with previous H_2 line studies. I calculate $A_V(H_2)$ values higher than in the previous chapter based on H I column densities (McJunkin et al. 2014), and little agreement with A_V values derived from optical and infrared measurements, which are themselves fairly disparate from each other. The methods likely probe different paths through the circumstellar material. My fits generally do not find $R_V = 3.1$, meaning comparisons to the literature values which assume $R_V = 3.1$ may not be valid. I perform a second fit setting $R_V = 3.1$ and find A_V values that are more consistent for some targets and more inconsistent for others. This chapter is exploratory in developing a new technique, and part of that exploration is trying to figure out the limitations. One limitation is that my new technique likely needs A_V or R_V calculated independently to constrain the other due to A_V and R_V being so highly degenerate. In future work, I hope to improve on the limitations of this new method and make it more robust.

5. Conclusions

"...there ain't no journey what don't change you some."

- David Mitchell, *Cloud Atlas*

5.1. The limits of HST CO absorption measurements

I have presented new observations and models of Fourth Positive band CO absorption lines in the disks of DE Tau, RECX-15, RW Aur, and SU Aur, tripling the number of measurements in the literature. I also re-analyzed previous CO absorption in the disks of AA Tau and HN Tau with my new method for consistency. Good agreement in temperature is found with previous UV CO fluorescence studies, though my temperatures are cooler than IR CO emission temperatures and warmer than IR CO absorption temperatures. It may be that my UV observations are probing a disk region in-between the IR observations.

However, this is at the limit of what can be done with current HST instrumentation. For better fits, higher spectral resolution is necessary in order to resolve the high-J lines which help to constrain the CO temperature at the high end. HST-STIS observations using the E140M mode are not feasible to obtain new observations due to the low flux levels ($\sim 10^{-15}$ ergs cm^{-2} s^{-1} Å^{-1}) in the 1300 - 1600Å wavelength range.

5.2. The difficulties of extinction measurements

I calculated extinction values from interstellar H I column densities derived from absorption against the stellar Lyα line of 31 young stars, as well as extinction values using an H$_2$ fluorescence model for a subset of the 31 targets. Optical, IR, and X-ray extinction

values in the literature do not agree well with each other, providing many different extinction values for each target. My Lyα values were generally lower than the optical, IR, and X-ray measurement techniques. The H_2 fluorescence A_V values had more of a spread, but also do not agree well with any of the other wavelength extinction techniques. This makes it very difficult to choose an extinction value for astrophysical calculations, such as correcting the observed CTTS SED to derive the intrinsic fluorescence incident on the planet-forming region of the circumstellar disk.

The extinctions may vary due to the different wavelengths probing different material along the line of sight, or because the different spectral regions may be probing different circumstellar lines of sight entirely. My Lyα measurements provide well-determined N(H I) column densities, which are easily converted into a visual extinction, but the optical and X-ray values may also be probing extra molecular and ionized gas along the line of sight. Each observed wavelength can also be produced in different regions around the star and disk, leading to different paths through the circumstellar material and different amounts of measured extinction. Lastly, many of these CTTSs show variability, possibly caused by varying circumstellar obscuration, which could lead to variance in the measured A_V values. The A_V discrepancies may just be due to the spatial complexity of the young star and disk system, with each extinction measurement probing a different circumstellar extinction, that when removed, would provide a clean interstellar extinction curve.

5.3. Evidence of grain processing/non-thermal H_2 populations in CTTS disks

I empirically estimated far-UV extinction curves for 16 CTTSs using an H_2 fluorescence model which corrected for self-absorption along the line of sight. By comparing the observed H_2 line fluxes with the predicted flux produced by pumping a ground state H_2 population with the stellar Lyα profile, I determined the amount of circumstellar and interstellar attenuation. Some curves were not well fit by a typical ISM extinction curve, which suggested a strong

circumstellar component to the extinction, and that there may be grain processing occurring in the disk, or that the H_2 population in the disk is non-thermal.

When grain growth occurs in a PPD, the distribution of grain sizes changes, with a greater ratio of larger grains to smaller grains. Grain processing may occur such that the extinction curve of the circumstellar material cannot be described by the A_V-R_V curves we fit to the data, which typically describe interstellar material. In this case, the total extinction curve (circumstellar + interstellar) would also be non-interstellar, which we observe for some targets. If the H_2 in the PPD has a non-thermal population, the fluorescence observed when pumped by the Lyα profile of the protostar will be much different than predicted by my model, which assumes a thermal population with a single column density and temperature. My code has the ability to input any initial H_2 population, which in future iterations can help determine if a non-thermal H_2 population can accurately describe the observations.

6.   Future Work

"Our lives are not our own. We are bound to others, past and present, and by each crime and every kindness, we birth our future."

- David Mitchell, *Cloud Atlas*

6.1.   Updating the H$_2$ fluorescence code

To continue this work, I plan on updating my H$_2$ fluorescence code and running it with new parameters. The first major change I want to make to the code is to add in the fluorescence of non-thermal H$_2$ populations. While a theoretical argument has been made for thermal populations of H$_2$ (Ádámkovics et al. 2016), there is ample evidence supporting non-thermal populations as well, including the fits I obtain in Chapter 4 that are not well fit by a Cardelli et al. (1989) curve. Herczeg et al. (2002) initially found evidence for a non-thermal component of the H$_2$ population in CTTSs by observing H$_2$ emission from TW Hya. France et al. (2011a) later suggested that both CO and H$_2$ could have relevant, non-thermal emission populations in the inner disk of CTTSs. Further evidence of a non-thermal H$_2$ absorption population in AA Tau, possibly due to excitation by continuum photons and excess energy from H$_2$ formation on dust grains, was found by France et al. (2012a). Fluorescing non-thermal H$_2$ populations would help to test whether this is a contributing factor behind the non-interstellar extinction curves I find in this thesis. The code already accepts arbitrary H$_2$ populations, which can then be excited by the Lyα profiles to produce new fluorescent lines. By testing different non-thermal H$_2$ populations and searching for populations that produce curves that are more similar to Cardelli et al. (1989) models, I can test the degree to which non-thermal H$_2$ populations are relevant for the targets.

New pumping profiles should be read in as well if new reconstructed Lyα profiles are made in the future. I would like profiles that take into account a more physical filling fraction, as well as a better treatment of radiative transfer. Also, I plan on updating the fluorescence code to fit each of the seven progressions with a different column density and temperature. The (4,4) progression especially was poorly fit in relation to the other progressions, which may mean that the H$_2$ emitting the (4,4) progression is not co-spatial with the rest of the fluorescing H$_2$, or that it is not populated thermally. By letting all the progressions have different column densities and temperatures, I will obtain better flux fits and can look for trends in the best-fit values of the progressions.

6.2. The 2175 Å bump

I predict the strength of the 2175 Å bump by extending my extinction fits out to longer wavelengths in Chapter 4 of this thesis. To do this, I modeled the UV "background" with a linear fit and measured the predicted absorption against the background. A 10% absorption against the background is taken as the detection limit. All of the targets with good fits ($0.75 \leq \chi^2 \leq 1.25$) have predicted noticeable bumps. Though I showed in Figure 4.8 that A$_V$ and R$_V$ are strongly degenerate, with multiple combinations providing similar curves in the $1100-1700$ Å region, Figure 6.1 shows that when extended out to the 2175 Å region, the bump strength predicted is noticeably different. This measurement can therefore help break the degeneracy between A$_V$ and R$_V$ in my new technique. The predicted strength can be tested by taking future NUV data and measuring the dip in the flux at 2175 Å. Measuring the absorption percentage provides a constraint on the extinction fits at shorter wavelengths and helps to alleviate a limitation of my technique.
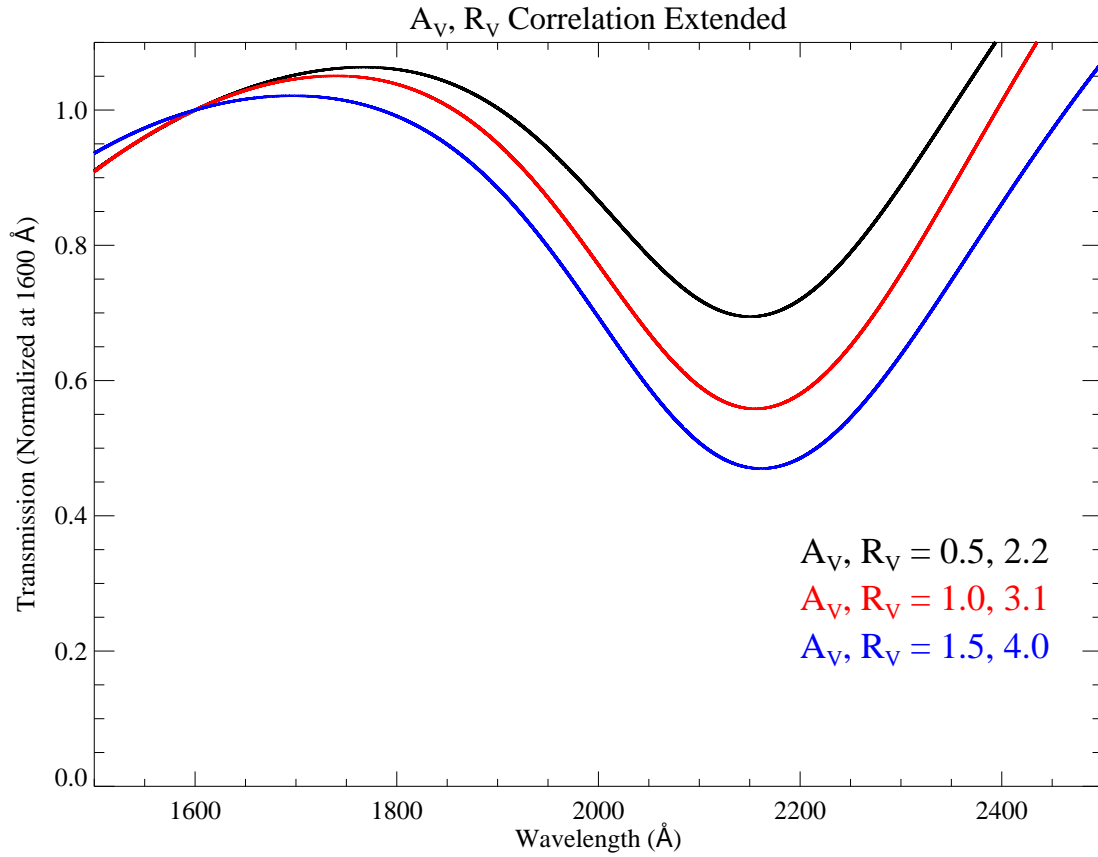
Fig. 6.1.— Figure 4.8 extended out to the 2175 Å bump, showing that the A_V and R_V which give similar 1100 - 1700 Å extinction curves predict different 2175 Å bump strengths. This can help break the degeneracy between the two values and better constrain the extinction fits at lower wavelengths.

6.3.   Extinction Towards Early-Type Stars In Local Star-Forming Regions

I presented in this thesis a new technique for determining the extinction curves toward young CTTSs, though how well this technique is working due to the limitations discovered is up for debate. Since I used my new method on all the viable stars in my sample (those that had reconstructed Lyα profiles), I want to follow up my work by using a more traditional and tested technique to accurately measure more UV extinction curves toward stars in local molecular clouds and star-forming environments using new FUV and NUV data taken with STIS. This will expand the number of targets with derived UV extinction curves as well as look for trends in the extinction curves toward different star-forming regions.

There are two main techniques that have been employed for deriving extinction curves: the pair method and comparison with model atmospheres. The pair method involves a comparison between the flux of a reddened star and an unreddened star of the same spectral type (Rudnick 1936). The problem with this technique is that there are very few truly unreddedned standard stars for comparison (Fitzpatrick & Massa 2005). The model atmosphere method involves a comparison between the flux of a reddened star and the output of a stellar atmosphere model. This approach is advantageous because, in theory, the model can be tweaked to match any stellar spectral type for comparison, eliminating the need to find a standard, unreddened pair star.

To measure the UV portion of the extinction law, stars with appreciable flux in the UV bandpass are needed. This limits me to O-, B-, and early A-type stars. I will propose to study 9 B- and A-type stars (listed in Table 6.1) identified in Mooley et al. (2013) or Alecian et al. (2013) as stars with probable locations in local dense clouds and star-forming regions (Taurus-Auriga, Orion, Upper Scorpius, Cepheus, 2 Cyg, and the Vela star cloud). Using stars in multiple regions is ideal for determining if there is a "universal" UV extinction law for star-forming environments, and for identifying common trends in the grain distributions at sites of active star formation. The sightlines toward these stars are dominated by dust in the star-formation region (Reipurth & Schneider 2008; Lombardi et al. 2008, 2010, 2011)

such that the derived extinction curve will not be contaminated by intervening average ISM dust. The sample consists of well-studied early type stars with accurate spectral types and visual extinctions from broadband optical colors, covering a range of star-forming regions, distances, and extinction values.

I hope to obtain FUV and NUV spectra of the 9 targets with STIS for the first time. The advantages of using STIS data over previous IUE data are the smaller aperture size of STIS, the larger signal-to-noise (S/N), and the more accurate flux calibration. The small STIS apertures will reduce the amount of scattered light in the spectra by $\sim 10^4$ (when comparing a target centered on the STIS grating aperture to the IUE large aperture) so that I obtain an accurate measure of the stellar spectrum. The IUE flux calibration is accurate to $\sim 10\%$ (Massa & Fitzpatrick 2000), whereas the STIS flux calibration is accurate to $\sim 3\%$ (Bohlin 1998), which will reduce the errors on the derived extinction curve. These data will complement the UV spectra in the IUE Spectral Atlas and can be used for a larger comparison survey of the extinction curves in star-forming regions.

I plan to calculate the extinction curves along several lines of sight toward local molecular clouds and star-forming regions by comparing the observed stellar spectra to unreddened model stellar spectra. This comparison provides a direct measurement of the extinction curve and is well-characterized for the diffuse ISM. The dominant source of error in this method is the determination of spectral type of the target star. I will rely on accurate spectral types so that the observations are compared to the correct stellar model spectra. Typical errors on the quoted spectral types in Table 6.1 are one spectral subtype for the B stars and two for the A stars (Vieira et al. 2003). In Figure 6.2, I demonstrate the different extinction curves that would be calculated for HD 26571, a B7III star previously observed with IUE, if different spectral types were adopted. When measuring the extinction at 2175 Å, changing from a B7 model spectrum to a B8 model spectrum changes the derived extinction from 4.35 mag to 4.72 mag (a 0.37 mag difference). Changing by one spectral subtype in the other direction decreases the derived extinction by 0.43 mag. The shape of

Table 6.1.   Target Parameters

Target	Distance (pc)	Spectral Type	A_V	Region	Refs.[a]
BD+41 3731	980^{+500}_{-200}	B2	1.06	2 Cyg & NGC 6910	1,2,3,4
HD 27659	164^{+10}_{-10}	A3V	1.50	Taurus	5,6
HD 37357	375^{+30}_{-30}	A1V	0.37	Orion OB1c	1,4,7
HD 68695	570^{+100}_{-100}	A0V	0.49	Vela star cloud	1,4,8
HD 290500	375^{+30}_{-30}	A2	1.26	Orion OB1	1,4,7
HD 290770	375^{+30}_{-30}	B9	0.61	Orion OB1 belt	1,4,7
SV Cep	400^{+100}_{-100}	A0	1.87	Dark Cep cloud L123	1,9
V1409 Ori	375^{+30}_{-30}	A1V	0.96	λ Orionis	1,4,7
V2307 Oph	145^{+20}_{-20}	A0V	2.47	Upper Scorpius	1,4,10

[a] (1) Alecian et al. (2013); (2) Finkenzeller (1985); (3) Shevchenko et al. (1991); (4) Vieira et al. (2003); (5) Mooley et al. (2013); (6) Rebull et al. (2010); (7) Brown et al. (1994); (8) Eggen (1986); (9) Kun (1998); (10) Preibisch & Mamajek (2008)

the extinction curve also changes, with the slope of the far-UV rise increasing slightly for earlier spectral types. This systematic error will need to be taken into account in the error analysis.

I will compare the UV SED of the targets with the Castelli & Kurucz (2004) ATLAS9 unreddened model stellar spectra of the same spectral type. By finding the flux ratio between the ATLAS9 stellar model and the new UV STIS data, I can obtain extinction curves over a wide wavelength range. I will then fit the resulting extinction curve with Cardelli et al. (1989) models as I do in Chapter 4 of this thesis. I hope to determine the extinction curve as a function of environment and find common trends or significant differences.

6.4. Exploring the Outflow Component

In Chapter 3 of this thesis, I measure the visual extinction toward young stars by modeling the H I absorption against the stellar Lyα profile. However, I only fit the redward side of the profile due to the blueward side often being contaminated by absorption from an outflow component (Schindhelm et al. 2012b). In future work, I plan to explore the properties of this outflow component, possibly by updating my model to look at both the redward and blueward side of the Lyα profile.

Outflows in lower-mass stars (~ 1 M$_\odot$) are generally understood to be driven by magnetic fields, though a consensus as to whether the driving is by centrifugal acceleration (Blandford & Payne 1982; Pudritz & Norman 1986; Pelletier & Pudritz 1992) or toroidal magnetic field pressure (Lynden-Bell 1996, 2003) has not been reached. Outflows act as an important mechanism through which protostars may lose excess angular momentum, and as such, are closely linked to the protostellar accretion. The shape and velocity structure of an outflow can tell us about the stellar mass accretion history. Outflows are also important in the self-regulation of star formation in dense clouds by injecting energy and momentum into the surrounding material. Understanding the composition and energetics of outflows
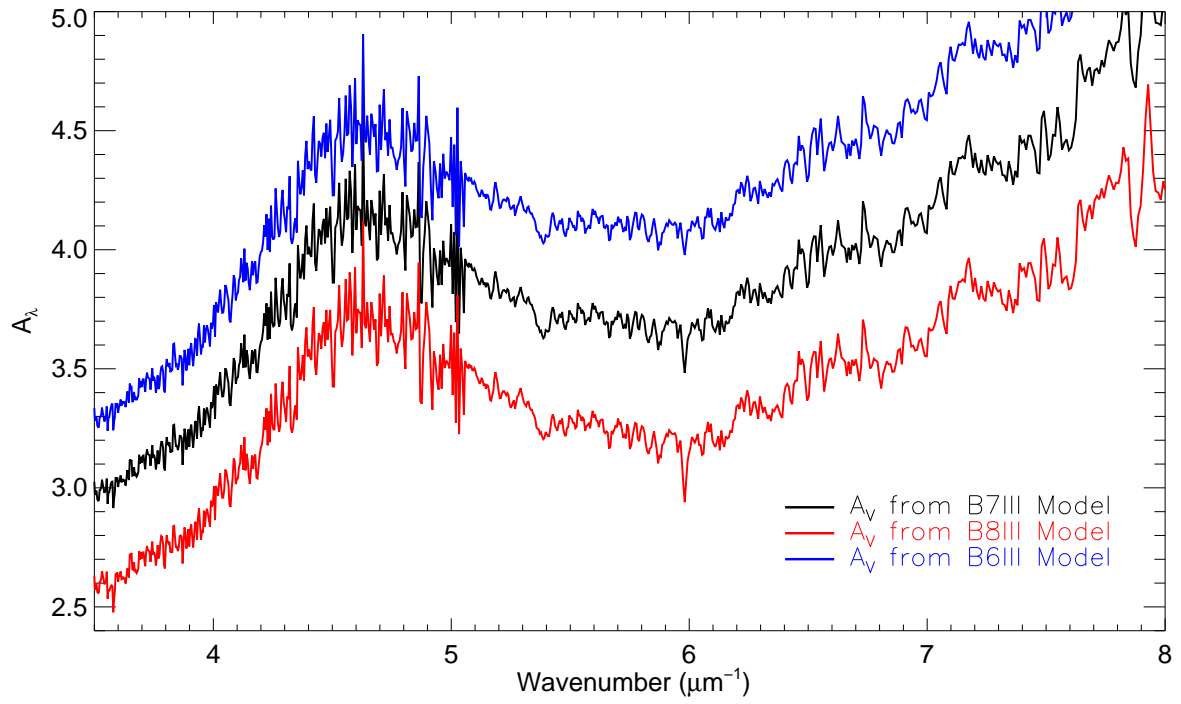
Fig. 6.2.— The different extinction curves calculated for HD 26571, a B7III star, for changes of one spectral subtype in either direction.

can tell us about the protostar itself as well as the circumstellar environment in which it is embedded.

Though Figure 3.3 seems to show that RECX-15 has no blueward Lyα emission, a closer look reveals this not to be the case. In Figure 6.3, I show a plot of the Lyα profile of RECX-15 with the airglow emission removed. The plot shows the strong redward emission at positive velocities (away from us) that is fit in Chapter 3, but also reveals a weak, but still present, non-zero blueward emission extending out to ~ 800 km s^{-1}. The absorber in the outflow must be fairly optically thick and at high velocities in order to block out most of this broad, blueward Lyα emission, but the fact that not all of the flux is removed may indicate that the absorber is not distributed uniformly in the outflow. It is possible that the outflow absorber is clumpy in nature and thus has a filling fraction $\eta < 1$. This is an interesting phenomenon that I plan to look into further, either by updating my H I absorption model to include an outflow component, or by creating a new model focused on the blueward side of the Lyα line.

6.5. Gas and dust disk evolution

This thesis has focused on a single snapshot of the gas and dust disk inventory, though the gas and dust populations in a disk evolve as terrestrial and gas planets start forming (see Chapter 1.1.1). As planetesimals are forming early in the disk lifetime, the grain growth will change the size distribution of the dust particles. Later, when the planetesimals have grown large enough to capture the gas in their region of the disk, the gas population will evolve as gas leaves the disk and becomes the atmospheres of gas giant planets. Gaps may open up in the disk, altering the initially smooth distribution of gas and particles. The gas population also changes due to photoevaporation and excitation from energetic stellar photons. I plan to assess the evolution of the gas and dust environment as different stages of planet formation are occurring by studying stars in different star-forming regions of different ages.
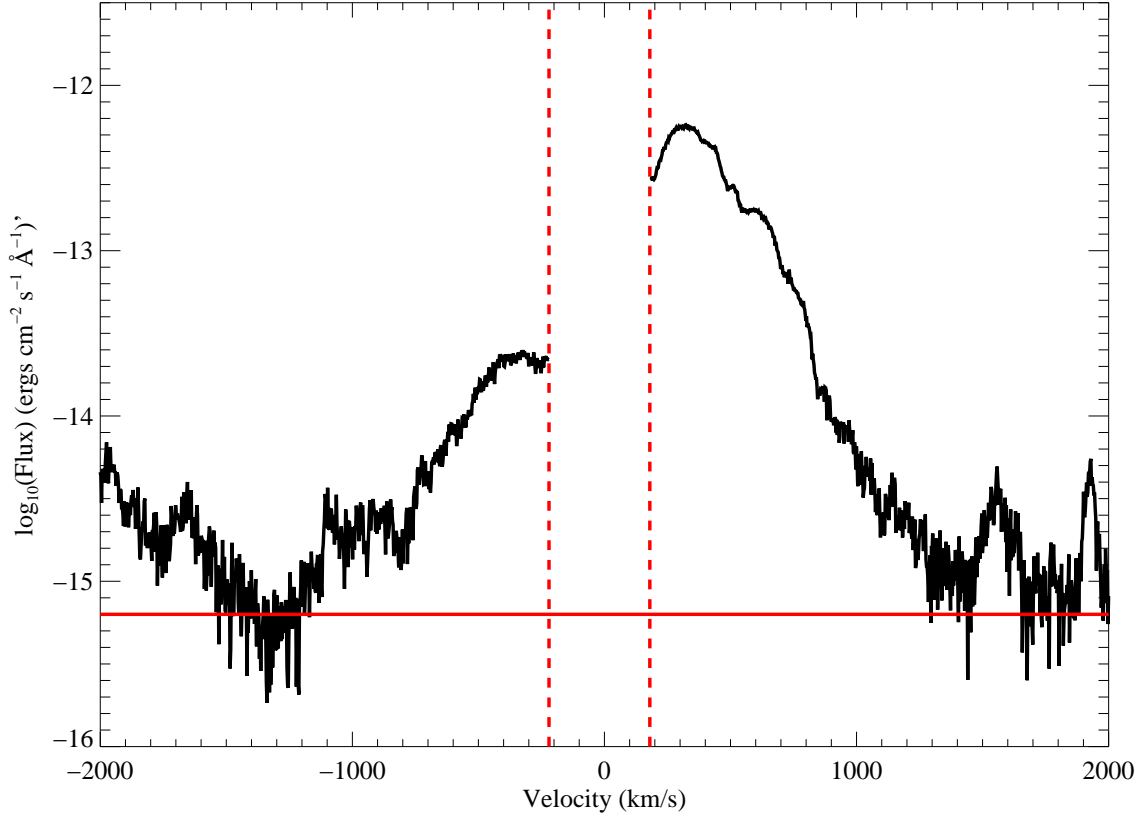
Fig. 6.3.— The Lyα profile of RECX-15 plotted in log(flux) versus velocity. The airglow emission at the center of the line has been removed, which is indicated by the red dashed lines. The flux continuum level is shown by the solid red line. In Chapter 3, the blueward side of the RECX-15 Lyα line was assumed to be completely absorbed by an outflow. In log space, however, a small amount of blueward emission is shown to be present. This could indicate a high-velocity, optically thick absorber which absorbs most of the flux, but allows a small fraction through due to a clumpy distribution with a filling fraction $\eta < 1$.

7. Bibliography

REFERENCES

Abgrall, H., Roueff, E., Launay, F., Roncin, J. Y., & Subtil, J. L. 1993a, A&AS, 101, 273

—. 1993b, A&AS, 101, 323

Acke, B., van den Ancker, M. E., & Dullemond, C. P. 2005, A&A, 436, 209

Ádámkovics, M., Najita, J. R., & Glassgold, A. E. 2016, ApJ, 817, 82

Aikawa, Y. & Herbst, E. 1999, A&A, 351, 233

Akeson, R. L., Ciardi, D. R., van Belle, G. T., & Creech-Eakman, M. J. 2002, ApJ, 566, 1124

Alecian, E., Wade, G. A., Catala, C., Grunhut, J. H., Landstreet, J. D., Bagnulo, S., Böhm, T., Folsom, C. P., Marsden, S., & Waite, I. 2013, MNRAS, 429, 1001

Alencar, S. H. P. & Basri, G. 2000, AJ, 119, 1881

Alencar, S. H. P., Melo, C. H. F., Dullemond, C. P., Andersen, J., Batalha, C., Vaz, L. P. R., & Mathieu, R. D. 2003, A&A, 409, 1037

Alencar, S. H. P., Teixeira, P. S., Guimarães, M. M., McGinnis, P. T., Gameiro, J. F., Bouvier, J., Aigrain, S., Flaccomio, E., & Favata, F. 2010, A&A, 519, A88

Alexander, R. D., Clarke, C. J., & Pringle, J. E. 2006a, MNRAS, 369, 216

—. 2006b, MNRAS, 369, 229

Allen, T. S., Prchlik, J. J., Megeath, S. T., Gutermuth, R. A., Pipher, J. L., Naylor, T., & Jeffries, R. D. 2014, ApJ, 786, 113

André, P. & Motte, F. 2000, in ESA Special Publication, Vol. 445, Star Formation from the Small to the Large Scale, ed. F. Favata, A. Kaas, & A. Wilson, 219

Andrews, S. M. & Williams, J. P. 2005, ApJ, 631, 1134

—. 2007a, ApJ, 671, 1800

—. 2007b, ApJ, 659, 705

Andrews, S. M., Wilner, D. J., Espaillat, C., Hughes, A. M., Dullemond, C. P., McClure, M. K., Qi, C., & Brown, J. M. 2011, ApJ, 732, 42

Appenzeller, I. & Bertout, C. 2013, A&A, 558, A83

Ardila, D. R., Basri, G., Walter, F. M., Valenti, J. A., & Johns-Krull, C. M. 2002, ApJ, 566, 1100

Ardila, D. R., Golimowski, D. A., Krist, J. E., Clampin, M., Ford, H. C., & Illingworth, G. D. 2007, ApJ, 665, 512

Ardila, D. R., Herczeg, G. J., Gregory, S. G., Ingleby, L., France, K., Brown, A., Edwards, S., Johns-Krull, C., Linsky, J. L., Yang, H., Valenti, J. A., Abgrall, H., Alexander, R. D., Bergin, E., Bethell, T., Brown, J. M., Calvet, N., Espaillat, C., Hillenbrand, L. A., Hussain, G., Roueff, E., Schindhelm, E. R., & Walter, F. M. 2013, ArXiv e-prints

Aresu, G., Meijerink, R., Kamp, I., Spaans, M., Thi, W.-F., & Woitke, P. 2012, A&A, 547, A69

Argiroffi, C., Maggio, A., Montmerle, T., Huenemoerder, D. P., Alecian, E., Audard, M., Bouvier, J., Damiani, F., Donati, J.-F., Gregory, S. G., Güdel, M., Hussain, G. A. J., Kastner, J. H., & Sacco, G. G. 2012, ApJ, 752, 100

Armitage, P. J. 2015, ArXiv e-prints

Armitage, P. J., Clarke, C. J., & Palla, F. 2003, MNRAS, 342, 1139

Armitage, P. J. & Rice, W. K. M. 2005, ArXiv Astrophysics e-prints

Arnaud, K. A. 1996, in Astronomical Society of the Pacific Conference Series, Vol. 101, Astronomical Data Analysis Software and Systems V, ed. G. H. Jacoby & J. Barnes, 17

Ayres, T. R. 2010, ApJS, 187, 149

Balucinska-Church, M. & McCammon, D. 1992, ApJ, 400, 699

Barnard, E. E. 1907, ApJ, 25

—. 1910, ApJ, 31

Bary, J. S., Weintraub, D. A., & Kastner, J. H. 2003, ApJ, 586, 1136

Bary, J. S., Weintraub, D. A., Shukla, S. J., Leisenring, J. M., & Kastner, J. H. 2008, ApJ, 678, 1088

Basri, G. & Batalha, C. 1990, ApJ, 363, 654

Bast, J. E., Brown, J. M., Herczeg, G. J., van Dishoeck, E. F., & Pontoppidan, K. M. 2011, A&A, 527, A119

Bergin, E., Calvet, N., D'Alessio, P., & Herczeg, G. J. 2003, ApJ, 591, L159

Bergin, E., Calvet, N., Sitko, M. L., Abgrall, H., D'Alessio, P., Herczeg, G. J., Roueff, E., Qi, C., Lynch, D. K., Russell, R. W., Brafford, S. M., & Perry, R. B. 2004, ApJ, 614, L133

Bergin, E. A. & Tafalla, M. 2007, ARA&A, 45, 339

Bertout, C., Basri, G., & Bouvier, J. 1988, ApJ, 330, 350

Bertout, C., Robichon, N., & Arenou, F. 1999, A&A, 352, 574

Bethell, T. & Bergin, E. 2009, Science, 326, 1675

Birnstiel, T., Andrews, S. M., & Ercolano, B. 2012a, A&A, 544, A79

Birnstiel, T., Andrews, S. M., Pinilla, P., & Kama, M. 2015, ApJ, 813, L14

Birnstiel, T., Dullemond, C. P., & Brauer, F. 2009, A&A, 503, L5

—. 2010a, A&A, 513, A79

Birnstiel, T., Klahr, H., & Ercolano, B. 2012b, A&A, 539, A148

Birnstiel, T., Ricci, L., Trotta, F., Dullemond, C. P., Natta, A., Testi, L., Dominik, C., Henning, T., Ormel, C. W., & Zsom, A. 2010b, A&A, 516, L14

Bitner, M. A., Richter, M. J., Lacy, J. H., Greathouse, T. K., Jaffe, D. T., & Blake, G. A. 2007, ApJ, 661, L69

Bitner, M. A., Richter, M. J., Lacy, J. H., Herczeg, G. J., Greathouse, T. K., Jaffe, D. T., Salyk, C., Blake, G. A., Hollenbach, D. J., Doppmann, G. W., Najita, J. R., & Currie, T. 2008, ApJ, 688, 1326

Blandford, R. D. & Payne, D. G. 1982, MNRAS, 199, 883

Blum, J. & Wurm, G. 2008, ARA&A, 46, 21

Bohlin, R. 1998, Absolute Flux Calibration For Prime STIS Echelle Modes With The 0.2x0.2" Slit, Tech. rep.

Bohlin, R. C., Savage, B. D., & Drake, J. F. 1978, ApJ, 224, 132

Böhm, T., Catala, C., Balona, L., & Carter, B. 2004, A&A, 427, 907

Bouvier, J., Alencar, S. H. P., Boutelier, T., Dougados, C., Balog, Z., Grankin, K., Hodgkin, S. T., Ibrahimov, M. A., Kun, M., Magakian, T. Y., & Pinte, C. 2007a, A&A, 463, 1017

—. 2007b, A&A, 463, 1017

Bouvier, J., Alencar, S. H. P., Harries, T. J., Johns-Krull, C. M., & Romanova, M. M. 2007c, Protostars and Planets V, 479

Bouvier, J., Chelli, A., Allain, S., Carrasco, L., Costero, R., Cruz-Gonzalez, I., Dougados, C., Fernández, M., Martín, E. L., Ménard, F., Mennessier, C., Mujica, R., Recillas, E., Salas, L., Schmidt, G., & Wichmann, R. 1999, A&A, 349, 619

Bouvier, J., Grankin, K., Ellerbroek, L., Bouy, H., & Barrado, D. 2013, ArXiv e-prints

Bouvier, J., Grankin, K. N., Alencar, S. H. P., Dougados, C., Fernández, M., Basri, G., Batalha, C., Guenther, E., Ibrahimov, M. A., Magakian, T. Y., Melnikov, S. Y., Petrov, P. P., Rud, M. V., & Zapatero Osorio, M. R. 2003, A&A, 409, 169

Brickhouse, N. S., Cranmer, S. R., Dupree, A. K., Luna, G. J. M., & Wolk, S. 2010, ApJ, 710, 1835

Brittain, S. D., Rettig, T. W., Simon, T., Kulesa, C., DiSanti, M. A., & Dello Russo, N. 2003, ApJ, 588, 535

Brown, A. G. A., de Geus, E. J., & de Zeeuw, P. T. 1994, A&A, 289, 101

Bruderer, S. 2013, A&A, 559, A46

Burgh, E. B., France, K., & Jenkins, E. B. 2010, ApJ, 708, 334

Burgh, E. B., France, K., & McCandliss, S. R. 2007, ApJ, 658, 446

Calvet, N. & Gullbring, E. 1998, ApJ, 509, 802

Calvet, N., Muzerolle, J., Briceño, C., Hernández, J., Hartmann, L., Saucedo, J. L., & Gordon, K. D. 2004, AJ, 128, 1294

Cameron, A. G. W. 1973, Space Sci. Rev., 14, 383

Cardelli, J. A., Clayton, G. C., & Mathis, J. S. 1989, ApJ, 345, 245

Carmona, A., van den Ancker, M. E., Henning, T., Pavlyuchenkov, Y., Dullemond, C. P., Goto, M., Thi, W. F., Bouwman, J., & Waters, L. B. F. M. 2008, A&A, 477, 839

Carpenter, K. G., Robinson, R. D., Wahlgren, G. M., Linsky, J. L., & Brown, A. 1994, ApJ, 428, 329

Carr, J. S. & Najita, J. R. 2008, Science, 319, 1504

Carr, J. S., Tokunaga, A. T., Najita, J., Shu, F. H., & Glassgold, A. E. 1993, ApJ, 411, L37

Casassus, S., van der Plas, G., M, S. P., Dent, W. R. F., Fomalont, E., Hagelberg, J., Hales, A., Jordán, A., Mawet, D., Ménard, F., Wootten, A., Wilner, D., Hughes, A. M., Schreiber, M. R., Girard, J. H., Ercolano, B., Canovas, H., Román, P. E., & Salinas, V. 2013, Nature, 493, 191

Castelli, F. & Kurucz, R. L. 2004, ArXiv Astrophysics e-prints

Cieza, L. A., Schreiber, M. R., Romero, G. A., Mora, M. D., Merin, B., Swift, J. J., Orellana, M., Williams, J. P., Harvey, P. M., & Evans, II, N. J. 2010, ApJ, 712, 925

Cieza, L. A., Swift, J. J., Mathews, G. S., & Williams, J. P. 2008, ApJ, 686, L115

Clarke, C. J., Gendrin, A., & Sotomayor, M. 2001, MNRAS, 328, 485

Coffey, D., Bacciotti, F., Woitas, J., Ray, T. P., & Eislöffel, J. 2004, ApJ, 604, 758

Comerón, F. & Fernández, M. 2010, A&A, 511, A10

Comerón, F., Fernández, M., Baraffe, I., Neuhäuser, R., & Kaas, A. A. 2003, A&A, 406, 1001

Correia, S., Zinnecker, H., Ratzka, T., & Sterzik, M. F. 2006, A&A, 459, 909

da Silva, L., Torres, C. A. O., de La Reza, R., Quast, G. R., Melo, C. H. F., & Sterzik, M. F. 2009, A&A, 508, 833

Danforth, C. W., Keeney, B. A., Stocke, J. T., Shull, J. M., & Yao, Y. 2010, ApJ, 720, 976

de la Reza, R. & Pinzón, G. 2004, AJ, 128, 1812

DeWarf, L. E., Sepinsky, J. F., Guinan, E. F., Ribas, I., & Nadalin, I. 2003, ApJ, 590, 357

Diplas, A. & Savage, B. D. 1994a, ApJS, 93, 211

—. 1994b, ApJ, 427, 274

Donati, J.-F., Skelly, M. B., Bouvier, J., Gregory, S. G., Grankin, K. N., Jardine, M. M., Hussain, G. A. J., Ménard, F., Dougados, C., Unruh, Y., Mohanty, S., Aurière, M., Morin, J., Farès, R., & MAPP Collaboration. 2010, MNRAS, 409, 1347

Donehew, B. & Brittain, S. 2011, AJ, 141, 46

Draine, B. T. 2003, ARA&A, 41, 241

—. 2011, Physics of the Interstellar and Intergalactic Medium

Draine, B. T. & Malhotra, S. 1993, ApJ, 414, 632

Duley, W. W. 2006, ApJ, 639, L59

Dullemond, C. P., Dominik, C., & Natta, A. 2001, ApJ, 560, 957

Durrance, S. T. 1981, J. Geophys. Res., 86, 9115

Edwards, S., Kwan, J., Fischer, W., Hillenbrand, L., Finn, K., Fedorenko, K., & Feng, W. 2013, ApJ, 778, 148

Eggen, O. J. 1986, AJ, 92, 1074

Eidelsberg, M., Jolly, A., Lemaire, J. L., Tchang-Brillet, W.-Ü., Breton, J., & Rostas, F. 1999, A&A, 346, 705

Eidelsberg, M. & Rostas, F. 2003, ApJS, 145, 89

Eisner, J. A., Hillenbrand, L. A., White, R. J., Bloom, J. S., Akeson, R. L., & Blake, C. H. 2007, ApJ, 669, 1072

Espaillat, C., Calvet, N., D'Alessio, P., Bergin, E., Hartmann, L., Watson, D., Furlan, E., Najita, J., Forrest, W., McClure, M., Sargent, B., Bohac, C., & Harrold, S. T. 2007, ApJ, 664, L111

Espaillat, C., D'Alessio, P., Hernández, J., Nagel, E., Luhman, K. L., Watson, D. M., Calvet, N., Muzerolle, J., & McClure, M. 2010, ApJ, 717, 441

Espaillat, C., Furlan, E., D'Alessio, P., Sargent, B., Nagel, E., Calvet, N., Watson, D. M., & Muzerolle, J. 2011, ApJ, 728, 49

Fedele, D., van den Ancker, M. E., Henning, T., Jayawardhana, R., & Oliveira, J. M. 2010, A&A, 510, A72

Federman, S. R., Glassgold, A. E., Jenkins, E. B., & Shaya, E. J. 1980, ApJ, 242, 545

Feigelson, E. D., Lawson, W. A., & Garmire, G. P. 2003, ApJ, 599, 1207

Feldman, P. D. & Brune, W. H. 1976, ApJ, 209, L45

Feldman, P. D., Burgh, E. B., Durrance, S. T., & Davidsen, A. F. 2000, ApJ, 538, 395

Finkenzeller, U. 1985, A&A, 151, 340

Finocchi, F., Gail, H.-P., Duschl, W. J., & Tscharnuter, W. M. 1996, in Astronomical Society of the Pacific Conference Series, Vol. 104, IAU Colloq. 150: Physics, Chemistry, and Dynamics of Interplanetary Dust, ed. B. A. S. Gustafson & M. S. Hanner, 517

Fischer, W., Edwards, S., Hillenbrand, L., & Kwan, J. 2011, ApJ, 730, 73

Fitzpatrick, E. L. 1999, PASP, 111, 63

Fitzpatrick, E. L. & Massa, D. 1990, ApJS, 72, 163

—. 2005, AJ, 130, 1127

Fogel, J. K. J., Bethell, T. J., Bergin, E. A., Calvet, N., & Semenov, D. 2011, ApJ, 726, 29

France, K., Burgh, E. B., Herczeg, G. J., Schindhelm, E., Yang, H., Abgrall, H., Roueff, E.,
    Brown, A., Brown, J. M., & Linsky, J. L. 2012a, ApJ, 744, 22

France, K., Schindhelm, E., Bergin, E. A., Roueff, E., & Abgrall, H. 2014, ApJ, 784, 127

France, K., Schindhelm, E., Burgh, E. B., Herczeg, G. J., Harper, G. M., Brown, A., Green,
    J. C., Linsky, J. L., Yang, H., Abgrall, H., Ardila, D. R., Bergin, E., Bethell, T.,
    Brown, J. M., Calvet, N., Espaillat, C., Gregory, S. G., Hillenbrand, L. A., Hussain,
    G., Ingleby, L., Johns-Krull, C. M., Roueff, E., Valenti, J. A., & Walter, F. M. 2011a,
    ApJ, 734, 31

France, K., Schindhelm, E., Herczeg, G. J., Brown, A., Abgrall, H., Alexander, R. D., Bergin,
    E. A., Brown, J. M., Linsky, J. L., Roueff, E., & Yang, H. 2012b, ApJ, 756, 171

France, K., Yang, H., & Linsky, J. L. 2011b, ApJ, 729, 7

Franciosini, E., Scelsi, L., Pallavicini, R., & Audard, M. 2007, A&A, 471, 951

Froning, C. S., Cantrell, A. G., Maccarone, T. J., France, K., Khargharia, J., Winter, L. M.,
    Robinson, E. L., Hynes, R. I., Broderick, J. W., Markoff, S., Torres, M. A. P., Garcia,
    M., Bailyn, C. D., Prochaska, J. X., Werk, J., Thom, C., Béland, S., Danforth, C. W.,
    Keeney, B., & Green, J. C. 2011, ApJ, 743, 26

Fukagawa, M., Tsukagoshi, T., Momose, M., Saigo, K., Ohashi, N., Kitamura, Y., Inutsuka,
    S.-i., Muto, T., Nomura, H., Takeuchi, T., Kobayashi, H., Hanawa, T., Akiyama, E.,
    Honda, M., Fujiwara, H., Kataoka, A., Takahashi, S. Z., & Shibai, H. 2013, ArXiv
    e-prints

Furlan, E., Luhman, K. L., Espaillat, C., D'Alessio, P., Adame, L., Manoj, P., Kim, K. H., Watson, D. M., Forrest, W. J., McClure, M. K., Calvet, N., Sargent, B. A., Green, J. D., & Fischer, W. J. 2011, ApJS, 195, 3

Garcia Lopez, R., Natta, A., Testi, L., & Habart, E. 2006, A&A, 459, 837

Gauvin, L. S. & Strom, K. M. 1992, ApJ, 385, 217

Geoffray, H. & Monin, J.-L. 2001, A&A, 369, 239

Gerbaldi, M., Faraggiana, R., Burnage, R., Delmas, F., Gómez, A. E., & Grenier, S. 1999, A&AS, 137, 273

Ghez, A. M., Neugebauer, G., & Matthews, K. 1993, AJ, 106, 2005

Głębocki, R. & Gnaciński, P. 2005, in ESA Special Publication, Vol. 560, 13th Cambridge Workshop on Cool Stars, Stellar Systems and the Sun, ed. F. Favata, G. A. J. Hussain, & B. Battrick, 571

Gómez de Castro, A. I. 2009, ApJ, 698, L108

Gorti, U., Dullemond, C. P., & Hollenbach, D. 2009, ApJ, 705, 1237

Gorti, U. & Hollenbach, D. 2009, ApJ, 690, 1539

Grady, C. A., Schneider, G., Sitko, M. L., Williger, G. M., Hamaguchi, K., Brittain, S. D., Ablordeppey, K., Apai, D., Beerman, L., Carpenter, W. J., Collins, K. A., Fukagawa, M., Hammel, H. B., Henning, T., Hines, D., Kimes, R., Lynch, D. K., Ménard, F., Pearson, R., Russell, R. W., Silverstone, M., Smith, P. S., Troutman, M., Wilner, D., Woodgate, B., & Clampin, M. 2009, ApJ, 699, 1822

Grady, C. A., Woodgate, B., Heap, S. R., Bowers, C., Nuth, III, J. A., Herczeg, G. J., & Hill, H. G. M. 2005, ApJ, 620, 470

Grady, C. A., Woodgate, B., Torres, C. A. O., Henning, T., Apai, D., Rodmann, J., Wang, H., Stecklum, B., Linz, H., Williger, G. M., Brown, A., Wilkinson, E., Harper, G. M., Herczeg, G. J., Danks, A., Vieira, G. L., Malumuth, E., Collins, N. R., & Hill, R. S. 2004, ApJ, 608, 809

Green, J. C., Froning, C. S., Osterman, S., Ebbets, D., Heap, S. H., Leitherer, C., Linsky, J. L., Savage, B. D., Sembach, K., Shull, J. M., Siegmund, O. H. W., Snow, T. P., Spencer, J., Stern, S. A., Stocke, J., Welsh, B., Béland, S., Burgh, E. B., Danforth, C., France, K., Keeney, B., McPhate, J., Penton, S. V., Andrews, J., Brownsberger, K., Morse, J., & Wilkinson, E. 2012, ApJ, 744, 60

Güdel, M., Briggs, K. R., Arzner, K., Audard, M., Bouvier, J., Feigelson, E. D., Franciosini, E., Glauser, A., Grosso, N., Micela, G., Monin, J.-L., Montmerle, T., Padgett, D. L., Palla, F., Pillitteri, I., Rebull, L., Scelsi, L., Silva, B., Skinner, S. L., Stelzer, B., & Telleschi, A. 2007a, A&A, 468, 353

Güdel, M., Telleschi, A., Audard, M., Skinner, S. L., Briggs, K. R., Palla, F., & Dougados, C. 2007b, A&A, 468, 515

Guilloteau, S. & Dutrey, A. 1998, A&A, 339, 467

Gullbring, E., Calvet, N., Muzerolle, J., & Hartmann, L. 2000, ApJ, 544, 927

Gullbring, E., Hartmann, L., Briceno, C., & Calvet, N. 1998, ApJ, 492, 323

Günther, H. M. & Schmitt, J. H. M. M. 2008, A&A, 481, 735

—. 2009, A&A, 494, 1041

Haridass, C. & Huber, K. P. 1994, ApJ, 420, 433

Hartigan, P., Edwards, S., & Ghandour, L. 1995, ApJ, 452, 736

Hartigan, P. & Kenyon, S. J. 2003, ApJ, 583, 334

Hartmann, L., Calvet, N., Gullbring, E., & D'Alessio, P. 1998, ApJ, 495, 385

Hartmann, L., Hewett, R., & Calvet, N. 1994, ApJ, 426, 669

Hartmann, L., Hewett, R., Stahler, S., & Mathieu, R. D. 1986, ApJ, 309, 275

Hashimoto, J., Tamura, M., Muto, T., Kudo, T., Fukagawa, M., Fukue, T., Goto, M., Grady, C. A., Henning, T., Hodapp, K., Honda, M., Inutsuka, S., Kokubo, E., Knapp, G., McElwain, M. W., Momose, M., Ohashi, N., Okamoto, Y. K., Takami, M., Turner, E. L., Wisniewski, J., Janson, M., Abe, L., Brandner, W., Carson, J., Egner, S., Feldt, M., Golota, T., Guyon, O., Hayano, Y., Hayashi, M., Hayashi, S., Ishii, M., Kandori, R., Kusakabe, N., Matsuo, T., Mayama, S., Miyama, S., Morino, J.-I., Moro-Martin, A., Nishimura, T., Pyo, T.-S., Suto, H., Suzuki, R., Takato, N., Terada, H., Thalmann, C., Tomono, D., Watanabe, M., Yamada, T., Takami, H., & Usuda, T. 2011, ApJ, 729, L17

Henning, T. 2010, ARA&A, 48, 21

Herbst, W., Herbst, D. K., Grossman, E. J., & Weinstein, D. 1994, AJ, 108, 1906

Herczeg, G. J. & Hillenbrand, L. A. 2008, ApJ, 681, 594

—. 2014, ApJ, 786, 97

Herczeg, G. J., Linsky, J. L., Valenti, J. A., Johns-Krull, C. M., & Wood, B. E. 2002, ApJ, 572, 310

Herczeg, G. J., Linsky, J. L., Walter, F. M., Gahm, G. F., & Johns-Krull, C. M. 2006, ApJS, 165, 256

Herczeg, G. J., Walter, F. M., Linsky, J. L., Gahm, G. F., Ardila, D. R., Brown, A., Johns-Krull, C. M., Simon, M., & Valenti, J. A. 2005, AJ, 129, 2777

Herczeg, G. J., Wood, B. E., Linsky, J. L., Valenti, J. A., & Johns-Krull, C. M. 2004, ApJ, 607, 369

Hernández, J., Calvet, N., Briceño, C., Hartmann, L., Vivas, A. K., Muzerolle, J., Downes, J., Allen, L., & Gutermuth, R. 2007, ApJ, 671, 1784

Herzberg, G. 1950, Molecular spectra and molecular structure. Vol.1: Spectra of diatomic molecules

Hoadley, K., France, K., Alexander, R. D., McJunkin, M., & Schneider, C. 2015a, ArXiv e-prints

Hoadley, K., France, K., Alexander, R. D., McJunkin, M., & Schneider, P. C. 2015b, ApJ, 812, 41

Hollenbach, D., Johnstone, D., Lizano, S., & Shu, F. 1994, ApJ, 428, 654

Horne, D., Gibb, E., Rettig, T. W., Brittain, S., Tilley, D., & Balsara, D. 2012, ApJ, 754, 64

Hubickyj, O., Bodenheimer, P., & Lissauer, J. J. 2005, Icarus, 179, 415

Huenemoerder, D. P., Kastner, J. H., Testa, P., Schulz, N. S., & Weintraub, D. A. 2007, ApJ, 671, 592

Hughes, A. M., Wilner, D. J., Andrews, S. M., Qi, C., & Hogerheijde, M. R. 2011, ApJ, 727, 85

Hughes, J., Hartigan, P., Krautter, J., & Kelemen, J. 1994, AJ, 108, 1071

Hussain, G. A. J., Collier Cameron, A., Jardine, M. M., Dunstone, N., Ramirez Velez, J., Stempels, H. C., Donati, J.-F., Semel, M., Aulanier, G., Harries, T., Bouvier, J., Dougados, C., Ferreira, J., Carter, B. D., & Lawson, W. A. 2009, MNRAS, 398, 189

Ida, S. & Lin, D. N. C. 2004, ApJ, 604, 388

Ingleby, L., Calvet, N., Bergin, E., Herczeg, G., Brown, A., Alexander, R., Edwards, S., Espaillat, C., France, K., Gregory, S. G., Hillenbrand, L., Roueff, E., Valenti, J.,

Walter, F., Johns-Krull, C., Brown, J., Linsky, J., McClure, M., Ardila, D., Abgrall, H., Bethell, T., Hussain, G., & Yang, H. 2011, ApJ, 743, 105

Ingleby, L., Calvet, N., Bergin, E., Yerasi, A., Espaillat, C., Herczeg, G., Roueff, E., Abgrall, H., Hernández, J., Briceño, C., Pascucci, I., Miller, J., Fogel, J., Hartmann, L., Meyer, M., Carpenter, J., Crockett, N., & McClure, M. 2009, ApJ, 703, L137

Isella, A., Testi, L., Natta, A., Neri, R., Wilner, D., & Qi, C. 2007, A&A, 469, 213

Joblin, C., Leger, A., & Martin, P. 1992, ApJ, 393, L79

Johns-Krull, C. M. & Herczeg, G. J. 2007, ApJ, 655, 345

Johns-Krull, C. M. & Valenti, J. A. 2001, ApJ, 561, 1060

Johns-Krull, C. M., Valenti, J. A., & Linsky, J. L. 2000, ApJ, 539, 815

Jonkheid, B., Faas, F. G. A., van Zadelhoff, G.-J., & van Dishoeck, E. F. 2004, A&A, 428, 511

Kamp, I. & Bertoldi, F. 2000, A&A, 353, 276

Kamp, I. & Dullemond, C. P. 2004, ApJ, 615, 991

Kamp, I. & van Zadelhoff, G.-J. 2001, A&A, 373, 641

Kastner, J. H., Huenemoerder, D. P., Schulz, N. S., Canizares, C. R., & Weintraub, D. A. 2002, ApJ, 567, 434

Kenyon, S. J. & Hartmann, L. 1995, ApJS, 101, 117

Kimble, R. A., Woodgate, B. E., Bowers, C. W., Kraemer, S. B., Kaiser, M. E., Gull, T. R., Heap, S. R., Danks, A. C., Boggess, A., Green, R. F., Hutchings, J. B., Jenkins, E. B., Joseph, C. L., Linsky, J. L., Maran, S. P., Moos, H. W., Roesler, F., Timothy, J. G., Weistrop, D. E., Grady, J. F., Loiacono, J. J., Brown, L. W., Brumfield, M. D.,

Content, D. A., Feinberg, L. D., Isaacs, M. N., Krebs, C. A., Krueger, V. L., Melcher, R. W., Rebar, F. J., Vitagliano, H. D., Yagelowich, J. J., Meyer, W. W., Hood, D. F., Argabright, V. S., Becker, S. I., Bottema, M., Breyer, R. R., Bybee, R. L., Christon, P. R., Delamere, A. W., Dorn, D. A., Downey, S., Driggers, P. A., Ebbets, D. C., Gallegos, J. S., Garner, H., Hetlinger, J. C., Lettieri, R. L., Ludtke, C. W., Michika, D., Nyquist, R., Rose, D. M., Stocker, R. B., Sullivan, J. F., van Houten, C. N., Woodruff, R. A., Baum, S. A., Hartig, G. F., Balzano, V., Biagetti, C., Blades, J. C., Bohlin, R. C., Clampin, M., Doxsey, R., Ferguson, H. C., Goudfrooij, P., Hulbert, S. J., Kutina, R., McGrath, M., Lindler, D. J., Beck, T. L., Feggans, J. K., Plait, P. C., Sandoval, J. L., Hill, R. S., Collins, N. R., Cornett, R. H., Fowler, W. B., Hill, R. J., Landsman, W. B., Malumuth, E. M., Standley, C., Blouke, M., Gruszczak, A., Reed, R., Robinson, R. D., Valenti, J. A., & Wolfe, T. 1998, ApJ, 492, L83

Kirby, K. & Cooper, D. L. 1989, 90, 4895

Kraus, A. L. & Hillenbrand, L. A. 2009, ApJ, 704, 531

Kuiper, G. P. 1949, ApJ, 109, 308

—. 1956, JRASC, 50, 105

Kun, M. 1998, ApJS, 115, 59

Kurosawa, R., Harries, T. J., & Symington, N. H. 2006, MNRAS, 370, 580

Kwan, J. & Fischer, W. 2011, MNRAS, 411, 2383

Lacy, J. H., Knacke, R., Geballe, T. R., & Tokunaga, A. T. 1994, ApJ, 428, L69

Lahuis, F., van Dishoeck, E. F., Boogert, A. C. A., Pontoppidan, K. M., Blake, G. A., Dullemond, C. P., Evans, II, N. J., Hogerheijde, M. R., Jørgensen, J. K., Kessler-Silacci, J. E., & Knez, C. 2006, ApJ, 636, L145

Lamzin, S. A. 2006, Astronomy Letters, 32, 176

Lawson, W. A., Crause, L. A., Mamajek, E. E., & Feigelson, E. D. 2001, MNRAS, 321, 57

Lawson, W. A., Feigelson, E. D., & Huenemoerder, D. P. 1996, MNRAS, 280, 1071

Lawson, W. A., Lyo, A.-R., & Muzerolle, J. 2004, MNRAS, 351, L39

Li, A. & Draine, B. T. 2001, ApJ, 554, 778

Lissauer, J. J. 1993, ARA&A, 31, 129

Liu, W. & Dalgarno, A. 1996, ApJ, 467, 446

Loinard, L., Torres, R. M., Mioduszewski, A. J., Rodríguez, L. F., González-Lópezlira, R. A., Lachaume, R., Vázquez, V., & González, E. 2007, ApJ, 671, 546

Lombardi, M., Alves, J., & Lada, C. J. 2011, A&A, 535, A16

Lombardi, M., Lada, C. J., & Alves, J. 2008, A&A, 489, 143

—. 2010, A&A, 512, A67

López-Martín, L., Cabrit, S., & Dougados, C. 2003, A&A, 405, L1

López-Santiago, J., Albacete Colombo, J. F., & López-García, M. A. 2010, A&A, 524, A97

Luhman, K. L. 2004, ApJ, 602, 816

Luhman, K. L. & Steeghs, D. 2004, ApJ, 609, 917

Lynden-Bell, D. 1996, MNRAS, 279, 389

—. 2003, MNRAS, 341, 1360

Lyo, A.-R., Ohashi, N., Qi, C., Wilner, D. J., & Su, Y.-N. 2011, AJ, 142, 151

Malaroda, S., Levato, H., & Galliani, S. 2006, VizieR Online Data Catalog, 3249, 0

Maloney, P. R., Hollenbach, D. J., & Tielens, A. G. G. M. 1996, ApJ, 466, 561

Mamajek, E. E. 2005, ApJ, 634, 1385

Mamajek, E. E., Lawson, W. A., & Feigelson, E. D. 1999, PASA, 16, 257

—. 2000, ApJ, 544, 356

Martin-Zaïdi, C., Deleuil, M., Le Bourlot, J., Bouret, J.-C., Roberge, A., Dullemond, C. P., Testi, L., Feldman, P. D., Lecavelier Des Etangs, A., & Vidal-Madjar, A. 2008, A&A, 484, 225

Massa, D. & Fitzpatrick, E. L. 2000, ApJS, 126, 517

Mathis, J. S. 1994, ApJ, 422, 176

McClure, M. K., Calvet, N., Espaillat, C., Hartmann, L., Hernández, J., Ingleby, L., Luhman, K. L., D'Alessio, P., & Sargent, B. 2013, ApJ, 769, 73

McJunkin, M., France, K., Burgh, E. B., Herczeg, G. J., Schindhelm, E., Brown, J. M., & Brown, A. 2013, ApJ, 766, 12

McJunkin, M., France, K., Schneider, P. C., Herczeg, G. J., Brown, A., Hillenbrand, L., Schindhelm, E., & Edwards, S. 2014, ApJ, 780, 150

McPhate, J. B., McCandliss, S. R., Feldman, P. D., Burgh, E. B., & Pelton, R. 1997, in Bulletin of the American Astronomical Society, Vol. 29, AAS/Division for Planetary Sciences Meeting Abstracts #29, 1051

Mennella, V., Colangeli, L., Bussoletti, E., Palumbo, P., & Rotundi, A. 1998, ApJ, 507, L177

Mooley, K., Hillenbrand, L., Rebull, L., Padgett, D., & Knapp, G. 2013, ApJ, 771, 110

Müller, A., van den Ancker, M. E., Launhardt, R., Pott, J. U., Fedele, D., & Henning, T. 2011, A&A, 530, A85

Muzerolle, J., Calvet, N., Briceño, C., Hartmann, L., & Hillenbrand, L. 2000, ApJ, 535, L47

Muzerolle, J., Calvet, N., Hartmann, L., & D'Alessio, P. 2003, ApJ, 597, L149

Muzerolle, J., Hartmann, L., & Calvet, N. 1998, AJ, 116, 455

Najita, J., Carr, J. S., & Mathieu, R. D. 2003, ApJ, 589, 931

Najita, J. R., Carr, J. S., Glassgold, A. E., & Valenti, J. A. 2007, Protostars and Planets V, 507

Najita, J. R., Crockett, N., & Carr, J. S. 2008, ApJ, 687, 1168

Nakagawa, Y., Nakazawa, K., & Hayashi, C. 1981, Icarus, 45, 517

Nguyen, D. C., Brandeker, A., van Kerkwijk, M. H., & Jayawardhana, R. 2012, ApJ, 745, 119

Nomura, H., Aikawa, Y., Tsujimoto, M., Nakagawa, Y., & Millar, T. J. 2007, ApJ, 661, 334

Nomura, H. & Millar, T. J. 2005, A&A, 438, 923

O'Donnell, J. E. 1994, ApJ, 422, 158

Owen, J. E., Clarke, C. J., & Ercolano, B. 2012, MNRAS, 422, 1880

Owen, J. E., Ercolano, B., Clarke, C. J., & Alexander, R. D. 2010, MNRAS, 401, 1415

Panoglou, D., Cabrit, S., Pineau Des Forêts, G., Garcia, P. J. V., Ferreira, J., & Casse, F. 2012, A&A, 538, A2

Papaloizou, J. C. B. & Terquem, C. 2006, Reports on Progress in Physics, 69, 119

Pascucci, I., Gorti, U., Hollenbach, D., Najita, J., Meyer, M. R., Carpenter, J. M., Hillenbrand, L. A., Herczeg, G. J., Padgett, D. L., Mamajek, E. E., Silverstone, M. D., Schlingman, W. M., Kim, J. S., Stobie, E. B., Bouwman, J., Wolf, S., Rodmann, J., Hines, D. C., Lunine, J., & Malhotra, R. 2006, ApJ, 651, 1177

Pascucci, I. & Sterzik, M. 2009, ApJ, 702, 724

Pelletier, G. & Pudritz, R. E. 1992, ApJ, 394, 117

Pontoppidan, K. M., Blake, G. A., & Smette, A. 2011, ApJ, 733, 84

Pontoppidan, K. M., Blake, G. A., van Dishoeck, E. F., Smette, A., Ireland, M. J., & Brown, J. 2008, ApJ, 684, 1323

Preibisch, T. & Mamajek, E. 2008, The Nearest OB Association: Scorpius-Centaurus (Sco OB2), ed. B. Reipurth, 235

Pudritz, R. E. & Norman, C. A. 1986, ApJ, 301, 571

Pudritz, R. E., Ouyed, R., Fendt, C., & Brandenburg, A. 2007, Protostars and Planets V, 277

Quast, G. R., Torres, C. A. O., de La Reza, R., da Silva, L., & Mayor, M. 2000, in IAU Symposium, Vol. 200, IAU Symposium, 28P

Rachford, B. L., Snow, T. P., Destree, J. D., Ross, T. L., Ferlet, R., Friedman, S. D., Gry, C., Jenkins, E. B., Morton, D. C., Savage, B. D., Shull, J. M., Sonnentrucker, P., Tumlinson, J., Vidal-Madjar, A., Welty, D. E., & York, D. G. 2009, ApJS, 180, 125

Rachford, B. L., Snow, T. P., Tumlinson, J., Shull, J. M., Blair, W. P., Ferlet, R., Friedman, S. D., Gry, C., Jenkins, E. B., Morton, D. C., Savage, B. D., Sonnentrucker, P., Vidal-Madjar, A., Welty, D. E., & York, D. G. 2002, ApJ, 577, 221

Ramsay Howat, S. K. & Greaves, J. S. 2007, MNRAS, 379, 1658

Rebull, L. M., Padgett, D. L., McCabe, C.-E., Hillenbrand, L. A., Stapelfeldt, K. R., Noriega-Crespo, A., Carey, S. J., Brooke, T., Huard, T., Terebey, S., Audard, M., Monin, J.-L., Fukagawa, M., Güdel, M., Knapp, G. R., Menard, F., Allen, L. E., Angione, J. R., Baldovin-Saavedra, C., Bouvier, J., Briggs, K., Dougados, C., Evans, N. J.,

Flagey, N., Guieu, S., Grosso, N., Glauser, A. M., Harvey, P., Hines, D., Latter, W. B., Skinner, S. L., Strom, S., Tromp, J., & Wolf, S. 2010, ApJS, 186, 259

Redfield, S. & Linsky, J. L. 2004, ApJ, 602, 776

Reipurth, B. & Schneider, N. 2008, Star Formation and Young Clusters in Cygnus, ed. B. Reipurth, 36

Rettig, T., Brittain, S., Simon, T., Gibb, E., Balsara, D. S., Tilley, D. A., & Kulesa, C. 2006, ApJ, 646, 342

Rettig, T. W., Haywood, J., Simon, T., Brittain, S. D., & Gibb, E. 2004, ApJ, 616, L163

Ricci, L., Testi, L., Natta, A., Neri, R., Cabrit, S., & Herczeg, G. J. 2010, A&A, 512, A15

Rieke, G. H. & Lebofsky, M. J. 1985, ApJ, 288, 618

Robrade, J. & Schmitt, J. H. M. M. 2007, A&A, 473, 229

Rodriguez, D. R., Kastner, J. H., Wilner, D., & Qi, C. 2010, ApJ, 720, 1684

Rodriguez, J. E., Pepper, J., Stassun, K. G., Siverd, R. J., Cargile, P., Beatty, T. G., & Gaudi, B. S. 2013, AJ, 146, 112

Rosenfeld, K. A., Andrews, S. M., Wilner, D. J., & Stempels, H. C. 2012a, ApJ, 759, 119

Rosenfeld, K. A., Qi, C., Andrews, S. M., Wilner, D. J., Corder, S. A., Dullemond, C. P., Lin, S.-Y., Hughes, A. M., D'Alessio, P., & Ho, P. T. P. 2012b, ApJ, 757, 129

Rucinski, S. M. & Krautter, J. 1983, A&A, 121, 217

Rudnick, J. 1936, ApJ, 83, 394

Safier, P. N. 1993, ApJ, 408, 115

Salyk, C., Blake, G. A., Boogert, A. C. A., & Brown, J. M. 2007, ApJ, 655, L105

—. 2011a, ApJ, 743, 112

Salyk, C., Pontoppidan, K. M., Blake, G. A., Lahuis, F., van Dishoeck, E. F., & Evans, II, N. J. 2008, ApJ, 676, L49

Salyk, C., Pontoppidan, K. M., Blake, G. A., Najita, J. R., & Carr, J. S. 2011b, ApJ, 731, 130

Savage, B. D. & Mathis, J. S. 1979, ARA&A, 17, 73

Schindhelm, E., France, K., Burgh, E. B., Herczeg, G. J., Green, J. C., Brown, A., Brown, J. M., & Valenti, J. A. 2012a, ApJ, 746, 97

Schindhelm, E., France, K., Herczeg, G. J., Bergin, E., Yang, H., Brown, A., Brown, J. M., Linsky, J. L., & Valenti, J. 2012b, ApJ, 756, L23

Schmitt, J. H. M. M. & Robrade, J. 2007, A&A, 462, L41

Schnaiter, M., Mutschke, H., Dorschner, J., Henning, T., & Salama, F. 1998, ApJ, 498, 486

Schneider, P. C., Eislöffel, J., Güdel, M., Günther, H. M., Herczeg, G., Robrade, J., & Schmitt, J. H. M. M. 2013, A&A, 557, A110

Schneider, P. C. & Schmitt, J. H. M. M. 2008, A&A, 488, L13

Shakura, N. I. & Sunyaev, R. A. 1973, A&A, 24, 337

Sheffer, Y., Rogers, M., Federman, S. R., Lambert, D. L., & Gredel, R. 2007, ApJ, 667, 1002

Shevchenko, V. S., Ibragimov, M. A., & Chenysheva, T. L. 1991, Soviet Ast., 35, 229

Siess, L., Dufour, E., & Forestini, M. 2000, A&A, 358, 593

Simon, M., Dutrey, A., & Guilloteau, S. 2000, ApJ, 545, 1034

Skinner, S. L. & Güdel, M. 2013, ApJ, 765, 3

Skinner, S. L., Güdel, M., Audard, M., & Smith, K. 2004, ApJ, 614, 221

Skrutskie, M. F., Meyer, M. R., Whalen, D., & Hamilton, C. 1996, AJ, 112, 2168

Smith, R. L., Pontoppidan, K. M., Young, E. D., Morris, M. R., & van Dishoeck, E. F. 2009, ApJ, 701, 163

Stelzer, B. & Schmitt, J. H. M. M. 2004, A&A, 418, 687

Stempels, H. C., Gahm, G. F., & Petrov, P. P. 2007, A&A, 461, 253

Swartz, D. A., Drake, J. J., Elsner, R. F., Ghosh, K. K., Grady, C. A., Wassell, E., Woodgate, B. E., & Kimble, R. A. 2005, ApJ, 628, 811

Tanaka, H., Takeuchi, T., & Ward, W. R. 2002, ApJ, 565, 1257

Tanaka, K. E. I., Nakamoto, T., & Omukai, K. 2013, ArXiv e-prints

Tang, Y.-W., Guilloteau, S., Piétu, V., Dutrey, A., Ohashi, N., & Ho, P. T. P. 2012, A&A, 547, A84

Testa, P., Huenemoerder, D. P., Schulz, N. S., & Ishibashi, K. 2008, ApJ, 687, 579

Testi, L., Palla, F., & Natta, A. 1998, A&AS, 133, 81

Tielens, A. G. G. M. 2008, ARA&A, 46, 289

Torres, C. A. O., Quast, G. R., Melo, C. H. F., & Sterzik, M. F. 2008, Young Nearby Loose Associations, ed. B. Reipurth, 757

Trilling, D. E., Lunine, J. I., & Benz, W. 2002, A&A, 394, 241

Trumpler, R. J. 1930, PASP, 42, 214

Valenti, J. A., Johns-Krull, C. M., & Linsky, J. L. 2000, ApJS, 129, 399

van Boekel, R., Min, M., Waters, L. B. F. M., de Koter, A., Dominik, C., van den Ancker, M. E., & Bouwman, J. 2005, A&A, 437, 189

van den Ancker, M. E., de Winter, D., & Tjin A Djie, H. R. E. 1998, A&A, 330, 145

van den Ancker, M. E., The, P. S., Tjin A Djie, H. R. E., Catala, C., de Winter, D., Blondel, P. F. C., & Waters, L. B. F. M. 1997, A&A, 324, L33

van der Marel, N., van Dishoeck, E. F., Bruderer, S., Birnstiel, T., Pinilla, P., Dullemond, C. P., van Kempen, T. A., Schmalzl, M., Brown, J. M., Herczeg, G. J., Mathews, G. S., & Geers, V. 2013, Science, 340, 1199

van Leeuwen, F. 2007, A&A, 474, 653

Vasyunin, A. I., Wiebe, D. S., Birnstiel, T., Zhukovska, S., Henning, T., & Dullemond, C. P. 2011, ApJ, 727, 76

Vidal-Madjar, A., Lagrange-Henri, A.-M., Feldman, P. D., Beust, H., Lissauer, J. J., Deleuil, M., Ferlet, R., Gry, C., Hobbs, L. M., McGrath, M. A., McPhate, J. B., & Moos, H. W. 1994, A&A, 290, 245

Vieira, S. L. A., Corradi, W. J. B., Alencar, S. H. P., Mendes, L. T. S., Torres, C. A. O., Quast, G. R., Guimarães, M. M., & da Silva, L. 2003, AJ, 126, 2971

Visser, R., van Dishoeck, E. F., & Black, J. H. 2009, A&A, 503, 323

Vuong, M. H., Montmerle, T., Grosso, N., Feigelson, E. D., Verstraete, L., & Ozawa, H. 2003, A&A, 408, 581

Walter, F. M., Herczeg, G., Brown, A., Ardila, D. R., Gahm, G. F., Johns-Krull, C. M., Lissauer, J. J., Simon, M., & Valenti, J. A. 2003, AJ, 126, 3076

Ward, W. R. 1997, Icarus, 126, 261

Webb, R. A., Zuckerman, B., Platais, I., Patience, J., White, R. J., Schwartz, M. J., & McCarthy, C. 1999, ApJ, 512, L63

Weidenschilling, S. J. 1977, MNRAS, 180, 57

—. 1980, Icarus, 44, 172

Welty, D. E. & Fowler, J. R. 1992, ApJ, 393, 193

White, R. J. & Ghez, A. M. 2001, ApJ, 556, 265

White, R. J. & Hillenbrand, L. A. 2004, ApJ, 616, 998

Whittet, D. C. B., Shenoy, S. S., Clayton, G. C., & Gordon, K. D. 2004, ApJ, 602, 291

Wiese, W. L. & Fuhr, J. R. 2009, Journal of Physical and Chemical Reference Data, 38, 565

Williams, J. P. & Cieza, L. A. 2011, ARA&A, 49, 67

Woitke, P., Kamp, I., & Thi, W.-F. 2009, A&A, 501, 383

Woitke, P., Riaz, B., Duchêne, G., Pascucci, I., Lyo, A.-R., Dent, W. R. F., Phillips, N., Thi, W.-F., Ménard, F., Herczeg, G. J., Bergin, E., Brown, A., Mora, A., Kamp, I., Aresu, G., Brittain, S., de Gregorio-Monsalvo, I., & Sandell, G. 2011, A&A, 534, A44

Wolven, B. C., Feldman, P. D., Strobel, D. F., & McGrath, M. A. 1997, ApJ, 475, 835

Wood, B. E., Karovska, M., & Raymond, J. C. 2002, ApJ, 575, 1057

Woodgate, B. E., Kimble, R. A., Bowers, C. W., Kraemer, S., Kaiser, M. E., Danks, A. C., Grady, J. F., Loiacono, J. J., Brumfield, M., Feinberg, L., Gull, T. R., Heap, S. R., Maran, S. P., Lindler, D., Hood, D., Meyer, W., Vanhouten, C., Argabright, V., Franka, S., Bybee, R., Dorn, D., Bottema, M., Woodruff, R., Michika, D., Sullivan, J., Hetlinger, J., Ludtke, C., Stocker, R., Delamere, A., Rose, D., Becker, I., Garner, H., Timothy, J. G., Blouke, M., Joseph, C. L., Hartig, G., Green, R. F., Jenkins,

E. B., Linsky, J. L., Hutchings, J. B., Moos, H. W., Boggess, A., Roesler, F., & Weistrop, D. 1998, PASP, 110, 1183

Wyatt, M. C. 2008, ARA&A, 46, 339

Yang, B., Stancil, P. C., Balakrishnan, N., & Forrey, R. C. 2010, ApJ, 718, 1062

Yang, H., Herczeg, G. J., Linsky, J. L., Brown, A., Johns-Krull, C. M., Ingleby, L., Calvet, N., Bergin, E., & Valenti, J. A. 2012, ApJ, 744, 121

Yang, H., Linsky, J. L., & France, K. 2011, ApJ, 730, L10

Youdin, A. N. & Shu, F. H. 2002, ApJ, 580, 494

A.   Appendix: Inclination Measurements

In Figure A.1, I compare the sine of the literature inclination values listed in Table A.1 (with 90° being edge-on) to the logarithm of my Lyα based H I column densities. A number of the disks are transitional or pre-transitional, which may have mm-sized grains that are not azimuthally-symmetric in their distribution (Casassus et al. 2013; Fukagawa et al. 2013; van der Marel et al. 2013), making dust-based inclination estimates less reliable. Also, many targets have both gas and dust disks, which may provide different inclinations. However, for the transitional and pre-transitional disks in the sample with purely dust-based inclinations quoted in Table A.1 (DM Tau, GM Aur, and LkCa 15), I find gas-based inclinations in the literature that differ by only a few degrees from those determined by the dust (DM Tau: 33°, Guilloteau & Dutrey 1998; GM Aur: 56°, Simon et al. 2000; LkCa 15: 52°, Simon et al. 2000). I adopt the inclination values in Table A.1 for these targets, although there is little difference. The other transitional and pre-transitional disks with the most accurate inclinations have gas-based or both gas and dust-based inclinations. For the targets with the most accurate inclination values (see below), there is no tight correlation (based on the Spearman's rank correlation coefficient) with the H I column densities. Since I would expect a correlation to exist if H I absorption was coming from the disk (see Figure 3.9), this suggests that the majority of the measured H I column density is interstellar.

A.1.   Most accurate Inclination Measurements

The most accurate inclination measurements come from spatially and spectrally resolved CO emission lines in the sub-mm (Lyo et al. 2011; Rosenfeld et al. 2012a,b) and spatially resolved disks in sub-mm dust continua (Andrews & Williams 2007b; Isella et al. 2007; Andrews et al. 2011). 2D model fits to the data provide strong constraints on the orientation of the disk and are a direct method of determining the inclinations. Out of the 31 targets, 11 have the most accurate inclinations.
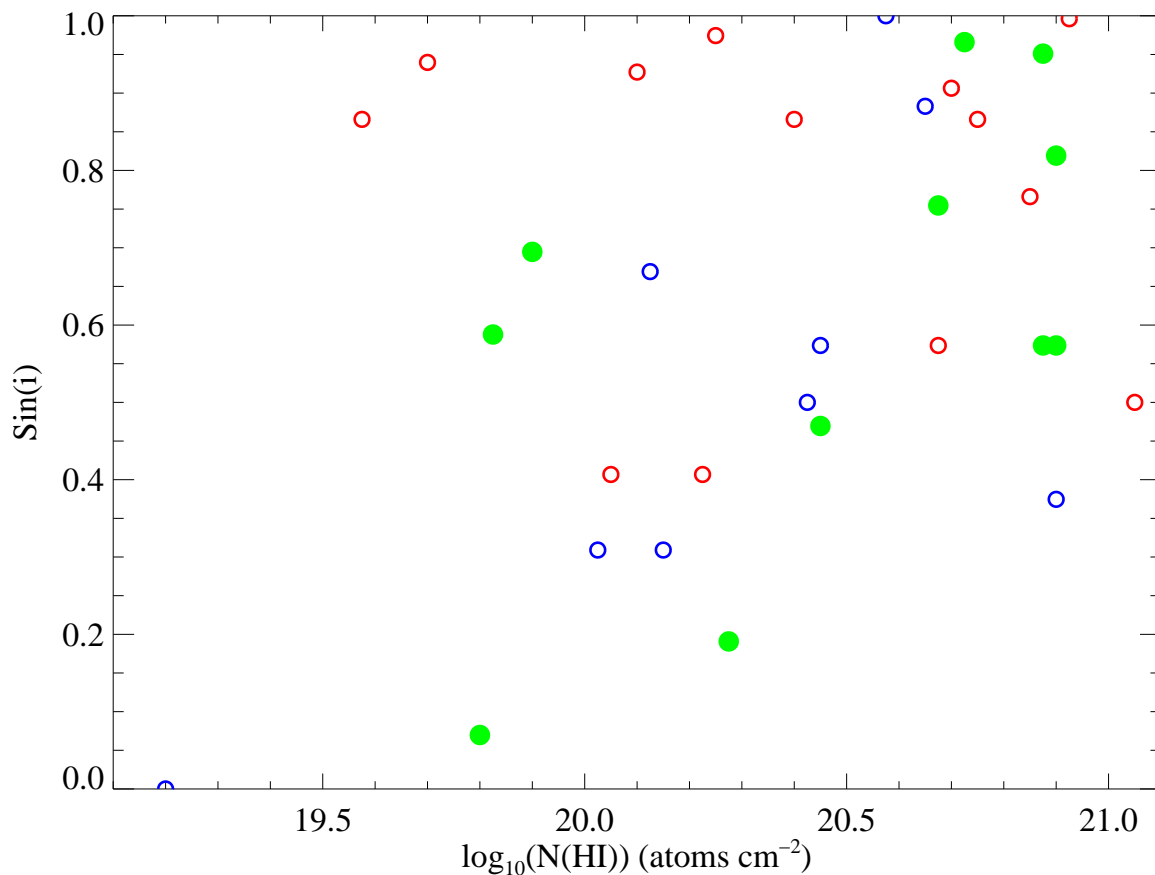
Fig. A.1.— The sine of the literature disk inclinations listed in Table A.1 (with 90° being edge-on) versus the logarithm of our measured H I column densities. Green filled circles are targets with the most accurate inclinations, red open circles are targets with less accurate inclinations, and blue open circles are the rest of the targets (other inclinations).

A.2.   Less accurate Inclination Measurements

Some of the less accurate inclinations found in the literature were derived from stellar rotation data. These measurements rely on accurate measurements of $v\sin i$, the stellar rotation period, and the stellar radius. The rotation period and the value of $v\sin i$ can be measured much more accurately than the stellar radius, which depends on the often uncertain parameters of stellar luminosity, reddening, veiling, and effective temperature (see Section 3.1). Appenzeller & Bertout (2013) find that inclination measurements determined from the stellar rotation are less reliable than those determined from spatially resolved disk observations.

Other less accurate inclinations come from SED modeling (AK Sco; Alencar et al. 2003), an assumption as no literature values were found (CS Cha; Espaillat et al. 2007, 2011), lower limits to intercept a flared disk model (HN Tau; McJunkin et al. 2013), Hα profile fits (RECX-11, RECX-15; Lawson et al. 2004), and fits to interferometric data (RW Aur; Eisner et al. 2007). Out of the 31 targets, 12 have less accurate inclinations.

A.3.   Other Inclination Measurements

The remaining inclination measurements do not spatially resolve the disk itself, but may be more accurate than the less accurate inclinations. These include targets such as AB Aur which has an inclination angle that varies with scale (Tang et al. 2012), CV Cha which has an inclination measured from χ^2 minimization models fit to brightness field maps (Hussain et al. 2009), and HD 104237 which has the inclination constrained using a microjet in the system (Grady et al. 2004). Other inclinations are those for BP Tau, HD 100546, SU Aur, SZ 102, and TWA 3A. Though SZ 102 and TWA 3A are typically quoted in the literature as edge-on and face-on, respectively, a well-defined measurement has not yet been made to our knowledge. Out of the 31 targets, 8 fall in this inclination category.

Table A.1.   Inclination Methods

Object	Inclination (degrees)	Inclination Ref.[a]	Inclination Method
AA Tau	75[b]	3	Elliptical Gaussian fits to the SMA sub-mm dust continuum visibilities
AB Aur	22[c]	24	Fit of IRAM 1.3mm continuum imaging
AK Sco	68[d]	2	Hipparcos parallax distance + orbit and stellar mass modeling (passive disk models to SED)
BP Tau	30[c]	22	Chisquare minimization of models to IRAM interferometer observations of ^{12}CO J=2-1
CS Cha	60[d]	8	Assumption as no literature value was found
CV Cha	35[c]	13	Chisquare minimization of reconstructed brightness field maps of stellar surface (spectropolarimetric observations)
DE Tau	35[d]	14	Spectroscopic IR stellar radii and rotation period + literature $v\sin i$ in the red
DF Tau A	85[d]	14	Spectroscopic IR stellar radii and rotation period + literature $v\sin i$ in the red
DK Tau A	50[d]	14	Spectroscopic IR stellar radii and rotation period + literature $v\sin i$ in the red
DM Tau	35[b]	4	2D Monte Carlo radiative transfer calculation leading to model of SMA continuum visibilities
DN Tau	28[b]	4	2D Monte Carlo radiative transfer calculation leading to model of SMA continuum visibilities
DR Tau	72[b]	3	Elliptical Gaussian fits to the SMA sub-mm dust continuum visibilities
GM Aur	55[b]	4	2D Monte Carlo radiative transfer calculation leading to model of SMA continuum visibilities
HD 100546	42[c]	5	Ellipticity of isophote fit to ACS coronographic images
HD 104237	18[c]	9	Velocity (both in plane of sky and radial) of the knot A in the microjet (STIS G140L)
HD 135344B	11[b]	16	SMA CO spectral line image models (^{12}CO and ^{13}CO J=2-1)
HD 163296	44[b]	21	SMA and VLA mm-observation models of continuum, ^{12}CO J=2-1 and J=3-2, and ^{13}CO J=1-0 emission
HN Tau A	> 60[d]	17	Not well constrained. Lower limit to intercept disk from flared disk model
IP Tau	30[d]	6	Stellar rotation velocity
LkCa 15	49[b]	4	2D Monte Carlo radiative transfer calculation leading to model of SMA continuum visibilities
RECX-11	70[d]	15	Magnetospheric accretion model fits to observed H-alpha profile
RECX-15	60[d]	15	Magnetospheric accretion model fits to observed H-alpha profile
RU Lup	24[d]	10,23	Rotational broadening of absorption lines, Rotational period + R_{star} + $v\sin i$
RW Aur A	77[d]	7	Interferometric data fit with inclined uniform disk model
SU Aur	62[c]	1	Visibility as a function of hour angle in the K-band fit with a Gaussian brightness profile inclined on the sky
SZ 102	~ 90[c]	12	Low luminosity possibly due to blocking of direct light by edge-on disk
TWA 3A	~ 0[c]	11	Assumption from large mid-IR excess and negligible optical reddening
TW Hya	4 - 10[b]	19	Disk models of ALMA ^{12}CO J=2-1 and J=3-2 data
UX Tau A	35[b]	4	Fit of bright, resolved CO J=3-2 disk in SMA data
V4046 Sgr	33.5[b]	20	Models of SMA ^{12}CO J=2-1 data
V836 Tau	65[d]	18	Assumed from colors and errors on rotation period, R_{star}, and $v\sin i$

[a] (1) Akeson et al. (2002); (2) Alencar et al. (2003); (3) Andrews & Williams (2007b); (4) Andrews et al. (2011); (5) Ardila et al. (2007); (6) Ardila et al. (2013) derived from Głębocki & Gnaciński (2005); (7) Eisner et al. (2007); (8) Espaillat et al. (2007, 2011); (9) Grady et al. (2004); (10) Herczeg et al. (2005); (11) Huenemoerder et al. (2007); (12) Hughes et al. (1994); (13) Hussain et al. (2009); (14) Johns-Krull & Valenti (2001); (15) Lawson et al. (2004); (16) Lyo et al. (2011); (17) McJunkin et al. (2013); (18) Najita et al. (2008); (19) Rosenfeld et al. (2012b); (20) Rosenfeld et al. (2012a); (21) Isella et al. (2007); (22) Simon et al. (2000); (23) Stempels et al. (2007); (24) Tang et al. (2012).

[b] Most accurate inclination

[c] Other inclination

[d] Less accurate inclination